DISS. ETH NO. 26421

SPECTROSCOPIC DISENTANGLEMENT OF THE QUANTUM STATES OF THE HIGHLY EXCITED COPPER DIMER

A thesis submitted to attain the degree of

DOCTOR OF SCIENCES of ETH ZURICH

presented by

Martin Michael Beck

Dipl.-Phys., Universität Konstanz

born on 25.06.1978

citizen of Germany

accepted on the recommendation of

Prof. Dr. Jeroen Anton van Bokhoven
Prof. Dr. Hans Jakob Wörner
Dr. Peter P. Radi

2019

Zusammenfassung

Obwohl Übergangsmetalle in der Biologie nur als Spurenelemente vorkommen, sind sie doch die Schlüsselelemente, die Leben wie wir es kennen durch ihre katalytischen Eigenschaften erst möglich machen. Auch in der chemischen Industrie wäre ohne Übergangsmetallkatalysatoren kaum ein Prozess realisierbar. Die quantenmechanischen Zusammenhänge, die hinter den besonderen chemischen, optischen und magnetischen Eigenschaften stecken, sind allerdings weitgehend unbekannt, da die Präsenz teilweise gefüllter d-Orbitale zu einer immensen Zustandsdichte führt. Durch die schiere Menge der möglichen, elektronischen Zustände, wird sowohl der experimentelle Zugang mittels Spektroskopie als auch der theoretische Zugang mittels ab-initio-Rechnungen massiv behindert. Das fehlende Verständnis der relevanten Quantenzustände macht es quasi unmöglich den chemischen Aufbau der Katalysatoren zu bestimmen, die notwendig wären um eine Grüne Chemie zu etablieren. Diese Arbeit adressiert diese grundlegende Problematik mittels nichtlinearer, doppelresonanter, optischer Laserspektroskopie. Als Studienobjekt dient dabei das Kupferdimer, das aufgrund der einfachen elektronische Konfiguration seines Grundzustands ein beliebtes Testsystem für theoretische Studien darstellt, gleichzeitig aber auch in der Natur als Kofaktoren in Enzymen relevant ist. Während in der Natur das chemische Umfeld das Kupferdimer aus seinem einfachen Grundzustand herausbewegt, ist es in dieser im Vakuum stattfindenden Studie die elektronische Anregung durch ultraviolettes Licht, die das Kupferdimer zu einem typischen Übergangsmetallsystem macht. In solchen sind, durch die Vielzahl der wechselwirkenden Quantenzustände, rotationsaufgelöste Spektren oft zu dicht und zu chaotisch um die beobachteten Linien individuellen Zuständen zuordnen zu können. Um dies dennoch zu tun, nutzen wir in dieser Arbeit zweifarbiges, resonanzverstärktes Vierwellenmischen als spektroskopische Methode. Dabei wird die

Wellenlänge eines Lasers genutzt, um einen Rotationszustand auszuwählen. Ein mit einem zweiten Laser aufgenommenes Spektrum vereinfacht sich dadurch massiv, da sich die Rotationsquantenzahl bei einem elektrischen Dipolübergang nur um maximal Eins ändern kann. Damit sind in solchen Spektren nur noch maximal drei Linien pro vibronischem Zustand möglich. Nimmt man eine Serie solcher Spektren auf, wobei man die ausgewählte Rotationsquantenzahl systematisch ändert, lassen sich die Spektren entsprechend der Rotationsquantenzahl als Fortrat-Diagramm übereinander anordnen. Darin setzen sich die zu einem spezifischen virbonischen Zustand gehörende Linien zu Parabeln gemeinsamen Ursprungs zusammen, wodurch eine eindeutige Zuordnung möglich wird. Im Falle des hochangeregten Kupferdimers wird neben den erwarteten Parabeln der bekannten Zustände eine Vielzahl kreuzender Systeme sichtbar (S. 92, Abb. 23). Viele sind dabei nur nahe der Kreuzung sichtbar, da nur dort durch einen quantenmechanischen Mischvorgang ein Anteil des Charakters des durchgehend sichtbaren Zustands übernommen wird. Da sich die resultierenden, anteilig identischen Zustände abstossen, kommt es zusätzlich zu einer Verschiebung der Linien. Die exakte Zuordnung der individuellen Linien erlaubt es eine Entstörung durchzuführen, wobei die molekularen Konstanten aller beteiligten vibronischen Zustände, sowie deren Wechselwirkung, quantitativ bestimmt werden. Dies erlaubt einen ersten Blick auf das dichte Netzwerk das durch Störungen zwischen den Zuständen aufgespannt wird. Am konkreten Beispiel des Kupferdimers ist insbesondere die starke Mischung zwischen einem kovalent gebundenen Zustand und einem ionisch gebundenen Zustand auffällig, die sich für eine Vielzahl von Vibrationszustände wiederholt. Da solche Mischvorgänge in der Born-Oppenheimer-Näherung ignoriert werden, liegt es nahe die Anwendbarkeit darauf aufbauender quantenchemischer Methode für die Beschreibung von Übergangsmetallsystemen zu hinterfragen, was allerdings den Rahmen dieser Arbeit sprengen würde. Stattdessen zeigt diese Arbeit

eine universelle Methode zur spektroskopischen Untersuchung kleiner Systeme hoher Zustandsdichte auf und liefert zusätzlich einen experimentellen Referenzdatensatz für den Test oder die Kalibrierung neuer quantenchemischer Berechnungsmethoden.

Da für die Anwendung der verwendeten, nichtlinearen Spektroskopiemethode ein Molekularstrahl mit hoher Dichte der zu untersuchenden Spezies benötigt wird, war die Inbetriebnahme und Verbesserung einer dafür konstruierten Clusterquelle zentraler Bestandteil dieser Arbeit (Kapitel 3). Kapitel 4 beschreibt die im Anschluss erfolgten Untersuchungen der niedrigliegenden elektronischen Zustände des Kupferdimers. Dabei wurde in einem eigentlich schon vollständig untersuchten Energiebereich ein weiterer Zustand gefunden, dessen optische Zugänglichkeit die Bedeutung der *jj*-Kopplung im Kupferdimer unterstreicht und gleichzeitig ein über 40 Jahre altes Rätsel bei der Charakterisierung des niedrigsten angeregten Singulett-Zustandes aufklärt. Dabei wurde in Kooperation auch aufgezeigt, wie dieser Energiebereich unter Berücksichtigung der Spin-Bahn-Kopplung und der ionisch gebundenen Zustände mit ab-initio-Methoden beschrieben werden kann. Kapitel 5 widmet sich schliesslich den rein experimentellen Untersuchungen der hochangeregten Zustände, die namensgebend für diese Arbeit sind und deren Kern darstellen.

Contents

1 Abstract

Transition metals are embedded as cofactors into a multitude of enzymes. Without their catalytic properties, essential biochemical reactions could not take place at ambient conditions. But besides their role for life itself, also the tremendous growth of the world population in the 20th century would not have been possible without their usage. Only by introducing artificial fertilizers, which were produced using transition metal catalysts, the agricultural production could supply the increasing demand in food. Next to the chemical properties, also the unique magnetic and optical properties of transition metals are used in a wide field of applications.

Despite their fundamental importance, the underlying quantum chemistry is barely understood. The reason for this is directly connected to the definition a transition metal itself: their open d electron shells provide a configurational manifoldness that gives rise to a high density of quantum states. Therefore, on excitation, transition metal containing systems are usually too complex to be completely covered by *ab initio* quantum chemical methods. Using high-resolution spectroscopy, the high density of states manifests itself in an impenetrable thicket of overlapping and chaotically disturbed bands. Thus, also the experimental analysis of the individual quantum states is inhibited. So, mankind has been resorting to engineering, supported by some approximating computational methods like density functional theory. But neither of these approaches brought insight into the actual transition metal chemistry that underlays virtually any chemical production. And while principles and practice of Green Chemistry have been well established, their implementation is out of reach.

This work addresses the spectroscopic hindrances introduced by the high density of states in transition metal systems. Inspired by the use of di-copper centers in nature, we decided to use the bare copper dimer as a test object.

Deep in the ultraviolet regime, we revisited bands that are characteristic for transition metal systems: dense and strongly perturbed, they are known to withstand attempts to assign their lines and not even their shapes could be reproduced by modeling molecular constants. To finally lift the veil that is spread out over such bands by the high density of states, we had to carry out spectroscopy on the individual rotational quantum state of the individual isotopologue. This was achieved by building a laser ablation cluster source (Chapter 3) that could provide the copper dimer in sufficient number density to apply two-color resonant four-wave mixing spectroscopy (TC-RFWM, see Chapter 2.3.1.1). With this double-resonant, non-linear method, instead of separate bands, a rich network of interacting quantum states became visible and also their individual interaction could be quantitatively described.

Conceptually, this opens many novel opportunities and sets the foundation for further experiments on systems with a high density of states, and enables performing a new generation of perturbation-facilitated experiments. Notably, the data provided by this (and prospective similar) work also enables calibration, respectively testing, of new and more efficient computational approaches based on (semi-)empirical models, *ab initio* quantum chemistry, machine learning, or quantum computing.

Already from the data presented in this work, it becomes obvious that even a light and simple transition metal dimer can easily violate the assumptions, which major computational methods depend on. Starting in the range of the lowest electronic excitations (Chapter 4), this work detected an additional optical accessible state, which implies that spin orbit-coupling is significant and calculations of pure spin states is not sufficient. Combining this finding with the already known relevance of ion-pair states, we could construct a reduced active space that provided a first accurate computational description of this range. For the highly excited states (Chapter 5), which are eponymous for this work and more representative for transition metal

systems in general, no well-established computational method is applicable, as their scaling prevents consideration of the required number of interacting quantum states. Experimentally, this range revealed the full nonadiabatic nature of transition metal systems: the rotational bands associated with each vibrational level of each electronic state form a dense grid. In proximity to each node of this grid, perturbations can occur depending on selection rules, Franck-Condon overlap and energetic separation. As a result, the experimentally observed states often result from vibronic coupling between two or more states. Therefore these states no longer have a single character, which would be described by good quantum numbers, but exists as superposition of multiple states of different characters (covalent and ion-pair character, different spin states, …). As the resulting mixed states partially share the same character, their levels repel each other and this finally causes the odd shapes reported for such spectral bands.

On the other hand, the mixing provides optically accessible gateways between otherwise separated manifolds and potential energy surfaces. In this work, such gateways were used to access the near dissociation regime of the electronic ground state of the copper dimer (Chapter 5.3.3). For this purpose, we utilized a state that is constituted by perturbation-facilitated mixing of a high-lying bright state, which exhibits similar properties as the ground state, and a highly vibrational excited dark state, which itself is the result of an avoided crossing of a covalent and an ionic state. Inherited from the dark state, the mixed state exhibits ion-pair character, and thereby high transition strength, towards the outer turning point of the vibrational motion. As this corresponds to large internuclear separation, far beyond the lower part of the ground state potential, most spontaneous emission yields highly excited vibrational levels of the electronic ground state.

Also outside of the field of spectroscopy, it is obvious that the mixing of states cannot be ignored. Regarding computational chemistry, this explains

why the established methods fail to comprehend or predict catalytic properties, as the methods to describe complex systems always start with the Born-Oppenheimer approximation to then eventually add further constraints like fixed spin states. While such approaches work reasonably well in organic chemistry and to predict most ground state structures, they neglect all the couplings demonstrated in this work. Methods like those used in Chapter 4.3, which consider such couplings, break down on realistically-sized, excited systems due to scaling issues. Therefore, to reproduce the dynamics of excited transition metal systems, new computational methods are needed. And to test or calibrate these, one will have to rely on further experiments in the fields of spectroscopy and cluster science. But even so this work has the ambition to inspire such efforts, these challenges lie beyond its scope.

2 Introduction

2.1 The current state of research

The experimental knowledge on the electronic states of the copper dimer was primarily established around the 1980s, when laser vaporization sources were introduced, but also other metal cluster sources advanced. As these sources provided cold molecular beams of unligated metal dimers and clusters*, the methods of molecular spectroscopy became applicable. Before this, research was done mostly by using spectrographs to record absorption or emission spectra in furnaces or flames. The most comprehensive overview of the experimentally known states of the copper dimer, as well as a profound discussion of its properties, was provided as a book chapter by Morse in 1993.[1] As a review, it composed all experimental work on dimers of the transition metals in the elemental groups of nickel and copper. It gives a good overview of the general trends within the transition metals, and on the d orbital participation in the chemical bond. For the copper group, there is special emphasis on the influence on the ion pair ground state, which becomes relevant due to the low ionization potentials of metals and the resulting, low-lying ionic separate atom limits. However, the challenging experimental requirements to prepare a molecular beam of such unstable species, which in almost any environment would instantly react, kept the number of experiments on these species constrained. This is aggravated by the fact that laser vaporization sources cannot produce monodisperse species, so that the corresponding species for each optical feature needs to be identified by photo-ionization and mass spectrometry, or by identification of specific isotopic patterns. The most successful method to do so was

* The term cluster is typically used to describe particles consisting out of 3 to N atoms. Classification with regard to N: small: $\leq 10^2$; medium: 10^2–10^4; large: $\geq 10^4$.

resonant two-photon ionization in combination with mass selective detection, which was provided by time-of-flight mass spectrometry. Upon initial assignment of spectral bands to specific species, also other spectroscopic methods were applied to refine the knowledge on these bands (*vide infra*). With this, rotational resolution could be achieved for a few strong bands, but otherwise many properties stayed vague. For the copper dimer, a large number of electronic states were revealed, but still properties like the Hund's coupling case could not be decided.

In the following decades, only a limited amount of knowledge on the copper dimer was added. Therefore the work of Morse is still the best reference to describe the copper dimer as it was known before starting this work. Figure 1 shows the original table of electronic states composed by Morse. Historically, the names of the state were chosen using the Hund's case (a) naming scheme, which uses capital letters for singlet states and lowercase letters for triplet states. But already by looking at the term symbols used by Morse, the uncertainty on this assignment becomes obvious, as only the ground state X and the a state were denoted using the Hund's case (a) labels $^1\Sigma_g^+$ and $^3\Sigma_u^+$. As expected from selection rules for electric dipole radiation, the a-X transition was not observed in gas phase experiments. However, for copper dimers embedded in a cryogenic rare gas matrix, it could be detected and a radiative lifetime of 27 ms was reported for the a state.[2] Both the X and the a state asymptotically approach the limit of two ground state atoms (^{2}S+^{2}S), where the $3d^{10}\ 4s^1$ electron configuration allows the formation of a single σ bond. Going up in excitation energy, the atomic ^{2}S state is followed by the ^{2}D state with a $3d^9\ 4s^2$ electron configuration. For the copper dimer, this provides a ^{2}S+^{2}D separate atom limit for the next set of molecular states. Based on Hund's coupling case (a) and selection rules, one would expect to observe only two transitions from the ground state to states related to this limit: one into a $^1\Sigma_u^+$ state and one into a $^1\Pi_u$ state.[3] These would be spectroscopically distinguishable, as only transitions into the $^1\Pi_u$ state would exhibit a Q

branch[†]. Indeed, two bands were reported in the associated energy range and labeled A and B.[4,5] When the B state was assigned $^1\Sigma_u^+$,[6] it was obvious to assign A $^1\Pi_u$, when reporting a rotational analysis of the A-X system.[7] However, a Q branch was not seen in a subsequent study.[8] When the absence of a Q branch was confirmed in a further study, but knowing that there should exist only one $^1\Sigma_u^+$ state in this region, Hund's case (c) coupling was suggested as a possible alternative.[9] Assuming significant spin-orbit coupling and Hund's case (c), each of the two $^2S+^2D$ asymptotes ($^2S_{1/2}+^2D_{5/2}$ and $^2S_{1/2}+^2D_{3/2}$) gives rise to a 0_u^+ state. Assigning both the A state and the B state 0_u^+, the spectroscopic absence of a Q branch makes sense. Still, the unusual relations of the vibrational constants, bond lengths, and short life times wouldn't be explained by these assignments. Morse suggested to take the low-lying ion-pair ground state into account. As this state would be also of $^1\Sigma_u^+$ resp. 0_u^+ symmetry, and by its ionic nature also introduce high transition strengths, which would explain the low life times, it would present an alternative explanation for the experimental findings. Then again, this explanation would no longer depend on Hund's case (c) coupling.

State	$T_0(cm^{-1})$	$\omega_e(cm^{-1})$	$\omega_e x_e(cm^{-1})$	$B_e(cm^{-1})$	$\alpha_e(cm^{-1})$	$r_e(Å)$	*Lifetime (μs)*
J	37448.8[j]	288.4[k]	0.64[k]	0.1165[i]	0.0010[i]	2.145(5)[i]	
I	~35000[k]	280[k]	1[k]				
H	36559[k]	713[k](?)					
G	30678[b]	116.0[k]	0.046[k]			2.73[b,l]	
F	~28550[k]	248.0[k]	0.90[k]				
D	25508[j]	~160[j]				2.38(3)[j,l]	6.5[j]
C 1_u	21843.9[j]	221.4[l]	1.764[l]	0.1045[i]	0.00092[i]	2.2643(11)[i]	0.80(10)[f]
B 0_u^+	21747.88[h]	245.2[h]	2.0[h]	0.09889[g]	0.00061[g]	2.3276(1)[g]	0.040(5)[f]
A 0_u^+	20396.0[e,h]	192.47[e,h]	0.353[e,h]	0.10276[e,h]	0.00092[e,h]	2.2834[e,h]	0.115(10)[f]
a $^3\Sigma_u^+$	~15350[d]	125(25)[d]				2.48(3)[d,l]	27000[d]
X $^1\Sigma_g^+$	0.00	266.43[b]	1.035[b]	0.10874[c]	0.00061[c]	2.2197(1)[c]	—

Figure 1: Overview of all experimentally known electronic states of $^{63}Cu_2$ as reported by M. D. Morse in *Advances in Metal and Semiconductor Clusters* Vol. 1 (ed M. A. Duncan) p. 92 (JAI Press, 1993).

[†] In spectroscopy, Q lines and branches denote transitions where the rotational quantum number does not change. Their appearance depends on selection rules.

Still in the same region, the C state was initially discovered as an extra feature when using laser induced fluorescence (LIF) to study the vibrational progression in the hot-bands of the B-X transition.[10] Later, by producing colder dimers, this band could be isolated and assigned to Π symmetry.[11] Reinterpreted in Hund's case (c), Morse listed it as C 1_u. Beyond this state, the findings became vague and no further state has been fully characterized. The D state was only detected in a rare gas matrix.[12] The E state, but also other states assigned earlier with limited certainty, were no longer mentioned by Morse in the table reproduced in Figure 1, but are referenced in an older review of the same author.[13] The knowledge of the F-J states mostly originates in a single study using resonance two-photon ionization (R2PI) with mass selective detection.[14] The unambiguous correlation between spectral features and isotopologues enabled the assignment of electronic states even where only small progressions of vibrational levels were observed. However, the fragmentary nature of this data and strong perturbations allowed only approximate determination of molecular constants, often based on extrapolation. Still, the G state could be utilized in a later study on the electronic ground state,[15] as its shallow potential allowed to observe dispersed fluorescence into the lower 64% of the vibrational levels of the ground state X. The J state is a special case. In the R2PI experiments, the vibrational levels were distorted by additional features that could not be assigned.[11] In a later R2PI experiment, which was studying the autoionization of Cu_2 and the vibronic states of Cu_2^+, it was concluded that the J state is formed by excitement of a 3dπ electron into a 4p orbital.[16] Still, the available information was insufficient to decide the parity of the 3d hole. Due to the high strength of the J-X transition, it was also accessible in the LIF study in which the C state was characterized.[11] However, the symmetry of the J state could not be determined, as the shape of the rotational bands were not reproduced by simulation of any symmetry. Only coarse molecular constants could be estimated based on the spacing between high rotational levels.

In the same book chapter, Morse used the molecular constants that were reproduced in Figure 1 to draw estimated potential energy curves of the experimentally known states. The resulting figure is reproduced as Figure 2. Based on the assumption of Hund's case (c) coupling, it provides a consistent picture of the observed electronic states. However, the ion-pair states are neglected and just an estimated electrostatic potential indicates the asymptotic shape of the outer potential wall of the ion-pair ground state. Diatomic systems, which have the internuclear distance as only continuous parameter, exhibit strict non-crossing rules. Therefore, the potential curve of the ion-pair ground state, which is of $^1\Sigma_u^+$ resp. 0_u^+ symmetry, cannot cross any other $^1\Sigma_u^+$ resp. 0_u^+ state. Consequently, most potential curves cannot have the regular shape drawn in Figure 2. Still, for the experimentally observed parts, their shapes are in good agreement. Thus, Figure 2 was the best available starting point for most discussions deep into the project described by this thesis, and, therefore, is included as reference for further discussion.

After the book chapter of Morse was written, only little additional knowledge was gained. In 1992, Fourier transform emission spectroscopy on the B-X transition was used to improve the accuracy of their molecular constants based on measuring their lowest vibrational levels.[17] In 1999, additional systems were identified within absorption spectra collected in the deep-UV range, by using white light of a xenon lamp.[18] Even so this just revealed band head positions over broad background features, the obtained vibrational constants of the lower state reproduced those of the copper dimer ground state. Further refinement on the constants of the D state were provided in 2000 by studies in liquid and solid Helium.[19] In 2014, the photodissociation dynamics of the copper dimer were studied by R2PI combined with velocity map imaging based detection.[20] In addition, this study used two-color spectroscopy to also scan over the low-lying electronic states (A-C) at vibrational resolution.

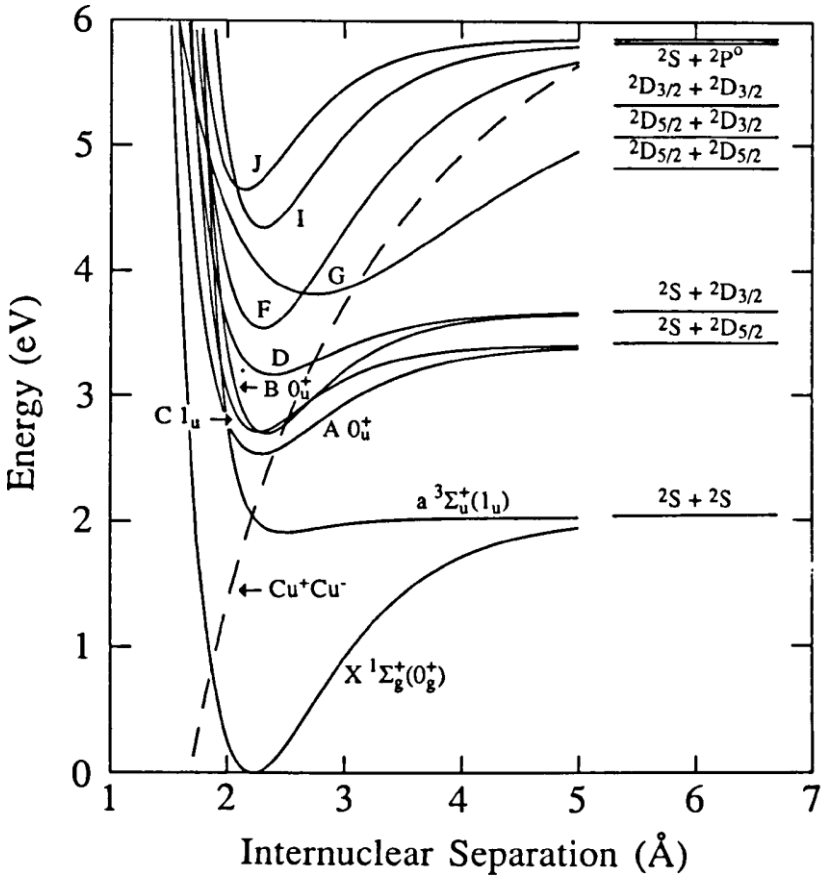

Figure 1. Qualitative potential energy curves for the experimentally known electronic states of Cu_2. Bond lengths, vibrational frequencies, and electronic energies are taken from Table 5. Electronic potential energy curves are plotted as Morse potentials, with anharmonicities adjusted to force dissociation to appropriate atomic limits. For the X, a, A, and B states these limits are certain. For the D and J states the chosen atomic limits are likely, but not certain. For the poorly characterized F, G, and I states the limits are speculative at best. The H state is so poorly characterized that it is omitted from this figure. Finally, the ionic Cu^+Cu^- curve is plotted as a dashed line according to equation 3. See the text for discussion.

Figure 2: Depiction of all experimentally known electronic states of $^{63}Cu_2$ as reported by M. D. Morse in *Advances in Metal and Semiconductor Clusters* Vol. 1 (ed M. A. Duncan) p. 95 (JAI Press, 1993).

2.2 Electronic states of the copper dimer

Declaration: This chapter gives an overview over structure of the molecular states in the copper dimer. As this discussion relies only on basic knowledge, which can be looked up in any chemistry textbook, no references are given. An extensive discussion of these aspects can be found in chapter V and VI in Herzberg's Spectra of Diatomic Molecules[3].

The electronic state of a molecule is associated with a certain configuration of its electrons in the orbitals around and between the nuclei. Therefore, this chapter shall start by a short introduction on the concept of orbitals.

2.2.1 Atomic orbitals

As a fermion, the electron must obey the Pauli exclusion principle. This requires that each possible quantum state, which an electron can hold in the quantum system established by the atom, must not be occupied by more than one identical electron. In chemistry, these quantum states are mostly described as localized orbitals. Given that the electron has an intrinsic quantum property of a spin, which can be either up or down, the Pauli exclusion principle allows to place up to two electrons in each orbital. While the discussion following below will be based on such localized orbitals, unitary transformations give rise to an infinite number of sets of delocalized orbitals, which provide an equivalent description of the occurring quantum mechanics. Therefore, one should not expect a specific electron to be strictly confined in the spatial extent of a specific localized orbital.

In presence of more than one electron, the orbitals are defined by three quantum numbers: the principal quantum number n, which indicates the electron shell the orbital belongs to, the azimuthal quantum number l, which describes the orbital angular momentum of the electron, and the magnetic quantum number m_l, which defines the spatial orientation of the orbital. Adding the electron spin s, one obtains a set of four quantum numbers, which fully describe an electron within an atom. The ranges of these quantum numbers are n = 1, 2, …; l = 0 – n-1; m_l = -l – +l; s = -½, +½. The azimuthal

quantum number l defines the shape of the orbital. The values l = 0, 1, 2, 3, 4 correspond to s, p, d, f, g orbitals. For p orbitals, m_l just defines the spatial orientation, for larger values of l, it also influences the shape. Sequential filling of these orbitals (following the *aufbau* principle) reproduces the structure of the periodic table of elements.

2.2.2 Molecular orbitals in diatomic species

Molecular orbitals can be constructed based on spatial overlap of atomic orbitals. If the orbitals overlap in phase, the constructive interference adds electron density between the positive nuclei: a bonding molecular orbital is formed. If the orbitals overlap out of phase, destructive interference introduces a node between the nuclei and a non-bonding molecular orbital is formed. Therefore, in general, for each set of interacting atomic orbitals, two molecular arise: one bonding orbital, which lies lower in energy than the atomic orbitals, and one non-bonding molecular orbital, which energetically lies above them. Non-overlapping atomic orbitals do not significantly contribute to the bonding and stay mostly unchanged.

The molecular orbitals are classified by their symmetry. If the bond is formed symmetrically about the internuclear axis, the label σ is used. If two lobes are formed symmetrically to the internuclear axis, the label π is used. For the main group elements, this is almost sufficient to describe bonds. All s orbitals, and p orbitals that are pointing towards each other, form σ bonds. The p orbitals perpendicular to the intermolecular axis form π bonds. When d orbitals come into play, what obviously is the case for transition metals, also bonds with four lobes around the internuclear axis can be formed, which is labeled δ. In theory, this could be continued for orbitals of arbitrary l values, where Greek letters would be used to label the bonds in alignment with the Latin letters used to describe the orbitals. But already for the φ bond, which forms six lobes around the internuclear axis, only a single example was reported as part of the quintuple bond of the uranium dimer[21]. However,

recent relativistic quantum chemical calculations suggest, that the uranium dimer exhibits just a quadruple bond, with no φ bond formed.[22]

Not all molecules follow the alignment of localized atomic orbitals. A way to preserve the comprehensible depiction of localized orbitals is provided by hybridization. There, hybrid atomic orbitals pointing towards the neighboring atoms are constructed by mixing several atomic orbitals. A well-known example of carbon where sp^3 hybrids provide the symmetrical 3D structure of diamonds and methane molecules, while sp^2 hybrids govern the shape 2D graphite layers. But also non-integer ratios can be used, e.g. to form smaller bond angles of molecules like water by increasing the p ratio to the hybrid atomic orbital. In such a case, the remaining ratio of s and p characters are distributed over hybrid atomic orbitals occupied by lone electron pairs. Inclusion of d orbitals into hybridization, arbitrary structures can be explained. But, while this allows to draw simple bonding schemes, it does not establish an accurate picture of energy levels. As already mentioned, this is also misleading in suggesting actual localization of specific valence electrons, which, outside of this specifically constructed description, are delocalized over the complete molecule.

For homonuclear dimers, the similar charge of the nuclei introduces a center of inversion, which gives rise to a further symmetry label: g (*gerade*/even) or u (*ungerade*/odd). The orbitals are localized symmetrically in respect to this inversion center, but the sign of the wave function may swap. If the sign is preserved when passing through this center, the corresponding state is *gerade*, if the sign flips it is *ungerade*.

For heteronuclear dimers, not only the center of inversion disappears, but also the energies of the atomic orbitals differ. This mismatch reduces the spreading between the bonding and non-bonding molecular orbitals formed, and thereby reduces the bond strength. However, as the effective nuclear charge of the two nuclei (as seen by the electrons) is no longer identical, the

charge is partially shifted towards one of the atoms. This gives the bond a partial ionic character which adds to the bond strength. That ionic states can also play a significant role for homonuclear dimers, will be emphasized in the scientific chapters of this work, and is omitted here.

2.2.3 Relating molecular orbitals to spectroscopy

Even so electrons and orbitals provide a reasonable description of intra- and intermolecular interactions, they are typically not the observables studied in optical spectroscopy. Instead, one observes the state of the overall quantum system, which is established by the wholeness of the states of all electrons and nuclei. Therefore, based on the states discussed in Chapter 2.1, it is not possible to readily draw an accurate molecular orbital diagram for the copper dimer, as the electronic configurations of the contributing states are in general not known. Without this knowledge, the energetic order of the orbitals cannot be inferred. In the second period of the periodic table, where accurate molecular orbital (MO) diagrams for the molecules are known, a systematic change in the energies of the orbitals exists. For the dimers of transition metals, the situation is more difficult and no comprehensive overview is available.

One way to create a MO diagram of a molecule like the copper dimer, could be found in the analysis of high-level ab initio data, generated as described in Chapter 2.3.2.1. If a unitary transformation would be found that transforms the result into a representation consisting out of fully localized electrons, a MO diagram could be derived therefrom. However, the *ab initio* results in Chapter 4.3 suggest that many states exist as a mixture of different electron configurations. As a result, the question whether a meaningful MO-diagram could be drawn for this system cannot be answered within the scope of this introduction.

Experimentally, the individual electron configurations sometimes can be probed by methods like R2PI. For the J state, the work by Sappey et al.[16],

which was already mentioned in Chapter 2.1, could narrow down the electronic configuration for the J state to just two possibilities. But, even though this reasoning, which based on atomic and molecular orbitals, finally allowed to state the full electron configuration of the J state (Chapter 5.2), this single result cannot establish further discussion in terms of MO diagrams. Therefore, further discussion will be based on electronic states only.

2.2.4 Classification of molecular electronic states

When discussing molecular electronic state, next to a name, which is typically assigned on first observation, the properties of an electronic state are described by a term symbol (short: term). It contains information on quantum numbers and symmetry as discussed hereafter.

The main classification of molecular electronic states is based on the total orbital angular momentum L. Its component along the internuclear axis Λ is used to label the states analogous to the S, P, D, F… labeling of atomic states.[‡] Therefore, Λ = 0, 1, 2, 3… is stated as Σ, Π, Δ, Φ… respectively.

The total spin quantum number S is obtained by summing up the spins of all individual electrons (being either +1/2 or -1/2). Therefore it is integer for molecules containing an even number of electrons, and half-integer if there is an odd number of electrons. As the spin of paired electrons cancels out, 2S is a measure for the number of unpaired electrons. The spin component Σ can take on 2S+1 different values ranging in integer steps from -S to +S. However, Σ is only defined in presence of an internal magnetic field ($\Lambda \neq 0$).

The total angular momentum of the electrons along the internuclear axis Ω is obtained by addition of orbital angular momentum and spin components: $\Omega = | \Lambda + \Sigma |$. If Λ is not equal to 0, the electronic term splits into a multiplet

[‡] Λ is the absolute value of the actual component M_L, which is ranging from -L to +L.

of 2*S*+1 different components. For Σ states ($\Lambda = 0$), this splitting is only present for rotating molecules. The value 2*S*+1 indicates the multiplicity of a state.

Further classification is provided based on symmetry properties. For homonuclear dimers, the distinction in gerade and ungerade states is used as already introduced for molecular orbitals (Chapter 2.2.2), using the symbols g and u. For Σ states, reflections on planes through the internuclear axis provide an additional distinctive feature. If the electronic eigenfunction is unchanged on reflection through such a plane, the state is labeled Σ^+, otherwise Σ^- is used. For degenerate states ($\Lambda \neq 0$), this distinction is not relevant, as reflection does no longer leave the eigenfunction unchanged. For these states, even when the cases are still distinguishable mathematically, their energies are exactly equal (without taking some splitting in rotating molecules into account).

Based on the quantum numbers and symmetries just discussed, a term symbol (short: term) can be constructed as a compact representation of the main properties of an electronic state. It has the form ${}^{2S+1}\Lambda_{\Omega,(\mathrm{g/u})}^{(+/-)}$.

2.2.5 Hund's coupling cases

For spectroscopic studies, the coupling between the electronic motion and the rotation of the molecule cannot be ignored. Except for a ${}^1\Sigma$ state, where both the total spin *S* and the total orbital angular momentum *L* of the electrons are zero, one needs to consider how the total angular momentum *J* of an atom is constructed based from these components. An idealized distinction in five cases was provided by Hund. They are based on comparing the strength of three couplings: the electrostatic coupling of *L* to the internuclear axis; the spin-orbit coupling; and the rotational coupling of *L* and *S* to the total angular momentum *J*.

Hund's case (a) assumes a strong electrostatic coupling of the electronic motion to the internuclear axis. S is then coupled to L by spin-orbit coupling, but there is virtually no coupling to the rotation of the molecule.

Hund's case (b) assumes again a strong electrostatic coupling, but this time spin-orbit coupling is negligible and rotational coupling comes first. This causes that for rotational levels no longer J is enumerated, but N which is excluding the spin component S (J=N+S). In old literature (e.g. Herzberg) the label K is used instead of N.

Hund's case (c) assumes a dominant spin-orbit coupling, followed by an intermediate electrostatic coupling and a negligible rotational coupling. With this, the component of the orbital angular momentum along the internuclear axis Λ is no longer defined and the component of the total angular momentum along the internuclear axis Ω has to be used as substitute when specifying a term symbol ($\Omega_{(\mathrm{g/u})}^{(+/-)}$). Also, Ω can be no longer obtained from Λ and Σ. Instead, it is defined as $\Omega = |M_{J1} + M_{J2}|$, where M_{J1} resp. M_{J2} are the components of the atomic total angular momentum J of atom 1 resp. atom 2 along the internuclear axis.

Hund's case (d) is dominated by the rotational coupling, followed by the electrostatic coupling. In this case, the spin-orbit coupling is negligible.

Hund's case (e) describes the rare situation where the electrostatic coupling is weaker than both spin-orbit and rotational coupling. This case does no further distinguish the relative strengths of spin-orbit and rotational coupling.

2.2.6 Derivation of the electronic states of the copper dimer

The general procedure to derive the molecular term manifolds from the states of the separated atoms of a dimer was already presented by Herzberg (Ref. [3], pp. 315-322). For a neutral dimer that is put together from a copper atom in a ^{2}S state (e.g. the ground state) and a copper atom in a ^{2}D state, Page and Gudeman already carried this out.[11] Applying this procedure on the low-

lying separate atom limits of the copper atom, Table 1 lists the corresponding bound states, both for assuming Hund's coupling cases (a) and (c). As already the states from the lowest $^2S+^2D$ limits are affected by the $^1\Sigma^+/0^+$ ion-pair ground state, the ion-pair ground state was added to the table to obtain a complete picture of the low-lying states. For the highly excited states, also excited ion pairs become relevant. However, there is no experimental data basis to recount the number of missing/undiscovered states in this energy range. Thus, these limits were omitted when compiling Table 1.

While the procedures to derive the molecular states from the separate atom asymptotes are well established, literature is inconsistent when it comes to counting of the expected molecular states arising on combination of unlike separate atoms limits. The reason for this can be found in the degeneracy of states with $\Lambda \neq 0$ (Hund (a)) resp. $\Omega \neq 0$ (Hund (c)). For these states, changing

Table 1: Molecular states of Cu_2 with their respective separate atom limits. The order follows the energetic order of the limits. In Hund's case (a), the values of *J* are disregarded. The ion pair ground state was added, as it also contributes to avoided crossings discussed in later chapters. The number in parentheses following the term symbol indicates the number of distinguishable states. Degenerated states are counted only once.

Separated atom limit	Hund's case (c) states	Hund's case (a) states
$^1S_0+^1S_0$ (Cu^+Cu^-)	0_g^+, 0_u^+	$^1\Sigma_g^+$, $^1\Sigma_u^+$
$^2D_{3/2}+^2D_{3/2}$	$0_g^+(2)$, 1_g, 2_g, $0_u^-(2)$, $1_u(2)$, 2_u, 3_u	$^1\Sigma_g^+(3)$, $^1\Pi_g(2)$, $^1\Delta_g(2)$, $^1\Phi_g$, $^1\Gamma_g$, $^3\Sigma_g^-(2)$, $^3\Pi_g(2)$, $^3\Delta_g$, $^3\Phi_g$, $^1\Sigma_u^-(2)$, $^1\Pi_u(2)$, $^1\Delta_u$, $^1\Phi_u$, $^3\Sigma_u^+(3)$, $^3\Pi_u(2)$, $^3\Delta_u(2)$, $^3\Phi_u$, $^3\Gamma_u$
$^2D_{3/2}+^2D_{5/2}$	$0_g^+(2)$, $0_g^-(2)$, $1_g(4)$, $2_g(3)$, $3_g(2)$, 4_g, $0_u^+(2)$, $0_u^-(2)$, $1_u(4)$, $2_u(3)$, $3_u(2)$, 4_u	
$^2D_{5/2}+^2D_{5/2}$	$0_g^+(3)$, $1_g(2)$, $2_g(2)$, 3_g, 4_g, $0_u^-(3)$, $1_u(3)$, $2_u(2)$, $3_u(2)$, 4_u, 5_u	
$^2S_{1/2}+^2D_{3/2}$	0_g^+, 0_g^-, $1_g(2)$, 2_g, 0_u^+, 0_u^-, $1_u(2)$, 2_u	$^1\Sigma_g^+$, $^1\Pi_g$, $^1\Delta_g$, $^3\Sigma_g^+$, $^3\Pi_g$, $^3\Delta_g$, $^1\Sigma_u^+$, $^1\Pi_u$, $^1\Delta_u$, $^3\Sigma_u^+$, $^3\Pi_u$, $^3\Delta_u$
$^2S_{1/2}+^2D_{5/2}$	0_g^+, 0_g^-, $1_g(2)$, $2_g(2)$, 3_g, 0_u^+, 0_u^-, $1_u(2)$, $2_u(2)$, 3_u	
$^2S_{1/2}+^2S_{1/2}$	0_g^+, 0_u^-, 1_u	$^1\Sigma_g^+$, $^3\Sigma_u^+$

the signs of both summands to the angular momentum $\Lambda = |M_{L1} + M_{L2}|$ resp. $\Omega = |M_{J1} + M_{J2}|$ does not affect the energy of the resulting state. Therefore, these states exists as degenerate pairs. Authors that just count all permutations thus obtain significantly higher numbers of states. For example, when following Herzberg, the $^2S+^2D$ limit gives rise to a 12 states (*vide infra*), while $(2s_1+1)(2l_1+1)(2s_2+1)(2l_2+1)$ gives 20 permutations and, including g/u, 40 states. As Table 1 is meant to support experiments, it just lists the observable states without including the degeneracy of Λ resp. $\Omega \neq 0$ and triplet states. This results in a table similar to the one presented by Bishea and Morse for the gold dimer[23], as Cu and Au exhibit an equivalent configuration of the valence orbitals. A comprehensive comparison of the anyway quite different coinage metal dimers was presented by Morse.[1]

When combining two ground state copper atoms ($^2S+^2S$), Hund's case (a) gives rise to a $^1\Sigma_g^+$ and a $^3\Sigma_u^+$ state. In Hund's case (c), *L* and *S* are no longer coupled to the internuclear axis. Therefore, reflection symmetry can be broken even when joining two atoms of identical states ($^2S_{1/2}+^2S_{1/2}$). This gives rise to a 0_u^- state in addition to the 0_g^+ and 1_u states deduced analogous to Hund's case (a). Combining a ground state atom with an atom in the lowest excited ^2D state ($3d^94s^2$), Hund case (a) gives rise to Σ^+, Π, and Δ states ($\Lambda=|M_S+M_D|$, $M_S=0$, $M_D=\{-2,-1,0,1,2\}$). As always when joining atoms of identical nuclear charge but different atomic state, each molecular state exists both as a *gerade* and an *ungerade* version. Being the product of joining two doublet states, each of these states further exists as a singlet and a triplet version. For Hund's case (c), the same limit splits into $^2S_{1/2}+^2D_{5/2}$ and $^2S_{1/2}+^2D_{3/2}$. The states are obtained by permutation of the *J* values of the individual atoms, taking again into account the degeneracies. As the Hund's case (a) limit $^2D+^2D$ combines identical atoms in an identical state, the number of *gerade* and *ungerade* states is different again. In Hund's case (c), this does not apply to the $^2D_{5/2}+^2D_{3/2}$ limit, which exhibits the uniform distribution of *gerade* and an

ungerade states known for states resulting from unlike states of the separated atoms.

Even so the different Hund's cases were discussed as alternatives, their separation is an idealization and reality often lies in between. Also, when approaching the separate atom limit of a molecular state belonging to Hund's cases (a) or (b), at larger internuclear distances spin-orbit coupling becomes dominant, and *J-J* coupling as in Hund's case (c) occurs. Therefore, when looking at selection rules for transitions and perturbations between molecular states, a premature restriction to only one Hund's case should be avoided.

2.3 Methodology

2.3.1 Experimental

As most methods utilized in this work are well established, this chapter focuses on their application to study the systems discussed in this work, which often extends their traditional field of application. Therefore the following chapters relate the spectroscopic methods directly to the analysis of the obtained spectra. For a full description of the multifarious effects manifesting in spectra of perturbed, diatomic molecules, which are studied in this work, comprehensive discussion is provided in a book written by Herzberg[3], and a book written by Lefebvre-Brion and Field[24]. While Herzberg's book established the still valid fundamentals related to spectra of diatomic molecules already in 1950, years before even the first laser was built, the work of Lefebvre-Brion and Field combines the findings in the spectra and dynamics of such systems obtained in the second half of the 20th century.

2.3.1.1 *Two-color resonant four-wave mixing spectroscopy*

Declaration: this chapter illustrates the method using the example of [P. Bornhauser, R. Marquardt, C. Gourlaouen, G. Knopp, M. Beck, T. Gerber, J.A. van Bokhoven, P. Radi, "Perturbation-facilitated detection of the first quintet-quintet band in C_2", *J. Chem. Phys.*, 2015, **142**, 094313], where the author contributed to a part of the experimental measurements.

Two-color resonant four-wave mixing (TC-RFWM) spectroscopy was established in the 1990s, even though it was still called two-color laser induced grating spectroscopy.[25-28] The name TC-RFWM was established by Rohlfing et al. when they proposed its use as a general tool for double-resonant spectroscopy in 1995.[29] TC-RFWM utilizes a combination of resonant four-wave mixing with a double-resonant optical spectroscopy. In general, four-wave mixing occurs when three wavelengths interact in a nonlinear medium, which enables a fourth wavelength to be generated by interference. However, this process is only efficient if the phase of the incoming waves is matched. More precisely, the k-vectors of the three incoming and the produced wave must add up to zero. This nonlinear process is further enhanced when the incoming waves are in resonance with a transition in the mixing medium. Reports of resonance-enhanced four-wave mixing processes range back until 1967, when parametric conversion of IR light was observed in potassium vapor.[30] In the second half of the 1970s, four-wave mixing was increasingly discussed as method for nonlinear spectroscopy(Ref.[31] and refs. therein). However, it's wide application started in the early 1990s, when its property of producing a spatially coherent, polarized signal beam was utilized to obtain spectra of radical species within flames and reaction plasmas(Ref.[32] and refs. therein).

While the aforementioned generation of studies was mostly using resonant degenerate four-wave mixing (using only one wavelength), the introduction of TC-RFWM further adds the features of double-resonant spectroscopy. Therefore, the coherent process of signal generation is dependent on both wavelengths being in resonance with transitions connected to a common

intermediate state. This allows to use one wavelength to select a single rovibronic transition within a single isotopologue of a target species. With this, spectra recorded by scanning the second wavelength are radically simplified, as the spectroscopy is no longer performed on a thermal distribution of a mixture, but, essentially, on a single rovibronically-defined quantum state of a single isotopologue of a species. Such a spectrum no longer contains anything, but rovibronic P, (Q,) and R lines of transitions connected to this quantum state. These unambiguously assignable lines directly allow to fit molecular constants. In addition, as all other lines of arbitrary strong bands disappear, weak features otherwise hidden become visible. This includes transitions of much weaker intensity, transitions involving spin-flips and, particularly, partially forbidden transitions that only become visible due to perturbation-facilitated, quantum-mechanical mixing of an optically forbidden dark state with a corresponding bright state in the same spectrum. While detection of spin-flip transitions allows to determine the spacing between the components of a multiplet and of spin-orbit *A* constants, the mixing of optically bright and dark states allows to quantitatively characterize the dark states and their strength of interaction with the bright state. To obtain this information in deperturbation studies, the pattern of such weak transitions is analyzed over a series of rotational levels. Next to selection rules and Frank-Condon overlap, the strength of perturbations is a function of the energetic spacing that the unperturbed rotational levels of bright state and dark state would have. For zero spacing, they would share their characters to equal parts and become identical. In spectroscopy this results in equal intensities for transitions into both levels. However, as quantum mechanics does not permit two identical levels at the same energy, the maximum of transition strength into the dark states is accompanied by a maximum of level repulsion. Performing the deperturbation, all observed transitions into the bright and dark state are used to simultaneously fit molecular constants and interaction strengths of

all contributing states, which for diatomic systems is often (including this work) performed by using the PGOPHER[33] software. The TC-RFWM process works independent of the common intermediate state being the upper or lower state. Therefore, also the mixed states, which are partially belonging to an optically inaccessible manifold, can be used. Consequently, TC-RFWM can be used for perturbation-facilitated optical-optical double resonance (PFOODR) spectroscopy.

To demonstrate the capabilities of (PFOODR) TC-RFWM spectroscopy, (without anticipation to the work on the copper dimer), our preceding work on the carbon dimer[34] shall be used. The description of the experimental setup is included in Chapter 2.4. Even so the carbon dimer has a singlet ground state, we could utilize thermal population in the just slightly higher-lying triplet state a as origin for of our TC-RFWM study. Tuning one wavelength to the (6,5) d-a band, we could access a perturbed vibronic level in the Swan bands, which is famous for its non-thermal emission in the tails of comets,[35] but was also observed when burning hydrocarbons at high pressures[35]. It took a complete century until in our laboratory, using almost the same setup we still use for this work, experimental verification was provided that the d (v=6) level is perturbed by the lowest-lying quintet state $1\,^5\Pi_g$.[36] Using these perturbed levels as gateways, we could perform a PFOODR study of the quintet manifold where could detect the first quintet-quintet band in C_2 (Figure 3), which probes the predissociative state $1\,^5\Pi_u$ (Figure 4). The significant population of the quintet states, which causes the non-thermal emission from the Swan bands, was finally explained by Babb *et al.* in 2019, when they calculated that the $1\,^5\Pi_u$ - $1\,^5\Pi_g$ transition is the dominant channel for radiative association during the collision of two ground-state carbon atoms.[37]

Figure 5 illustrates the spectral simplification based on exemplary spectra. For comparison, we added a simulated absorption spectra to Figure 5d.

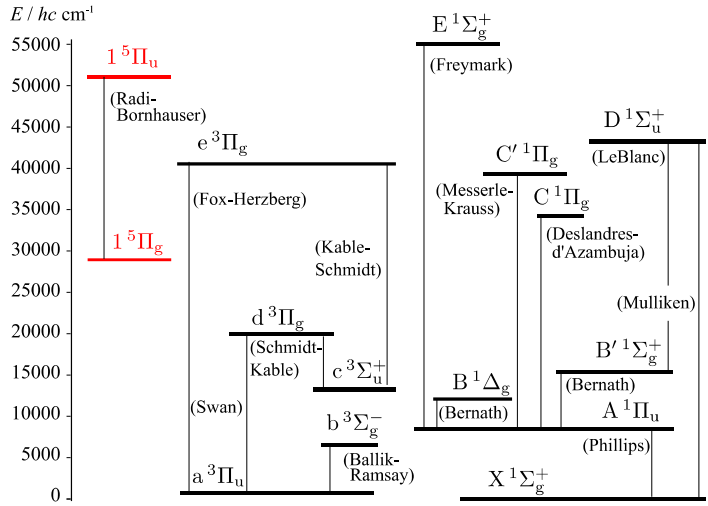

Figure 3: Low-lying singlet, triplet, and quintet electronic states of C_2.

A downside of using TC-RFWM as spectroscopic method is the complex, nonlinear process of signal generation, depending on the number density of the target species as well as on the powers of the lasers.[38] This makes it difficult to do an analysis based on absolute line intensities or line shapes. Even when just line positions are needed, like it applies for our work presented here, it is easy to misinterpret the signal. For illustration, we included a spectrum with a strong saturation on the probe wavelength into Chapter 4 (Figure 15, p. 54). In this example, the intensity-broadened probe beam was tuned to a band head, where it caused a dip on the fully resonant transition, but signal from the neighboring lines still produced a (useless) spectrum. However, when optimizing the setup on a separated (well-known) line, a single beam of too small or too strong intensity can totally annihilate the signal generation. If this problem is not recognized, it is easy to totally lose the alignment while trying to find the signal again. Including the phase matching, which, working in a thin molecular beam, is adjusted by changing the angle at which the beams enter the common focus, the four-wave mixing process includes 16 spatially degrees of freedom. Adding timings, molecular

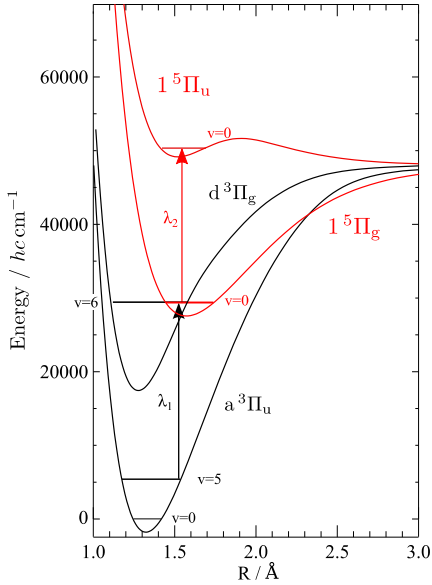

Figure 4: PFOODR scheme for the detection of 1 $^5\Pi_u$ in potential energy diagram. The pump wavelength λ_1 excites to a mixed state (1 $^5\Pi_g$ *v*=0) that gains triplet intensity from the bright Swan system (d-a). From there, the probe wavelength λ_2 excites the 1 $^5\Pi_u$ *v*=0 state (red arrow). Ab initio potential energy curves were computed at the MRCI level of theory with a large basis set.[§]

beam source conditions, scattered light (mistaken for a signal), polarization, focusing, etc., it can easily take days to rediscover the signal, even for a skilled experimenter. Building a TC-RFWM spectroscopy setup for studies on molecular beams from scratch, it can easily take one year until the first real signal is observed. However, once these difficulties are handled, one is rewarded with a spectroscopic method of exceptional properties.

[§] Figures 3-5 were reprinted from P. Bornhauser, R. Marquardt, C. Gourlaouen, G. Knopp, M. Beck, T. Gerber, J.A. van Bokhoven, P. Radi, "Perturbation-facilitated detection of the first quintet-quintet band in C_2", *J. Chem. Phys.*, 2015, **142**, 094313, with the permission of AIP Publishing.

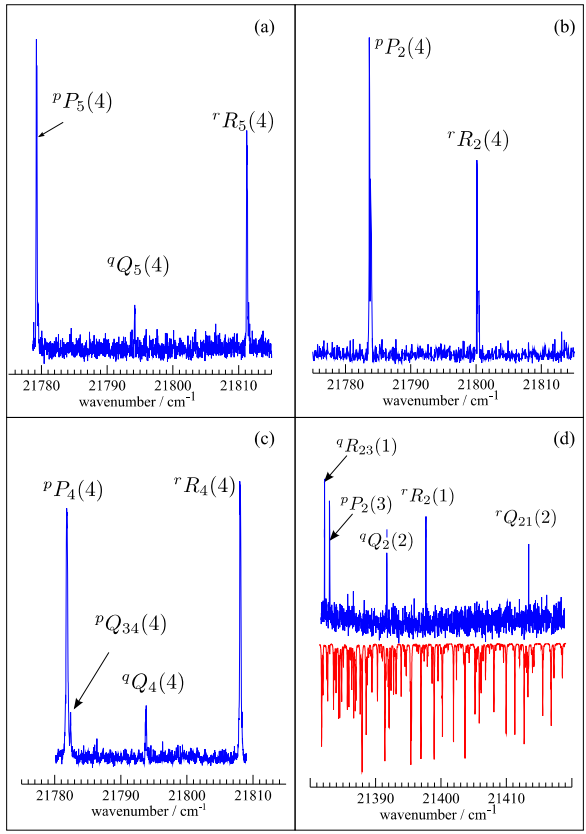

Figure 5: PFOODR by TC-RFWM. Panel (a)-(c) are obtained by selecting intermediate levels exhibiting significant 1 $^5\Pi_g$ character by the pump wavelength in the d-a band and scanning the probe wavelength. From the nominal $F_5(4)$ level of the "dark" 1 $^5\Pi_g$ electronic state with 83% quintet character three transitions to 1 $^5\Pi_u$ state in the P, Q, and R branch are observed (a). By addressing the $F_2(4)$ intermediate level shown in panel (b), the Q branch is not observed because this spin-substate is mainly a Ω=0 state ($^5\Pi_{0g}$). Panel (c) is obtained by tuning the pump wavelength to excite the intermediate level $F_4(4)$. In addition to the three spin-allowed transitions in the P, Q, and R branch, a weak satellite is observed linking the F_4 level with a F_3 term. Such cross transitions allow an accurate determination of the spin-orbit A constant of the 1 $^5\Pi_u$ state. Panel (d) shows exclusively rotational transitions from the a $^3\Pi_u$ v=5 state to levels of the "dark" 1 $^5\Pi_g$ state. Here, the probe wavelength is fixed on the $^qP_2(2)$ transition of the 1 $^5\Pi_u$ - 1 $^5\Pi_g$ system and the pump wavelength is scanned in the wavenumber region of the Δv=1 sequence bands of the Swan system. For comparison, a simulation of the dense and complex absorption spectrum is shown in red.

2.3.1.2 *Laser induced fluorescence spectroscopy*

Declaration: this chapter illustrates our usage of the method using the example of [P. Bornhauser, B. Visser, M. Beck, G. Knopp, J. A. van Bokhoven, R. Marquardt, P. P. Radi, "Experimental and theoretical investigation of the vibrational band structure of the $1^5\Pi_u$–$1^5\Pi_g$ high-spin system of C_2", *J. Chem. Phys.*, 2017, **146**, 114309] where the author did the laser induced fluorescence measurements and partially contributed to the two-color resonant four-wave mixing measurements

While the principles of laser induced fluorescence (LIF) are well beyond the stage of needing explicit introduction, a few words shall introduce its application as complementary channel of information in our work both on the carbon and the copper dimer. Simultaneous collection of LIF signal through a spectrometer (Chapter 2.4.2) is a convenient tool to monitor the output of a molecular beam source in a two-color experiment. Often, one laser is fixed on a transition originating in the ground state. Therefore, by monitoring fluorescence from the thereby excited state into a neighboring vibrational channel of the ground state, the LIF signal is linearly coupled to the number density of the target species in the molecular beam. In principle, spectral hole-burning introduces dips in this signal in cases when double-resonances with the second laser occur, but as this is in no way competitive to TC-RFWM, we did not use this for analysis.

Instead of monitoring the ground state population, in a follow-up study on the carbon dimer, we utilized LIF in our PFOODR measurements. Exciting the $1\,^5\Pi_u$ state as already shown in Figure 4, we utilized LIF to measure the v=1 and v=2 levels of the $1\,^5\Pi_g$ state. By scanning the spectrometer starting at the excitation towards longer wavelength, these bands become visible (Figure 6). However, as the LIF signal contains more than just fluorescence from the $1\,^5\Pi_u$ state, an on/off measurement was necessary to subtract the one-color background.

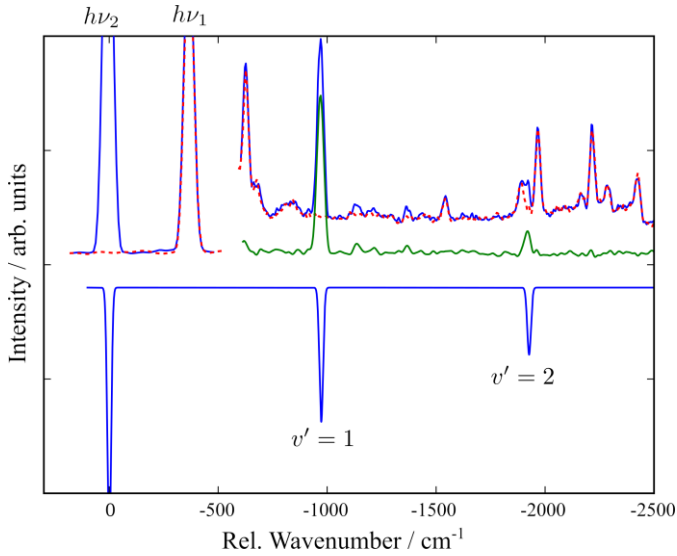

Figure 6: ON/OFF dispersed fluorescence from the 1 $^5\Pi_u$ v = 0 level excited by applying PFOODR. The abscissa is the wavenumber shift from the exciting $P_2(5)$ line in the (0,0) 1 $^5\Pi_u$ - 1 $^5\Pi_g$ band. The red (dotted) trace is observed by turning hν_2 OFF. LIF from both lasers ON is shown in blue (solid). Both traces are offset below -500 cm^{-1} for clarity. The difference spectrum (green, solid) displays the vibrational progression with v = 1 and 2. Inverted shown is a simulation by taking into account the vibrational frequencies obtained by *ab initio* computations.[**]

In our work on the copper dimer, we used LIF to rotationally resolve a dark vibronic state using only one laser. For this, we tuned the spectrometer to a vibronic band in the dark manifold and did an excitation scan on a perturbed bright state. The detection in the dark manifold produced a complementary spectrum where, in contrast to the TC-RFWM measurements, the rotational lines of the dark state are seen also further away of the intersection with the bright state, while the lines originating in the bright state rapidly disappear. More details of these findings are discussed directly in Chapter 5.3.3.

[**] Reprinted from P. Bornhauser, B. Visser, M. Beck, G. Knopp, J. A. van Bokhoven, R. Marquardt, P. P. Radi, "Experimental and theoretical investigation of the vibrational band structure of the $1^5\Pi_u$–$1^5\Pi_g$ high-spin system of C_2", *J. Chem. Phys.*, 2017, **146**, 114309, with the permission of AIP Publishing.

2.3.2 Theoretical

The work on the carbon dimer, which was used to introduce the experimental methods in Chapter 2.3.1, was supported by quantum chemical *ab initio* calculations using the multireference configuration interaction (MRCI) method. Among the *ab initio* methods, MRCI is one of the few that is capable to consider the non-adiabatic coupling among excited electronic states. However, a common property of well-established methods providing these capabilities is their exponential scaling with the number of determinants. Therefore, these are typically limited to consider 16 electrons and orbitals. Still, for the 12 electrons of the carbon dimer, a straightforward application was possible. The details are omitted here, but can be found in our related publications.[34,39,40] A in depth review of such methods and their applications was provided by Szalay *et al*.[41]

For the 58 electrons of the copper dimer, a straightforward application of such methods is not possible. It is possible to exclude a frozen core of inner shell electrons around each atom, but still, prior to this work, there were no successful attempts to reproduce the experimentally known electronic states. While the high-lying electronic states are well beyond the scope of the well-established *ab initio* methods, Chapter 4.3 demonstrates how to apply them in order to reproduce the low-lying electronic states in good agreement with the experimental findings. To provide the background needed to follow the theoretical findings within Chapter 4, the following chapter will give a brief introduction into scope and methods used.

2.3.2.1 *Theoretical treatment of Cu_2*

Declaration: this chapter is utilizing part of [B. Visser, M. Beck, P. Bornhauser, G. Knopp, J. A. van Bokhoven, R. Marquardt, C. Gourlaouen, P. P. Radi, "Identification of a new low energy 1_u state in dicopper with resonant four-wave mixing", *J. Chem. Phys*., 2017, **147**, 214308] to introduce the concepts on which the theoretical results of chapter 4.3 were established. It is only provided for completeness, as the author of this thesis did mostly contribute to its experimental part.

In this work we report theoretical results on the ground state X $^1\Sigma_g^+$ and the following excited states: the lowest two $^1\Sigma_u^+$ and $^3\Sigma_u^+$ levels, the lowest $^1\Pi_u$, $^3\Pi_u$, $^1\Delta_u$, and $^3\Delta_u$ levels.

Potential energy functions were calculated at the internally contracted multi-reference configuration-interaction (briefly MRCI) level of theory[42-44], using single and double excitations, an estimation for corrections due to higher order excitations from the Davidson formula for cluster correction (MRCI+Q) and the aug-cc-PVQZ-DK (AVQZ-DK) basis as implemented in the MOLPRO program suite[45]. The Douglas-Kroll-Hess Hamiltonian[46,47] was used at order four to estimate relativistic corrections beyond spin-orbit interactions. The AVQZ-DK basis has originally been optimized using the coupled cluster method with perturbational inclusion of triple excitations (CCSD(T))[48]. Test calculations have shown that it is possible to use the AVQZ-DK basis at the MRCI level.

An important step prior to the MRCI+Q calculations is the determination of an optimal active space. The best choice has proven to be the calculation of optimal orbitals from a state averaged multi-state self-consistent field calculation (MCSCF) using a reduced active space involving all 22 valence electrons in 18 orbitals, a (22,18)-RAS. The active orbital space is composed of the 3d, 4s and 4p orbitals. Calculations in a (22,18) complete active space (CAS) are too costly to be run efficiently. Instead, we have optionally removed all double excitations of 3d orbitals from the active space, defining in this way a reduced active space of states.

The states included in the MCSCF calculation were the 23 singlet states that can be obtained from the (22,18)-RAS and that correlate with the two lowest dissociation asymptotes. The lowest asymptotes correspond to the $3d^{10}4s^1$ + $3d^{10}4s^1$ electronic configurations of separated copper atoms, which we call the ss separated atoms limit. The next lowest correlate with the $3d^{10}4s^1$ + $3d^94s^2$ configurations - also referred to as “d-hole” configurations, which

compose the sd separated atoms limit. In (22,12)-CAS calculations, which have also been investigated in the course of this work, a third type of asymptotic channels is possible, if double excitations from 3d orbitals are considered: $3d^9 4s^2 + 3d^9 4s^2$ configuration, the dd separated atoms limit. Each channel may contain singlet (S) or triplet (T) levels, which may additionally be distinguished as neutral (N) or charged (C) levels, where a charge separation into $Cu^+ + Cu^-$ occurs asymptotically. These states may be named charge transfer states and are also referred to as ion-pair states; the corresponding separated ion limits are indicated as ss, sd, dd, respectively, in Table 2, which summarizes the partition of the $\binom{22}{12} = 276$ valence states that can be obtained from a MCSCF or MRCI calculation in the (22,12)-CAS.

For the (22,18)-RAS calculations, only states belonging to the ss and sd separated atoms limit in Table 2 were considered. States indicated by dd belong to double excitation from 3d orbitals and were excluded in the RAS-calculations. Indeed, electronic correlation inferred from double excitations

Table 2: Number of singlet (S) and triplet (T) states in the (22,12)-CAS per irreducible representation of the D_{2h} point group, and their distribution as neutral (N) or charge transfer states (C), and whether the dissociation corresponds to the $3d^{10}4s^1 + 3d^{10}4s^1$, the ss separated atoms limit, or to the $3d^{10}4s^1 + 3d^9 4s^2$, the sd separate atoms limit, or to the $3d^9 4s^2 + 3d^9 4s^2$, the dd separate atoms limit. Separated ion limits in the case of charge transfer states are indicated correspondingly. All states of the lines given in italics correspond to the latter dissociation channel and were excluded from the (22,18)-RAS.

Limit		A_g	B_{3u}	B_{2u}	B_{1g}	B_{1u}	B_{2g}	B_{3g}	A_u	Tot
N	ss	1S	…	…	…	1T	…	…	…	1S+1T
	sd	2S+2T	1S+1T	1S+1T	1S+1T	2S+2T	1S+1T	1S+1T	1S+1T	10S+10T
	dd	*6S+1T*	*3S+3T*	*3S+3T*	*3S+3T*	*1S+6T*	*3S+3T*	*3S+3T*	*3S+3T*	*25S+25T*
C	ss	1S	…	…	…	1S	…	…	…	2S
	sd	2S+2T	1S+1T	1S+1T	1S+1T	2S+2T	1S+1T	1S+1T	1S+1T	10S+10T
	dd	*6S+1T*	*3S+3T*	*3S+3T*	*3S+3T*	*6S+1T*	*3S+3T*	*3S+3T*	*3S+3T*	*30S+20T*

of the 3d orbitals has been found to be less important than that inferred from excitation into additional 4p orbitals. It is known that inclusion of 3d orbitals, or orbitals alike, the so-called 3d' orbitals, is necessary to improve on the calculation of the electronic correlation in transition metals.[49,50]

It is also known that the MCSCF levels of copper are inverted with respect to experiment[51]: dd levels (see Table 2) lie below the sd and below the ss levels at the MCSCF level of theory. Therefore, in a (22,12)-CAS the reference level giving rise to the dominant $d^{10}s^1$ configuration of the $^1\Sigma_g^+$ ground state is level number 9, from Table 2. In the (22,18)-RAS reported in the present work, state number 3 is the reference level that correlates with the expected ground state configuration. Charge transfer states are not involved in this inversion of states.

One has therefore to calculate at least 3 states of symmetry 1 (A_g) in the MRCI program in order to grasp this level correctly. Similarly, one has to calculate at least 3 states of symmetry 5 (B_{1u}) in the MRCI program to grasp the lowest $^3\Sigma_u^+$ ($^3B_{1u}$) level. Even though charge transfer states are not involved in the inversion of states at the MCSCF level of theory, their inclusion into the set of states to be calculated at the internally contracted MRCI level of theory has shown to yield a clear improvement of the energy of the levels reported in this work. Specifically, the following number of roots were calculated at the internally contracted MRCI level: Four in ^1A_g, three in singlet and triplet B_{1u}, one in each of singlet and triplet B_{3u}, B_{2u}, and A_u.

Following this rationale, it was possible to obtain the whole set of levels pertaining to the neutral ss and sd asymptotes. Because of the complete disorder between MCSCF reference and MRCI states, the Davidson cluster correction needs to be calculated with respect to the rotated reference state (i.e. use the MOLPRO variable $\mathrm{energd3}$ for energies referring to relaxed coefficients in the rotated reference state).

While Table 2 is of practical relevance for theoreticians, it does not directly convey the information relevant to the spectroscopic states in the $D_{\infty h}$ point group. The corresponding neutral states in the ss separate atoms limit decompose as $^1\Sigma_g^+(^1A_g)$ + $^3\Sigma_u^+(^3B_{1u})$. In the sd separate atoms limit, the corresponding states are $\Sigma_g^+(A_g)$ + $\Sigma_u^+(B_{1u})$ + $\Pi_g(B_{2g}+B_{3g})$ + $\Pi_u(B_{3u}+B_{2u})$ + $\Delta_g(A_g+B_{1g})$ + $\Delta_u(B_{1u}+A_u)$, each as one singlet and one triplet state. Other important states in the present study stem from the ss limit of separate ions, i.e. charge transfer states with configurations of the type $3d^{10}4s^0$ + $3d^{10}4s^2$: $^1\Sigma_g^+(^1A_g)$ + $^1\Sigma_u^+(^1B_{1u})$. The latter will in particular be relevant for the assignment of the G state in Cu_2, as will be discussed below.

Spin-orbit levels are finally computed from diagonalization of the Breit-Pauli operator represented in the basis of MRCI wavefunctions as implemented in the MOLPRO program package[45]. The latter exclude cluster corrections. In order to estimate the effect from cluster corrections on the spin-orbit levels, we noticed that the Davidson correction leads to an energy shift of the MRCI spin-eigenfunctions which can be simply related to an energy shift of corresponding spin-orbit eigenfunctions. Davidson corrected spin-orbit energies have hence been obtained by the formula

$$E_{\mathrm{MRCI+Q}}^{(\mathrm{SO})} = E_{\mathrm{MRCI}}^{(\mathrm{SO})} - E_{\mathrm{MRCI}} + E_{\mathrm{MRCI+Q}}, \qquad (1)$$

where E_{MRCI} and $E_{\mathrm{MRCI+Q}}$ are spin-eigenstates obtained at the MRCI level of theory without and with the Davidson correction, $E_{\mathrm{MRCI}}^{(\mathrm{SO})}$ is the energy obtained from diagonalization of the Breit-Pauli operator and $E_{\mathrm{MRCI+Q}}^{(\mathrm{SO})}$ contains the estimated Davidson correction to the latter.

Relevant spin-orbit levels in this report are 0_u^+ and 1_u levels, in Hund's case (c) notation, as these are the only states accessible from the X $^1\Sigma_g^+$ ground state via optical excitation in the electric dipole approximation. Spin-orbit to spin-eigenstate correspondences used in connection with Eq. 1 and verified

from inspection of the output of the MOLPRO program are given in the correlation Table 3:

In addition to the 0_u^+ and 1_u levels, spin-orbit calculations involving the ungerade states in the ss and sd separated atoms limit yield 0_u^-, 2_u and 3_u levels. When all neutral and charge transfer states considered in the present calculation are included, the spin-orbit matrix has rank 28. These states separate as 4 A_g and 6 of each B_{3u}, B_{2u}, B_{1u}, and A_u irreducible representations of D_{2h}. Among the B_{3u} states one finds one component of the 1_u and 3_u levels

Table 3: Correspondence of the ungerade spin-orbit levels (in Hund's case (c) notation, right hand side) to spin-eigenstates using notations from the $D_{\infty h}$ point group (left hand side). Reported are all ungerade states belonging to the ss separated atoms and ions limits, as well as those belonging to the sd separated atoms limit (see text and Table 2). Electronic term values T_e are given in units of cm^{-1} and were evaluated at the MRCI+Q level of theory at the interatomic distance of 220 pm, where the reference is the minimum of the X $^1\Sigma_g^+$ ground state.

Spin eigenstates		Spin-orbit states	
2 $^1\Sigma_u^+$	34567	34611	3 0_u^+
2 $^3\Sigma_u^+$	31758	31867	2 0_u^-
		31867	4 1_u
1 $^1\Delta_u$	27325	28005	3 2_u
1 $^3\Delta_u$	26886	27785	3 1_u
		26249	2 2_u
		26051	1 3_u
1 $^1\Pi_u$	23177	23264	2 1_u
1 $^1\Sigma_u^+$	22672	22935	2 0_u^+
1 $^3\Pi_u$	21750	22145	1 0_u^-
		21925	1 0_u^+
		21552	1 1_u
		21267	1 2_u
a $^3\Sigma_u^+$	17404	17404	a 0_u^-
		17404	a 1_u

(the other component being among the B_{2u} states), among the B_{1u} states one finds 0_u^+ and one component of the 2_u levels, and curve crossings may occur. The correct assignment of levels and manual crossing was indeed necessary at several values of the inter-atomic distance r and carried out by inspection of the eigenvectors of the spin-orbit matrix, which vary as functions r. Only the relevant lowest states in each irreducible representation are finally reported in Chapter 4.3.

Table 3 is in line with the correlation diagram for the AgF molecule presented in ref.[52] but for the position of the $^1\Sigma^+$ level, which lies below the $^3\Pi$ in AgF. Also, the signs of the relative shifts of the spin-orbit states with respect to the spin-eigenstates are somewhat different in AgF.

2.4 Experimental Setup

Declaration: the author contributed improvements to the apparatus discussed in each subchapter, but mostly worked on preexisting designs.

This chapter provides an overview of the experimental setup used to perform this work. It is meant as a reference to describe the principal apparatus needed to reproduce these experiments. Full details of the implementation were provided in previous work[53] and are kept brief unless they were significantly revised. The original depiction as provided in ref. [53] is reproduced as Figure 7.

2.4.1 Vacuum Setup

Core of the experiment is the main vacuum chamber (Figure 7), where laser spectroscopy is applied in a molecular beam. As neutral species in a molecular beam cannot be refocused and a high number density is required for signal generation by non-linear methods, the source for this beam is also placed directly into this chamber. At the end of the main chamber, a skimmer[††]

[††] A skimmer is an inverse funnel used to cut out a fraction of a molecular beam

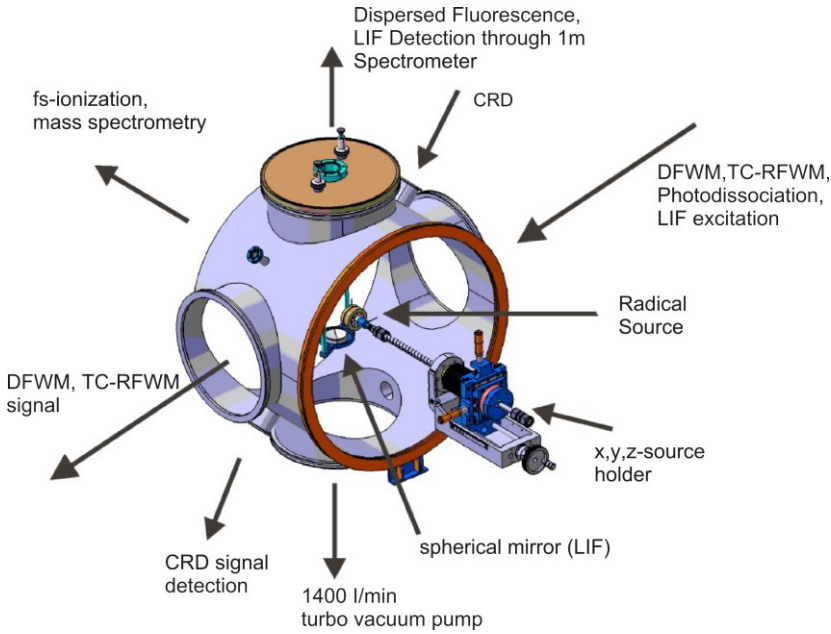

Figure 7: Original depiction of the "molecular beam apparatus for multiplex spectroscopy".[53,‡‡]

passes a fraction of the molecular beam into a smaller chamber where time-of-flight mass spectroscopy can be applied. In this second chamber, the neutral species are ionized by a focused laser pulse, which also provides the time zero. Theses ions are then accelerated towards a reflectron[§§], from where only the cations generated in the second chamber finally reach a Daly detector. The mass trace is then recorded using an oscilloscope. In normal operation, non-resonant multi-photon ionization by a titanium-sapphire laser (800 nm, <100 fs, 0-700 µJ) is used to ionize virtually any species except

‡‡ Reprinted from J. Raman Spectrosc. 38, Tulej *et al.*, Multiplex spectroscopy of stable and transient species in a molecular beam, pp. 1022–1031, Copyright (2007), with permission from John Wiley and Sons.

§§ A reflectron is an ion mirror using a defined electric field gradient to compensate for different kinetic energies of ions. Providing a longer path for fast ions, it ensures that ions of identical mass reach a detector at the same time

helium. As an alternative mode of operation, one of the dye lasers used for spectroscopy, *vide infra*, can be used to do resonance-enhanced multi-photon ionization. This allows an initial search for optical transitions in a target species, which is identified by its mass, respectively its isotopic pattern. Having identified an initial set of lines belonging to the target species, these lines can then be utilized for the spectroscopy performed in the main chamber.

2.4.2 Optical spectroscopy setup

The optical spectroscopy is performed using two Nd:YAG-pumped (10Hz) dye lasers (NarrowScan, Radiant Dyes, 0.04 cm^{-1} specified line width). Pumped at 532 or 355 nm, they provide pulses of about 10 ns length over almost the complete visible range. By application of second harmonic generation, this range can be extended into the deep ultraviolet regime. These beams are then split as needed to provide the three incident beams for resonant four-wave mixing spectroscopy (TC-RFWM; described in chapter 2.3.1.1.). In our setup we use a forward BOXCARS configuration[54], focusing three laser beams through a common lens (2" diameter, f=1000mm) into the molecular beam, which is located in the center of the vacuum chamber. Thereby, the phase matching condition required by the spectroscopic method can be adjusted by changing the displacement between the individual laser beams and the parallel running optical axis of the lens. Beforehand, the laser beams are conditioned using a varying combination of telescopes, attenuators, spatial filters, and irises, to optimize signal generation and to minimize stray light. To allow fine adjustment of the spatial overlap on a fluctuating signal, the last mirrors are motorized. This allows to record the signal over the mirror axis and to determine the center position by means of fitting. A wavelength meter (WS 6, HighFinesse/ 166 Ångstrom) is used to calibrate and monitor the dye laser output. Photodiodes (Thorlabs, 1 GHz bandwidth) are used to monitor the second harmonic generation.

For detection of the TC-RFWM signal, the three incident laser beams are dumped after passing the molecular beam, to avoid any background produced by multiple scattering in the output window. Only the spatially separated signal beam leaves the vacuum chamber and is re-collimated by a second lens, which is identical to the focusing lens in front of the chamber. After passing an iris and a few mirrors providing additional three meters of separation, the signal beam is focused through a pinhole onto a photomultiplier tube (Hamamatsu H3177). This distance helps to separate the laser-like signal beam from the isotropically emitted fluorescence, which is also produced frequently by the probed species in the molecular beam. Depending on the intensity of the studied transitions, additional filters are placed in front of the photomultiplier to avoid saturation resp. damage. As a complementary method, laser induced fluorescence (LIF; described in chapter 2.3.1.2) spectra are measured in parallel. For this, a spherical mirror below the laser focus collimates the fluorescence onto a window atop of the vacuum chamber. A further mirror and a lens then focus this light onto the slit of a spectrometer (SPEX, 1m). The dispersed fluorescence signal is then recorded using a further photomultiplier tube. The output of the photomultipliers and photodiodes are recorded on a digital storage oscilloscope (LeCroy HD6104-MS) and the peak areas values of the averaged waveforms are used as intensity values. Plotting of these over the output of the wavelength meter yields the final spectra for four-wave mixing or excitation scans; for dispersed LIF scans the spectrometer position provides the abscissa.

2.4.3 Timing Setup

To provide the timings for the setup up to 5 cascaded/branched delay generators (DG535, Stanford Research Systems, 4 edges or 2 pulses) were used. While they provide 2 signals per pump laser and 2-3 signals for the molecular beam source, some of them at the same time act as frequency dividers (by setting one channel to a time larger than the trigger period). By

full integration into the experimental control (GPIB), the delay generators also allow scans in the time domain (overlap optimization, source characterization, lifetime studies on the ns scale). Performing optical spectroscopy, the master clock is provided by the first delay generator in the chain. When also TOF mass spectrometry is used, the oscillator of the titanium-sapphire laser, which is divided down and amplified at about 100 Hz, acts as master clock. Its amplifier trigger also triggers the first delay generator, which then times the master trigger in order to have the pulsed molecular beam in the ionization chamber when the next femtosecond pulse is fired. To have time zero for the mass spectroscopy, a descendant of the master trigger is used to arm the trigger system of an oscilloscope that is then triggered by the next pulse of the titanium-sapphire laser.

2.4.4 Slit discharge radical source

While the main results of this work were achieved using the cluster source discussed in Chapter 3, the experimental work used to illustrate the methodology (Chapter 2.2) was mostly done using a slit discharge radical source originally developed by Linnartz[55] and illustrated in Figure 8. For these experiments on C_2,[34,39] we used a similar design mounted on a pulsed valve (Series 9, Parker, 2 mm orifice). To supply this valve, about 1% of acetylene was diluted in argon buffer gas and applied at backing pressures between 5 and 11 bar. After stretching the gas pulses by the multi-channel body, molecular pulses of about 750 µs duration were emitted into the chamber. An electrical pulse of -800 to -900 V and about 2 µs duration is applied during this expansion to break down the precursor by use of an electrical discharge. This results in a large variety of products, including a significant amount of C_2. The slit geometry was chosen to increase the spatial overlap with the laser beams passing along the slits in a distance of about 5 mm.

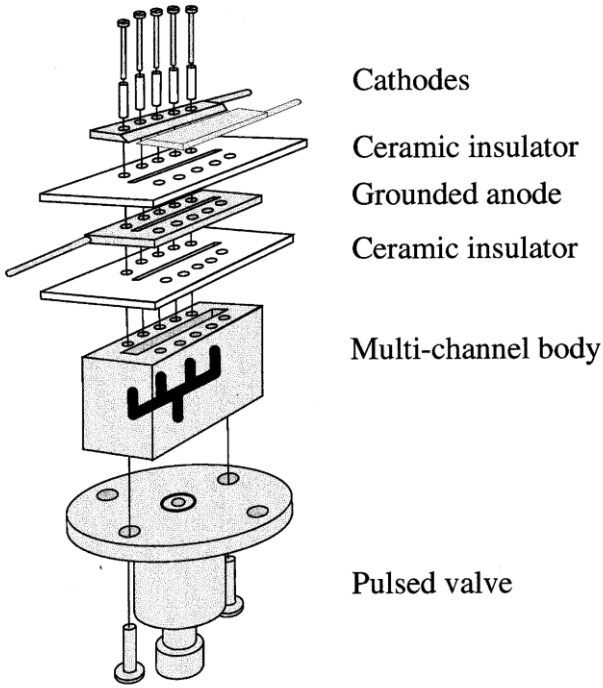

Figure 8: Original depiction of the slit source design.[56,***]

***Reprinted from Chem. Phys. 283, Birza *et al.*, Cw cavity ring down spectroscopy in a pulsed planar plasma expansion, pp. 119–124, Copyright (2002), with permission from Elsevier.

3 Cluster Source

Declaration: the author did not contribute to the initial design, but the commissioning and design revisions needed to achieve stable operation were mainly contributed by the author. The first functional version was reported in a spectroscopic paper written by Bradley Visser, where the author contributed equally to the underlying experimental work [B. Visser, M. Beck, P. Bornhauser, G. Knopp, T. Gerber, R. Abela, J.A. van Bokhoven, P.P. Radi, "Unraveling the electronic structure of transition metal dimers using resonant four-wave mixing", *J. Raman Spectrosc.*, 2016, **47**, 425-431.].

3.1 Introduction

The cluster source used for the studies on the copper dimer was designed at the Paul Scherrer Institut. It follows the basic idea of a "standard" laser vaporization source[57]. In such a source, typically, a pulse of rare gas is fired into a channel that passes over the surface of a rotating rod of target material. Synchronized to the arrival of the gas pulse, a laser pulse enters through a small hole in the channel wall opposing the target rod and ablates a portion of the sample material. The resulting plasma bloom of target material is entrained in the gas pulse, which subsequently flows through a growth channel, where cooling and cluster aggregation takes place. Finally, the cluster containing gas pulse is expanded into high vacuum, where a cluster containing molecular beam emerges by supersonic expansion.

Given the high requirements on number density and stability of the target species in the molecular beam, which is required to utilize TC-RFWM spectroscopy (Chapter 2.3.1.1), the target rod was replaced by a 2D motion-controlled target disk. This allows to provide a fresh piece of surface for each shot of the ablation laser. Further, it enables usage of regular sputter targets instead of custom-made rods. In addition, instead of using a disk of bulk target material, a rare target material can also be provided as a thin coating

on one side of the target disk. Figure 9 shows a schematic of the first working version of the cluster source at the end of the initial commissioning phase.

The source is built around an aluminum base plate in which a 2 mm wide channel is embedded.[†††] Using a pulsed valve (Parker general valve, series 9, 1 mm diameter orifice), backed by up to 50 bar of helium, gas pulses in the order of a few 100 µs length were fired into the channel. At the center of the base plate, the channel expands to open towards a target disk (standard sputter target dimensions: 50 mm diameter, 3 mm thick). To avoid extensive dead volume between target surface and base plate, a milled PEEK ring surrounding the target not only forms a gas seal, but also defines the distance between target and base plate. The complete assembly consists of

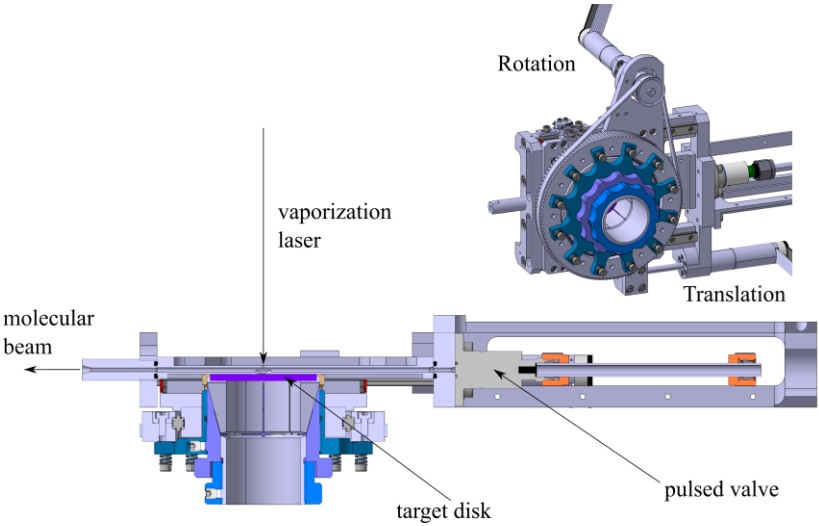

Figure 9: Schematic of the Cluster Source in its state at the end of commissioning.[‡‡‡]

[†††] In Ref. [58], 1 mm was erroneously reported, but 2 mm is the correct value.

[‡‡‡] Reprinted from B. Visser, M. Beck, P. Bornhauser, G. Knopp, T. Gerber, R. Abela, J.A. van Bokhoven, P.P. Radi, "Unraveling the electronic structure of transition metal

a target, a PEEK ring, and a holder, which is spring-loaded to form a reliable seal towards the base plate. It is further mounted on a rail system and linearly moved by an in-vacuum motor (Maxon). A ball bearing between target assembly and rail system allows rotational motion driven by a second motor and a belt. In combination, this allows a turntable-like motion, so that the complete target surface can be addressed by the ablation laser pulses (Continuum, NY81, ≤100 mJ @ 532 nm, ~10 ns pulse length). These pulses were focused outside of the vacuum chamber by a f = 500 mm lens. The focus was slightly shifted out of plane of the target in order to have optimum ablation conditions over a spot size of a few tenth of millimeters. This was necessary, as at the used ablation energies of 10-100 mJ plasma shielding would have limited the amount of ablated material on using a tighter focus. On the side opposing the target, a hole of 1 mm diameter was drilled into the base plate to allow incidence of the ablation laser pulses. Finally, interchangeable nozzles were screwed tight to the end of the growth channel. Limited by the lasers for spectroscopy, the cluster source was used at 10 Hz repetition rate.

3.2 Electromechanical position control

Both motors were equipped with encoders to track the motion. For the linear motion, end switches provided a way for zeroing. For the rotational axis only relative positions are known. During spectroscopic measurements on bulk targets, both motors where used in constant velocity mode, with the linear axis moving at about 0.14 mm/h and the rotational at 12 RPM. The latter was chosen to have 1 full rotation while recording 50 averages using the 10 Hz experiment. Especially in the early stages of the cluster source, this was necessary to average over the position-dependent tightness of the seal, but was kept up so far for all but the fastest survey scans, for which the

dimers using resonant four-wave mixing", *J. Raman Spectrosc.*, 2016, **47**, 425-431, with the permission of John Wiley and Sons.

averaging was reduced. In the early phase, there were several attempts to use other control schemes. However, the backlash of the linear motion would require to approach each target position from the same direction. For the rotation it is even worse, as the toothed belt introduces elasticity. Therefore, at slow velocities, stick-slip phenomena occur and the motor encoder can no longer be used to precisely determine the actual position. Given these effects, more advanced control schemes were postponed to prospective redesigns.

3.3 Seal tightness and metal vapor uptake

Over the course of this project, the management of the gas pulse was the most crucial aspect of this experiment. Whenever the target was insufficiently sealed, a large portion of the metal vapor was pushed into the gap between base plate and target. Therefore, the metal vapor density in the growth channel was not sufficient for cluster formation and growth. As the distance between the pulsed valve and the ablation spot is much larger, compared to typical rod-based vaporization sources, a large volume flow of buffer gas is needed to have sufficient pressure in the growth channel to enable cluster formation. To produce sufficient number density for applying non-linear spectroscopy, we had to push the general valves beyond their range of stable operation. After sufficiently revising the seal between target and base plate, the entrance hole for the ablation laser was identified as major source of pressure loss. The not always perfectly aligned ablation laser was increasing its diameter over time. To fix this, the circumstance that the laser focus was in front of the target surface was utilized. By clamping a (black anodized) aluminum foil behind an alignment tool glued over the laser hole, the ablation laser shot its own pinhole for entering the source. This foil could be replaced whenever breaking the vacuum. Figure 10 shows the cluster source with this workaround applied. In case of the clamping being too loose, more than one foil could be inserted to provide a better seal. As

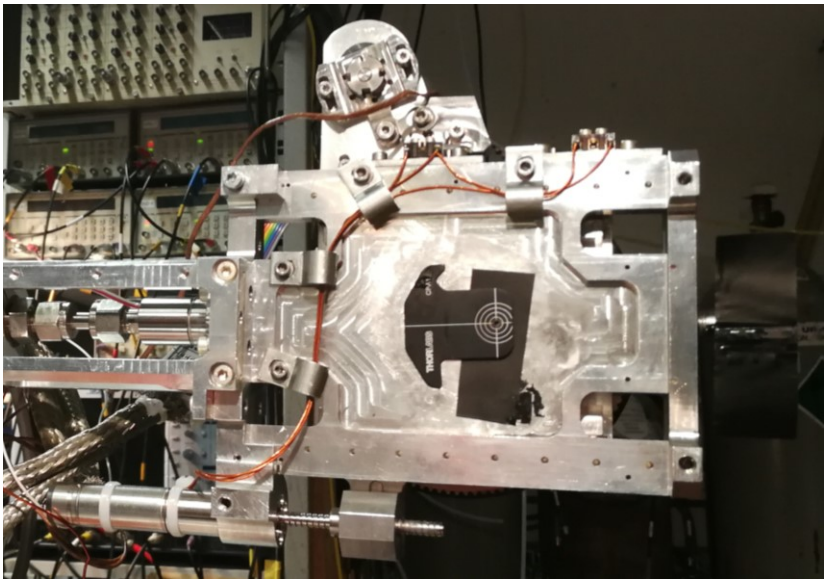

Figure 10: Cluster source with improvised pinhole for the ablation laser pulses. An additional piece of black anodized aluminum foil covers the nozzle to prevent stray light from being reflected from the nozzle towards the spectrometer.

the foil is close to the focus of the laser beam, the pinhole is burned almost immediately after switching on the ablation laser.

But even with reworking the seal around the target, and adding a pinhole on the laser input side, stable conditions were only achieved for the copper dimer. Larger copper clusters would have depended on higher pressure or longer residence time in the growth channel. The first could not be achieved due to the limitations of the general valve. Trying the latter, by introducing obstacles between growth channel and nozzle, did not succeed, as then again the aerodynamic resistance of the channel became comparable to the resistance of the pinhole and the metal vapor did no longer reach the nozzle.

3.4 Obtained mass spectra

Figure 11 shows a copper mass spectrum obtained with this cluster source. As mentioned in the previous chapter, mostly the dimer was produced. Still, the identity of the species is unambiguously determined as the expected pattern of isotopologues exactly matched the expectations. Also the even-odd alternation in intensities is reproduced as thermodynamically expected for copper atoms with a single 4s electron. As the mass spectroscopy was performed without pumping overnight, H_2O^+ is visible in all spectra.

Figure 12 shows a similar spectrum obtained after installing a carbon sputter target. There, the trimer is the most dominant species which again can be explained by thermodynamics. In general, the magic numbers reported for carbon e.g. by Rohlfing et al.[59] where reproduced.

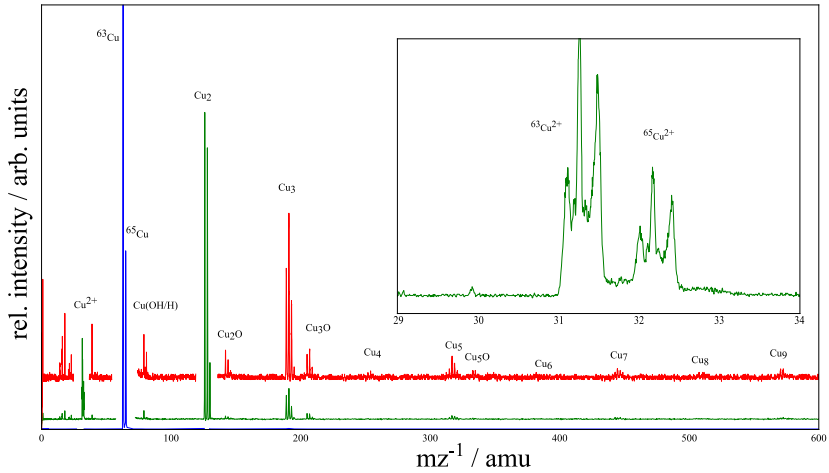

Figure 11: Copper mass spectra using multiphoton fs-ionization using the focused beam of a Ti:sapphire laser (800nm). To increase the visibility of the weak features, three different magnifications were used. The insert shows a zoomed version of the monomer's dication. The peaks clearly suggest, that fragmentation of a larger species took place when using approx. 10^{13} W/cm^2 of power. Attenuating the fs pulses removed this feature.

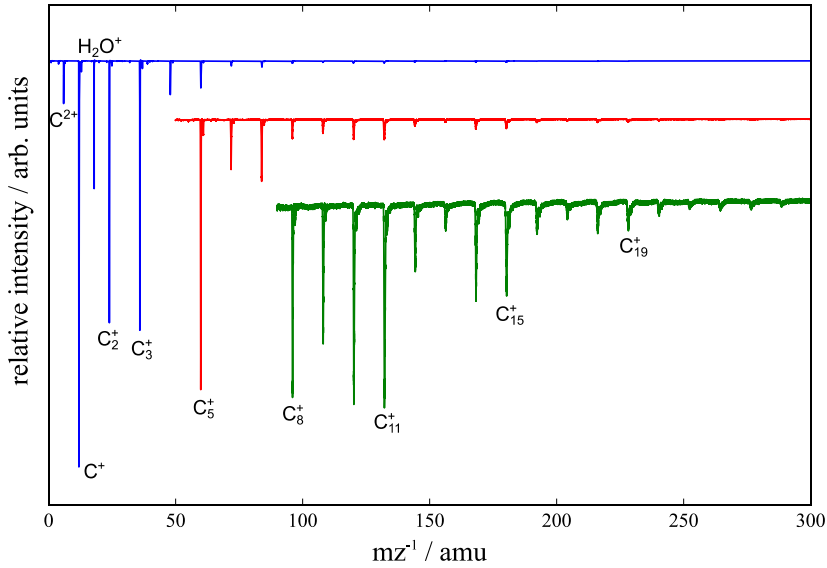

Figure 12: Carbon mass spectra using multiphoton fs-ionization using the focused beam of a Ti:sapphire laser (800nm). The red trace is a magnified version of the blue one, the green one another zoom.

Being able to do ablation on well-defined surface elements, we also experimented with coated targets. On a copper target with an electrochemically deposited layer of chromium, we not only acquired proof of principle spectra for the chromium dimer, but, when using a defined overlap of fresh and used surface, we could also observe species grown from a mixture of the coating and bulk materials. Figure 13 shows such a spectrum. The high amount of oxygen present is probably a side effect of the coating process and can be probably avoided by using e.g. sputtering instead of electrochemical deposition.

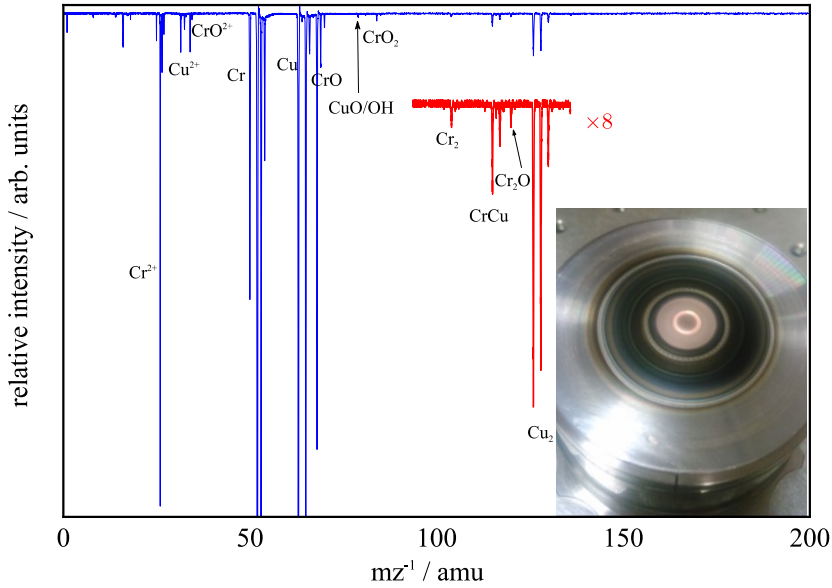

Figure 13: Mass spectrum obtained using the chromium coated copper target, after finding conditions in which both bulk and coating were ablated at the same time. The target is shown as an insert. The chromium in the center region was not ablated but over-coated with copper vaporized in the deep ring surrounding it.

3.5 The second version of the cluster source

When the spring-loading of the target assembly was introduced in the course of the commissioning phase, preload and mounting was performed by the same screws. This complicated the exchange of the target, but also limited reproducibility of the preload. Therefore, the moving parts were redesigned to realize a lockable bayonet catch to mount the sample holder. To increase the flexibility on the input side of the ablation laser, targeting further modifications of the growth channel geometries, the rotational motor was already moved to the back side of the base plate. In addition, a support was added to both sides of the drive pinion of the belt, to reduce sheer forces acting on the gear at the end of the motor. As the base plate was quite scratched after several accidents, which lead to a decreased gas tightness,

and to decreased service life of the PEEK seal, the backside of the base plate was milled to accept 0.5mm thick foils of stainless steel as a wear part. Figure 14 shows a semi-transparent schematic of the changed components, where the replaced parts were colored.

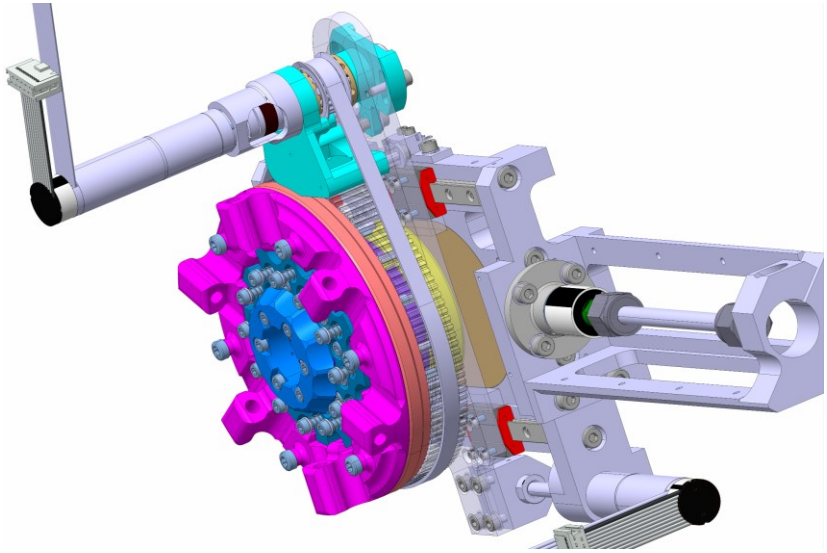

Figure 14: Schematic of the modified cluster source as it was used at the end of this work.

3.6 Conclusion

Over the course of this work, the cluster source achieved the number density requirements to do non-linear spectroscopy on the copper dimer. Next to the pulse to pulse stability, also the reliability could be improved to finally reach up to 150 hours of operation without the need of breaking the vacuum. While this number was achieved on a bulk target, where each surface element was used multiple times, the implementation of a bayonet lock allows to swap prepared target assemblies in a time that is predominant defined by the venting and pumping speed of the vacuum chamber. At this

stage, the source is not yet capable of producing large clusters, but the reasons for this will be addressed in future revisions.

3.7 Outlook

Already during the preparation of this thesis, initial tests with an experimental pulsed valve were undertaken. This valve was provided on loan by the Stienkemeier group at the University of Freiburg (Germany). It is constructed similar to the CRUCS valve described in Ref. [60]. Its design is closely related to the commercially available Even-Lavie valve[61]. It was further modified to achieve the high peak flow rate needed by this cluster source. Preliminary results, using the resulting short, but very intense gas pulses, show a significant increase in accessible cluster sizes also for copper and a decrease in overall gas load. The latter is due to the much shorter opening time, compared to the general valve.

Scheduled engineering work is dedicated to replace the static base plate by a frame carrying modular cluster aggregation modules. Together with a reworked version of the electromechanical components, this will allow a fast exchange of “source heads”. These heads will contain both channels for gas supply, cluster aggregation, ablation laser access. These heads, whose flexible design is further enhanced by the availability to 3D print them from stainless steel or titanium, can also include (liquid nitrogen) cooling but also optical elements that form a physical seal of the ablation laser entrance against vacuum. In sum, this enables full adjustability of pressure, temperature, and aggregation time. Together with the metal concentration, which is adjusted by the ablation laser focus and power, this gives control over all parameters needed to produce clusters of arbitrary sizes. Finally, reaction chambers for providing additional reactants to the clusters during or after creation can be included directly into the source head. As free laser beams require safety requirements that are hard to meet at user facilities, the coupling of the ablation laser into an optical fiber with 1500 µm core

diameter is tested. As this further allows to combine mounting and supply of the source on a single flange, it becomes a versatile platform to be used at synchrotrons and free electron lasers. Reducing the laser power, also fragmentation-free laser-desorption of biomolecules (coated onto a target disk) would be an alternative applications going beyond production of metal clusters.

4 The low-lying electronic states of Cu_2

Declaration: this chapter reproduces the main results from [B. Visser, M. Beck, P. Bornhauser, G. Knopp, J. A. van Bokhoven, R. Marquardt, C. Gourlaouen, P. P. Radi, "Identification of a new low energy 1u state in dicopper with resonant four-wave mixing", *J. Chem. Phys.*, 2017, **147**, 214308], with the permission of AIP Publishing. The experimental work was equally distributed among Bradley Visser and the author. The experimental part was initially written by Bradley Visser and the theoretical part by Roberto Marquardt.

4.1 Introduction

Once the cluster source (see Chapter 3) was producing the copper dimer in sufficient number density for application of TC-RFWM spectroscopy, the sensitivity of this method should be utilized to explore transitions into *gerade* states applying TC-RFWM in an UNFOLDED scheme (see Chapter 2.3.1.1). To do so, we kept one laser in resonance with band head of the (0,0) B-X band and scanned the second dye laser, which was set-up for prove of principle measurements accessing the A-X band in an UP scheme, towards longer wavelengths. As the low-lying states of copper were supposed to be well known, any detected band found should have been a two-photon excitation into a high-lying *gerade* state. However, when we indeed found a band about 300 cm^{-1} below the A-X system, the rotational progression of lines was incompatible with an UNFOLDED scheme, where the B state would have been the common state enabling the four-wave mixing process. Therefore, this band had to originate from an additional low-lying state, even so all states accessible with a one-photon process from the ground state were already known. As this new band was unambiguously assigned to a transition originating in the electronic ground state of the copper dimer, this fundamentally challenged the existing knowledge on the copper dimer and finally gave rise to the findings described in this chapter.

4.2 Experimental results

The production of copper dimers with the laser vaporization source was first optimized using time of flight mass spectrometry combined with femtosecond ionization. One-color (degenerate, DFWM) and TC-RFWM spectroscopy was subsequently performed on the known transitions of Cu_2 in the visible region, proving the efficacy of the non-linear spectroscopic methods.[58]

Transitions to the A' state were too weak to be observed with DFWM at the Cu_2 density present in the expansion. The low-resolution scan of the (0,0) A' – X $^1\Sigma_g^+$ band shown in Figure 15 was performed using the UP (or hole-burning) scheme of TC-RFWM (inset of Figure 15) with the probe transition fixed close to the (0,0) B $^1\Sigma_u^+$ (0_u^+) – X $^1\Sigma_g^+$ R-branch band head. The large strength of the B $^1\Sigma_u^+$ (0_u^+) – X $^1\Sigma_g^+$ transition lends intensity to the four-wave mixing signal and enables the measurement of the A' – X $^1\Sigma_g^+$ transition. Double-resonance selection rules impose that only transitions are observed that originate from labeled ground state rotational levels in the R-branch. The probe laser power was increased in order to saturate the transition and label as many rotational states as possible (J = 6–13). The adverse effects of such a saturation can be observed in the intensity distribution of rotational branches which show a dip[62] at J = 12. This rotational level is affected predominantly since the probe laser is centered at the R(12) line of the (0,0) B $^1\Sigma_u^+$ (0_u^+) – X $^1\Sigma_g^+$ band.

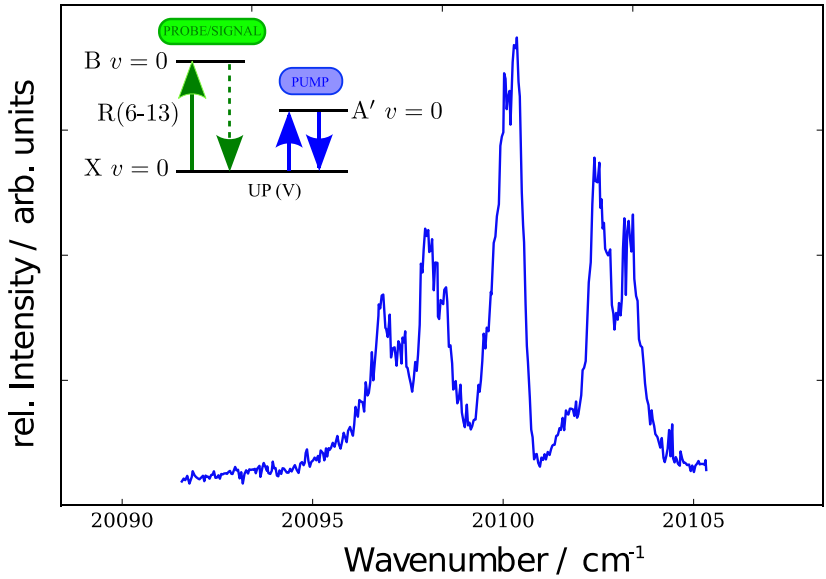

Figure 15: TC-RFWM of Cu_2. The double-resonance spectrum is observed by tuning the probe laser close to the band head in the R-branch of the (0,0) B $^1\Sigma_u^+$ (0_u^+) – X $^1\Sigma_g^+$ band at 21 748.28 cm^{-1}. Only lines originating from J''= 9-13 are observed by scanning the pump lasers in the wavenumber region of the A' – X $^1\Sigma_g^+$ transitions. A dip in the branches occurs at J = 12 due to a strong saturation of the R(12) line by the probe laser.

To ensure that the A' state was one-photon accessible from the ground state (UP scheme), the scan was also performed with the probe laser fixed to rotational transitions in the (1,0) B $^1\Sigma_u^+$ (0_u^+) – X $^1\Sigma_g^+$ and (0,0) C $^1\Pi_u$ (1_u^+) – X $^1\Sigma_g^+$ bands. Rotational level selective scans at a much higher effective resolution were measured for the (0,0) and (1,0) bands of the A' – X $^1\Sigma_g^+$ electronic transition by fixing the probe laser to isolated transitions in the (1,0) B $^1\Sigma_u^+$ (0_u^+) – X $^1\Sigma_g^+$ band. Transitions to v' = 2 and higher vibrational levels proved too weak to be observed.

In Figure 16(a), a typical DFWM scan of the (1,0) B $^1\Sigma_u^+$ (0_u^+) – X $^1\Sigma_g^+$ band is plotted against a simulation of the transition using molecular constants determined in this work for A' and ground state values from Ram *et al.*[17]

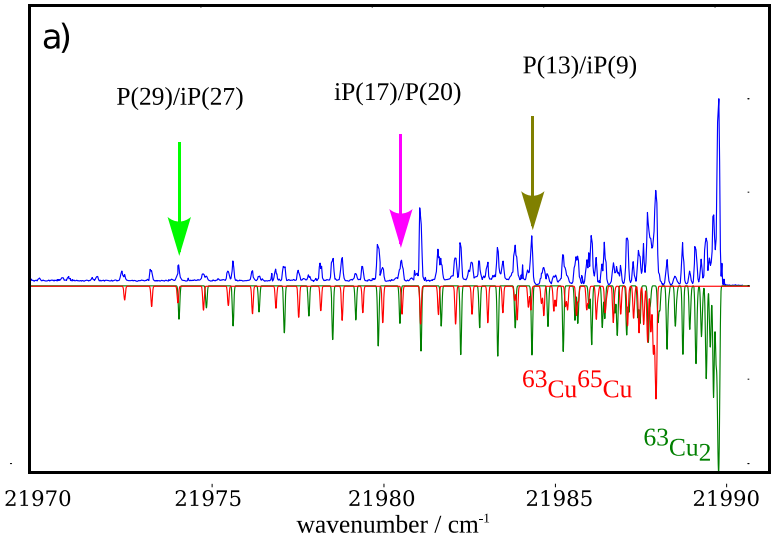
a)
P(29)/iP(27)
iP(17)/P(20)
P(13)/iP(9)
63Cu65Cu
63Cu2
21970
21975
21980
21985
21990
wavenumber / cm-1

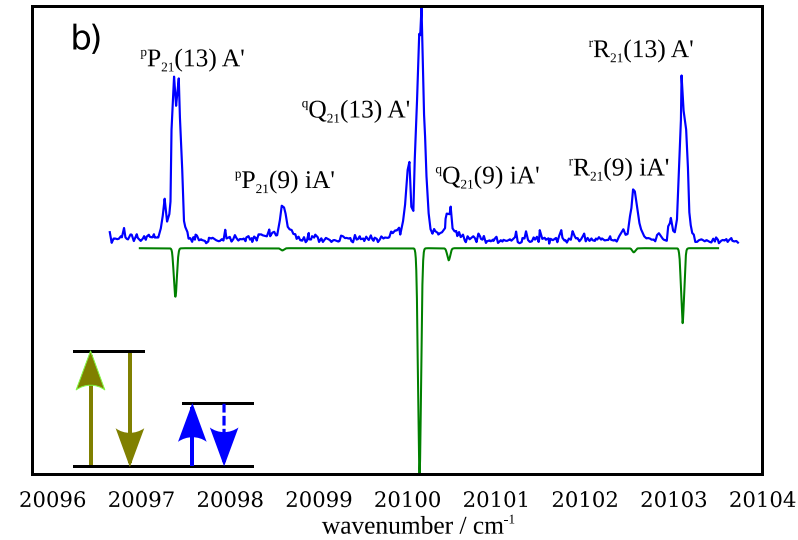
b)
pP21(13) A'
qQ21(13) A'
rR21(13) A'
pP21(9) iA'
qQ21(9) iA'
rR21(9) iA'
20096
20097
20098
20099
20100
20101
20102
20103
20104
wavenumber / cm-1

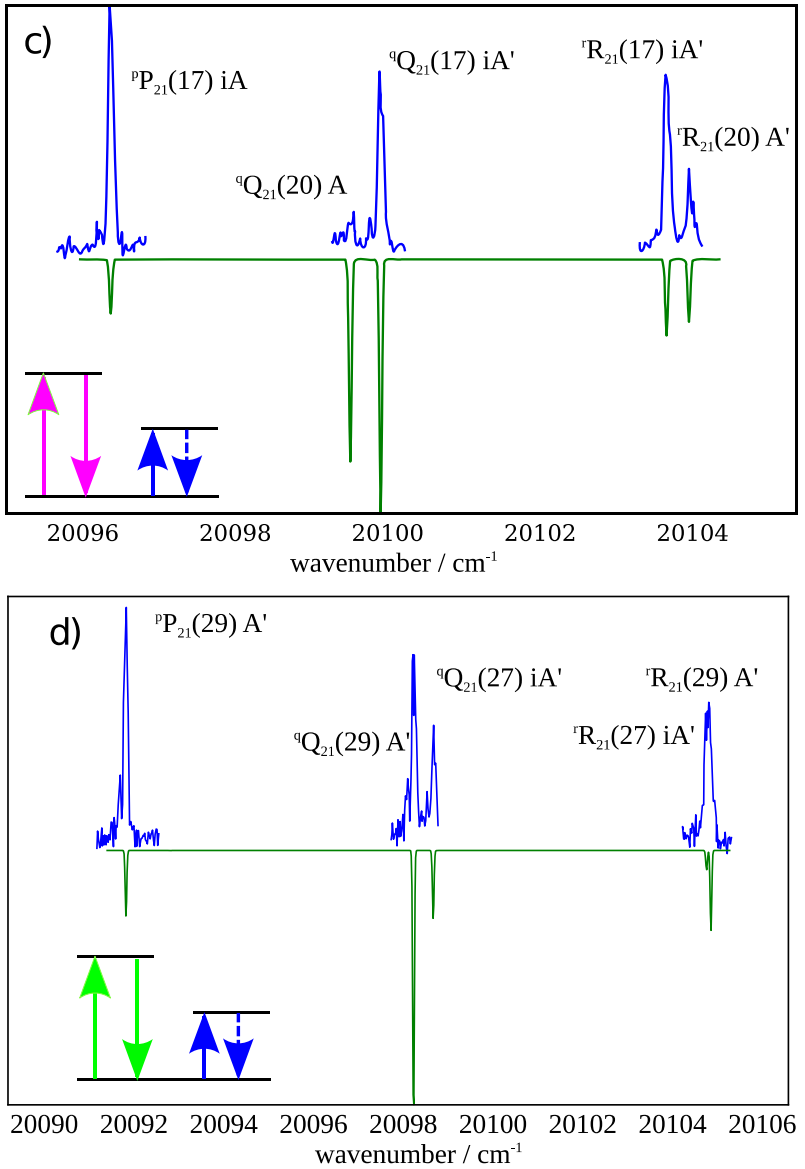

Figure 16: Four-wave mixing spectra of Cu_2. (a) depicts the DFWM spectrum of the (1,0) B $^1\Sigma_u^+$ (0_u^+) – X $^1\Sigma_g^+$ band. Inverted, simulated spectra for $^{63}Cu_2$ and $^{63}Cu^{65}Cu$ are shown in green and red, respectively. Simplified TC-RFWM spectra were obtained by intermediate labeling of specific rotational transitions (b)–(d). See the text for details.

The simulation is split into two components representing the contributions from the $^{63}Cu_2$ (green) and $^{63}Cu^{65}Cu$ (red) isotopologues to aid the dissemination of the experimental spectrum. Many transitions overlap with other various transitions in one or the other isotopologue.

To ensure spectral selectivity of the TC-RFWM scans of A', the more widely spaced P-branch lines in the (1,0) B $^1\Sigma_u^+$ (0_u^+) – X $^1\Sigma_g^+$ spectrum were used to label the individual rotational states [Figure 16(a)]. Nevertheless, owing to the dense spectrum, often two rotational states (one in each isotopologue) were labeled simultaneously. The pump transition for each example in Figure 16(b) – Figure 16(d) is marked with an arrow in Figure 16(a), where P(*J''*) denotes a transition within the $^{63}Cu_2$ isotopologue and iP(*J''*) a transition within the $^{63}Cu^{65}Cu$ isotopologue. The low-abundant isotopologue $^{65}Cu_2$ was not observed in this study due to the inherent squared dependence of the signal on the number density for four-wave mixing. Figure 16(b) is obtained by tuning the probe laser to P(13) in the (1,0) B $^1\Sigma_u^+$ (0_u^+) – X $^1\Sigma_g^+$ band of the $^{63}Cu_2$ isotopologue at 21 984.66 cm^{-1}. This rotational transition coincides with P(9) of the 65Cu63Cu isotopologue and is denoted iP(9) in Figure 16(a). In the TC-RFWM spectrum, $^pP_{21}(13)$, $^qQ_{21}(13)$, and $^rR_{21}(13)$ lines of the A' – X $^1\Sigma_g^+$ transition are observed. Three more transitions are observed owing to the overlapping iP(9) line in the probe laser: $^pP_{21}(9)$, $^qQ_{21}(9)$, and $^rR_{21}(9)$. The rotational transitions define the term energies for *J* = 12, 13, and 14 for A' of the $^{63}Cu_2$ isotopologue and *J* = 8, 9, and 10 for $^{65}Cu^{63}Cu$.

In Figures 16(c) and 16(d), additional TC-RFWM scans are shown for intermediate labeling of ground state rotational levels by the overlapping pairs iP(17)/P(20) and P(29)/iP(27) at 21 980.87 and 21 974.33 cm^{-1} in the (1,0) B $^1\Sigma_u^+$ (0_u^+) – X $^1\Sigma_g^+$ band, respectively. Each spectrum shows clearly resolved lines that are easily assigned to transitions within each isotopologue. The spectra show the clear presence of a Q-branch, thus

leading to the assignment of A' to $^1\Sigma_u^+$ in Hund's case (c). The plots shown inverted in this figure are simulations employing the molecular constants determined in this work for A' and the work of Ram *et al.*[17] for the ground state. Accurate simulation of four-wave mixing signal strengths requires careful control of the input laser intensities. For this work, however, no attempt was made to model the spectral intensity distribution in detail because results are obtained from line positions. Line intensities are nonetheless used as a guide for the assignment. The individual TC-RFWM spectra were analyzed and peak positions were determined using the peak finding algorithms in PGOPHER.[33] The spectroscopic constants for A' are presented in Table 4. The RMS values of all the fits are less than the linewidths of the dye lasers. Statistical uncertainties are given in units of the last significant digit. No allowance is given for systematic errors in the calibration. The complete line list is included as Table 11 in chapter 10.3. Considering the T_v values in Table 4, the vibrational term differences $\Delta G_{1/2}$[§§§] $= T_1 - T_0 \approx \omega_e - 2\omega_e x_e \approx \omega_e$, one obtains an estimation for the equilibrium constants ω_e and ω'_e for the two isotopologues $^{63}Cu_2$ and $^{63}Cu^{65}Cu$ of 233.0723 cm^{-1} and 231.3057 cm^{-1}, respectively. Similarly, an estimation for B_e (and B'_e) is obtained by $B_e \approx B_0 + \alpha/2$, where $\alpha \approx B_0 - B_1$ which results for the two isotopologues to 0.106130 and 0.104569 cm^{-1}. The corresponding equilibrium distance r_e is 2.246 Å. The usual isotope relationships $\omega'_e/\omega_e = \rho$ and $B'_e/B_e = \rho^2$ can be tested for consistency, where $\rho = \sqrt{\mu/\mu'}$ and μ and μ' are the reduced masses of the isotopologues. The experimental values $\rho = 0.9924$ and $\rho^2 = 0.9853$ are in good agreement with the theoretical mass relations, i.e., 0.9923 and 0.9845, respectively.

[§§§] The symbol $\Delta G_{1/2}$ has been introduced by Herzberg[3] and since then used by many authors. However, the recommended symbol[63] for a vibrational term difference is $\Delta G(v) = G(v+1) - G(v) = T_{v+1} - T_v$, where electronic terms belong to the same manifold.

Table 4: Optimized molecular constants for the A' state. All values are given in cm^{-1}. *T* is relative to the X, *v* = 0 state. Uncertainties are one standard deviation.

Parameter	$^{63}Cu_2$, *v*=0	$^{63}Cu_2$, *v*=1	$^{63}Cu^{65}Cu$, *v*=0	$^{63}Cu^{65}Cu$, *v*=1
T_v	20100.4090(16)	20333.4813(30)	20100.4911(14)	20331.7968(27)
B_v	0.1057640(44)	0.105032(14)	0.1041607(45)	0.103345(10)
Observations	50	53	75	38
RMS	0.008	0.011	0.009	0.011

4.3 *Ab initio* results

Figure 17 shows potential energy functions of some spin eigenstates and corresponding spin-orbit states in the ss and sd channel from calculations in the (22,18) RAS at the MRCI+Q level of theory. Only ungerade states that might contribute to observable transitions from the X $^1\Sigma_g^+$ state are shown, and assignments result from the analysis of the data discussed below. The reader is also referred to Table 3 (p. 34) for additional information on the correspondence of states in Hund's cases (a) and (c).

The dissociation energy in the X $^1\Sigma_g^+$ ground state is $D_e \approx 16500$ cm^{-1} (the MRCI raw value without the Davidson correction is 14950 cm^{-1}), which is close to the experimentally estimated value 16530 cm^{-1} (Ref. [13] and references therein). Furthermore, the minimum of the potential energy function is between 220 and 225 pm, which also fits well the value estimated experimentally (222 pm [17]).

The two excited $^1\Sigma_u^+$ levels show a clear avoided crossing between 300 and 350 pm, indicating a change in character. Inspection of the transition dipole moment indicates that for distances below 350 pm the lower of the two $^1\Sigma_u^+$ levels has a strong ion-pair character, indicative of charge transfer, while the upper level has not. This characters are exchanged beyond that distance.

Asymptotically, spin-orbit states split by about 2040 cm^{-1} (2043 cm^{-1} from experiment[64](p. 171)), and terms are as expected: the first two 0_u^+ levels in the sd separated atoms limit and the first 0_u^+ level correlate with the lower 5/2 D-sublevel, while the last two 1_u levels and the second 0_u^+ level correlate with the higher 3/2 D-sublevel. The calculated $D_{5/2} \leftarrow S_{1/2}$ excitation energy is 12334 *hc* cm^{-1}, and hence about 1000 *hc* cm^{-1} larger than the experimental energy difference[64].

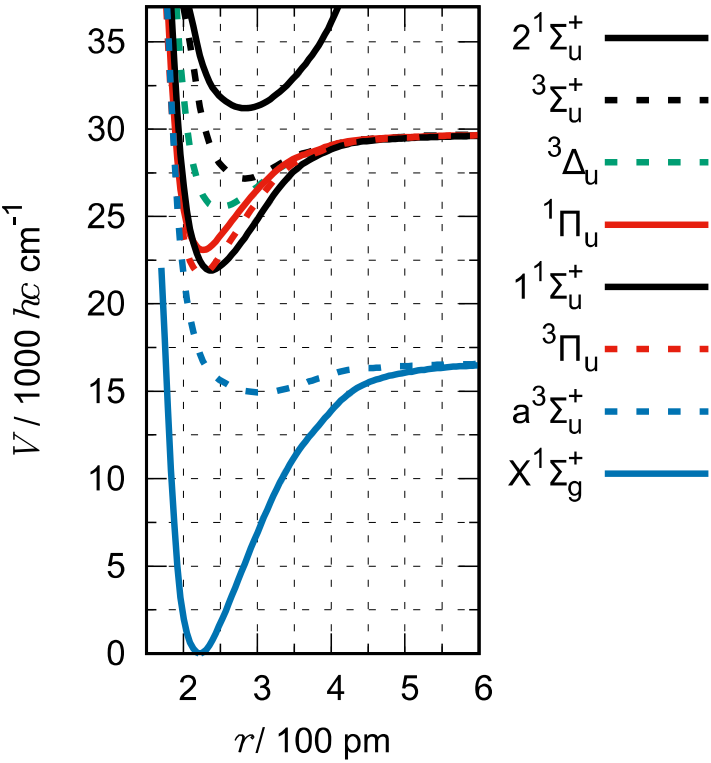

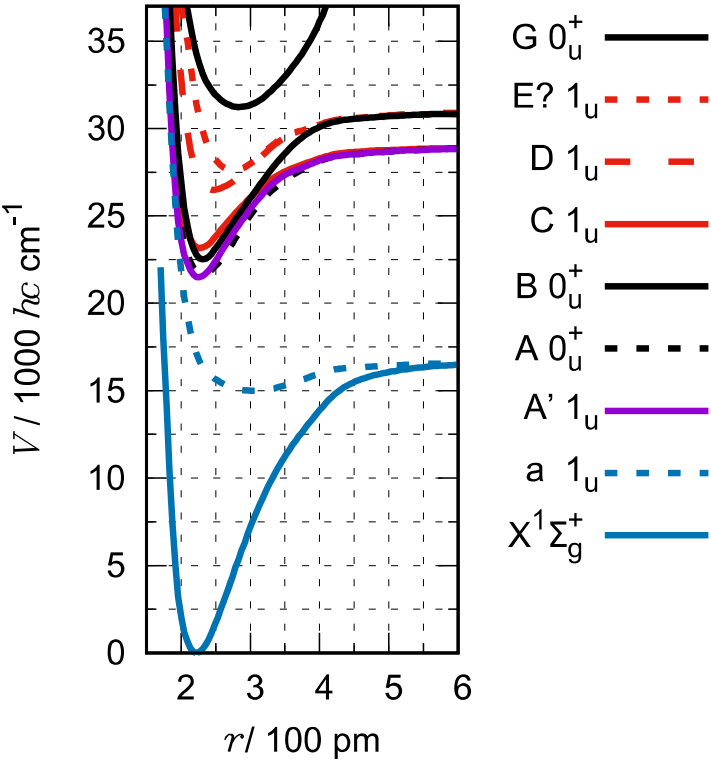

Figure 17: Adiabatic potential functions for the ground state and some ungerade excited states in Cu_2 from MRCI+Q calculations with the AVQZ-DK basis. The relaxed Davidson correction is calculated with respect to rotated reference functions for all levels. Spin eigenstates are shown on the first page, spin-orbit states on the second page. The zero reference energy is the energy of the X $^1\Sigma_g^+$ state, -3307.4167 E_h, at r ≈ 222 pm, where $E_h \approx 4.36 \times 10^{-18}$ J is the hartree. The legend gives the states in the order of appearance from bottom to top at this equilibrium distance. See also text for further explanations and a discussion of assignments.

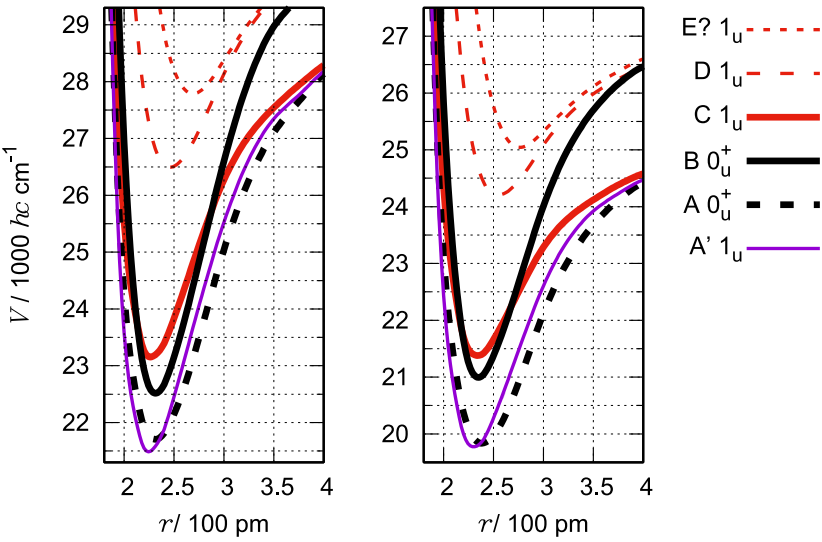

Figure 18: Spin-orbit states. Left hand side: MRCI+Q results $E_{\mathrm{MRCI+Q}}^{(\mathrm{SO})}$ following Eq. 1 (p. 33) (detail of Figure 17). Right hand side: raw MRCI results $E_{\mathrm{MRCI}}^{(\mathrm{SO})}$ without the Davidson-correction. See also the caption of Figure 17 and the discussion of the assignment in the text.

Levels 1 0_u^+ and 2 0_u^+ result from a repulsion of two 0_u^+ levels in the $^3\Pi_u$ and the $^1\Sigma_u^+$ manifolds as a consequence of the spin-orbit coupling. Similarly, the four levels 1 1_u to 4 1_u levels result from the spin-orbit interaction of four 1_u levels in the $^3\Pi_u$, $^1\Pi_u$, $^3\Delta_u$, and the second $^3\Sigma_u^+$ manifolds. While the position of the 2 1_u level is hardly shifted from that of the corresponding $^1\Pi_u$ level, that of the 1 1_u level is pushed by about 300 cm^{-1} below the $^3\Pi_u$ level. The a 1_u level, which relates to the first $^3\Sigma_u^+$ level, is hardly affected by the spin-orbit calculation and essentially coincides with the $^3\Sigma_u^+$ level. The same holds for level 3 0_u^+, which essentially coincides with the higher $^1\Sigma_u^+$ level shown in Figure 17 above.

The Davidson corrected MRCI energies are about 1000 to 1500 *hc* cm^{-1} higher than the raw MRCI values in which the Davidson correction is not included. As will be discussed below, the raw MRCI results are in somewhat

better agreement with the experimental transition energies between electronic levels. This is a rather lucky good agreement that could be related to error cancellations. We shall consider the Davidson corrected results to be more reliable in reference to the whole set of experimental data, despite the larger differences from experimental electronic term values. It is possible that calculations in a larger CAS space would capture electronic correlation better and hence reduce this discrepancy. However, such calculations are outside the scope of the present work. Table 5 summarizes the results.

T_0 values in Table 5 are defined with respect to the v=0 state in the X $^1\Sigma_g^+$ manifold. Theoretical values were calculated from a Chebychev DVR (discrete variable representation, see refs.[65,66]) on a grid of 401 points between 170 and 400 pm, which ensures convergence. A cubic spline interpolation of 13 points calculated *ab initio* was performed to evaluate the potential energy functions on this grid. The 63-copper mass 62.9296 u was used. While the calculated term values including the cluster correction exceed the experimental ones by about 800 to 1500 cm^{-1}, the uncorrected results underestimate the five lowest observed bands by 400 to 1300 cm^{-1}. Although the latter are somewhat closer to experimental values, we consider the former to be more reliable for two reasons. First, consider the term differences $T_0(Y)$ - $T_0(1\ 1_u)$ in the manifold of states Y = 1 0_u^+, 2 0_u^+, 2 1_u, 3 1_u, and 3 0_u^+. They are 48, 1234, 1594, 4407, 9329 cm^{-1}, respectively, in the MRCI calculation. In the MRCI+Q calculation, they are 193, 1026, 1652, 4968 and 10026 cm^{-1}. Experimentally, if one accepts the assignment proposed in Table 5, they are 296, 1648, 1744, 5408 and 10578 cm^{-1}, in the respective order, and hence better reproduced by the cluster corrected calculations. Secondly, as indicated in Table 5, calculated vibrational terms differ from measured values by about 10 cm^{-1} for the MRCI+Q potentials, while differences are a factor of 3 larger for the MRCI results.

Table 5: Experimentally determined electronic and vibrational term values and rotational constants B_0 (in cm^{-1}), equilibrium distances r_e or r_0 (in pm), calculated cross sections $G_{v'0}$ (in pm^2), and fluorescence lifetimes $\tau_{v'=0}$ (in µs) for some low lying excited states of Cu_2 in comparison with theoretical values from the present work.

Experiment						Theory (this work)									
						MRCI		MRCI+Q							
T_0[a]	$\Delta G_{1/2}$[a]	r_e	τ_0	Properties	Reference	T_0[a]	$\Delta G_{1/2}$[a]	T_0[a]	$\Delta G_{1/2}$[a]	B_0	r_0	$G_{v'0}$	(v')[b]	τ_0	Label	Assignment
20 100	233	2.246		Q band, middle	This work	19 750	190	21 480	223	0.105	2.26	4.1	(0)	3.0	A′	$1\,1_u$
20 396	192	2.283	0.115	No Q band, strong	1	19 798	158	21 673	183	0.100	2.32	100.0	(0)	0.04	A	$1\,0_u^+$
21 748	241	2.328	0.04	No Q band, strong	1	20 984	213	22 506	230	0.100	2.32	190.0	(1)	0.03	B	$2\,0_u^+$
21 844	218	2.264	0.8	Q band, strong	1	21 344	167	23 132	201	0.103	2.28	44.0	(0)	0.2	C	$2\,1_u$
25 508	160	2.380	6.5	Weak	1	24 157	127	26 448	154	0.088	2.47	0.15	(6)	4	D	$3\,1_u$
27 136	223			Weak	13	24 988	124	27 736	140	0.074	2.70	≤0.001	(c)[c]		E	$4\,1_u$
28 541	246			Weak	1										F	?
30 678	116	2.730		Middle	1	29 079	124	31 506	117	0.073	2.71	9.2	(26)	0.008	G	$3\,0_u^+$

[a] T_0 defined with respect to the $v = 0$ state in the $X\,^1\Sigma_g^+$ manifold. $\Delta G_{1/2} = T_1 - T_0$ in the corresponding electronic manifold.

[b] $G_{v'0}$ is the maximal absorption or emission cross section between state v' in the excited electronic level and state v'' in the electronic ground level. The value of v' is given in parentheses.

[c] The maximal absorption or emission cross section lies in the continuum. The value given refers to the cross section of the highest bound state $v' \sim 28$.

Rotational constants B_0, averaged positions r_0 and cross sections are calculated as expectation values of the corresponding operators using the vibrational wave functions determined from the MRCI+Q potentials. Cross sections are defined by

$$G_{v',v''} = \frac{2\pi^2}{3hc\epsilon_0} M^2_{v',v''}, \quad (2)$$

where h is the Planck constant, c the speed of light in vacuum, ε_0 the electric constant and $M^2_{v',v''} = \sum_\alpha \left|\left\langle \psi_{v'} \middle| \mu_e^{(\alpha)} \middle| \psi_{v''} \right\rangle\right|^2$ are transition dipole moments using full transition electric dipole moments functions $\mu_e^{(\alpha)}$ (α = x,y,z) between the electronic states involved as obtained from the raw MRCI calculations. Only the maximal values for absorption transitions $v' \leftarrow v'' = 0$ are reported in Table 5, where v' is the vibrational quantum number in the electronically excited state and v'' is the vibrational quantum number in the electronic ground level. The corresponding v' of the maximum is also given in the table. The cross sections mirror the weak and strong electronic transitions well.

Using the calculated cross sections, we also report fluorescence lifetimes $\tau_{v'} = 1/A_{v'}$ for several states, where $A_{v'} = \sum_{v''} A_{v',v''}$ and $A_{v',v''} = 8\pi c|\tilde{\nu}_{v'} - \tilde{\nu}_{v''}|^3 G_{v',v''}$ is the Einstein A-coefficient involving states v' and v'' in the corresponding electronic manifolds.

The assignments proposed in Figures 17 and 18, and in Table 5 will be discussed in the following.

4.4 Discussion

The spectra shown in Figure 16 demonstrate the strengths of using TC-RFWM spectroscopy. For a TC-RFWM signal to be generated, two resonant transitions must share a common intermediate state. Thus, with the use of narrow band nanosecond lasers, single rotational levels can be selected (or

labeled) and only transitions from the selected rovibronic level are observed. This selectivity simplifies the assignment of spectra considerably and leads to an *effective* resolution that is much higher than what is achievable with standard spectroscopic techniques. As such, the position of individual lines within band heads can be measured in isolation. TC-RFWM is particularly effective for deciphering overlapping bands and detecting small shifts and lines caused by perturbations.

The gas-phase measurements of the electronic structure of Cu_2 were reviewed by Morse in 1993.[1] Since then several new states were observed in the UV in absorption[18] and improved spectroscopic constants for the D state were reported in a study of Cu_2 in supercooled helium.[19] Despite the considerable amount of attention that the copper dimer has received, very few of the excited electronic states have been rotationally resolved and assigned spectroscopic constants.

Aside from the ground state and the lowest triplet state that correlate to $3d^{10}4s^1\ ^2S$ ground state atoms, the low energy electronic structure of Cu_2 is dominated by states that correspond to the $^2S + {}^2D_{3/2,5/2}$ ($3d^9\ 4s^2$) pair of atomic limits. The necessity of describing these 'd-hole' excited states in Hund's case (c) coupling was first proposed by McCaffrey *et al.* [9] to explain the presence of two $^1\Sigma_u^+$ states in the visible wavelength range. However, the second $^1\Sigma_u^+$ state could also arise from an ion-pair state and the influence of ion-pair states in this energy region has been inferred from the very short lifetimes of the A (115 ns) and B (40 ns) states.[1] The discovery of the A' state confirms Hund's case (c) coupling is required to account for the number of low energy electronic states observed (*vide infra*).

For states in the 20000 - 22000 cm^{-1} energy range, the only reasonable separated atom limits are $^2S + {}^2D_{5/2}$ and $^2S + {}^2D_{3/2}$. The following set of dd separated atom limits consist of a pair of d-hole atoms and have a net bond order of zero if the 3d electrons are considered to be non-bonding. The next

highest separated atom limit is $^2S + ^2P^0$ at 30535 cm^{-1} above the ground state limit and would require the states to be bound with more than 25000 cm^{-1}, which is considerably more than the ground state bonding energy of 16530 cm^{-1}.[13]

The states that arise from the $^2S + ^2D$ separated atom limits in both Hund's case (a) and (c) are covered extensively in the work of Page and Gudeman.[11] Under Hund's case (a) there are only two states that can spectroscopically couple with the ground state via the electric dipole: $^1\Sigma_u^+$ and $^1\Pi_u$. The C state at 21843.9 cm^{-1} has already been identified as $^1\Pi_u$ in Hund's case (a) and thus the A' state cannot be accounted for in this coupling scheme. The A and B $^1\Sigma_u^+$ states had also presented a problem, but the presence of a second $^1\Sigma_u^+$ in this energy range could be attributed to the presence of ion-pair states.[13] The same argument cannot be used to explain the presence of an additional $^1\Pi_u$ state in this energy range as the lowest $^1\Pi_u$ ion-pair states are expected to lie at least 1 eV above the lowest $^1\Sigma_u^+$ ion-pair state.[13]

In Hund's case (c) one 0_u^+ and two 1_u states arise from each of the $^2S + ^2D_{5/2}$ and $^2S + ^2D_{3/2}$ separated atom limits.[11] This easily accounts for the A', A, B and C states and indicates that two further 1_u states should be spectroscopically accessible from the ground state. One of these states may be the D state, which has so far only been observed in matrices and ultracold helium.[12,19] The other state could be state E,[13] although the observation of that state might still be questionable[1]. Also the assignments of the E and F bands are uncertain. These states could also arise from the dd limit of separated atoms, but the calculation of states belonging to that limit are outside the scope of the present work. Should this hypothesis be true, the 4 1_u state would then be a state that has not yet been measured. Apart from the E and F states, the theoretical results in Figures 17 and 18, as well as in Table 5 strongly support these assignments from the overall inspection of relative energies and other calculated properties of the states. From these results, band G can

definitely be assigned to the third 0_u^+ state (or $^1\Sigma_u^+$ in Hund's case (a) notation) which would correspond asymptotically to the B_{1u} charge transfer state in the ss limit of separated ions of Table 2 (p. 31), confirming thus the conjectures made by Rohlfing and Valentini[15].

The calculated fluorescence lifetimes reported in Table 5 underestimate the observed values for the A and C states by a factor of four, but fit rather nicely the values for states B and D. The accuracy of these calculated properties is unknown. Their variance can be rather large even with small changes of the shape of the potential and dipole moment functions. We therefore consider only the qualitative aspect of the calculated cross sections and fluorescence lifetimes in Table 5, which seem nevertheless to contribute coherently to the proposed assignment. As a matter of fact, the intensity ratio of roughly 20:10:1 observed by Bondybey *et al.* for the *v'*=0, 1, and 2 peaks, respectively, in the laser excitation spectrum of state A and depicted in figure 1 of their paper[12] is rather well reproduced by values calculated during this work (15:10:2).

The *ab initio* study of the copper dimer in this work is the first to consider the low energy states in Hund's case (c) terms. The energy ordering of 0_u^+ and 1_u terms fits exactly to what has been observed experimentally. The $1\ 0_u^+$, $2\ 0_u^+$, $1\ 1_u$ and $2\ 1_u$ terms can easily be assigned to the A, B, A' and C states, respectively. Doverstal *et al.*[67] assigned the C (1_u) state as correlating with the lower of the two $^2S + {}^2D$ separated atom limits based upon the measured dissociation energy. Thus, as to not violate non-crossing rules A' is also assigned to correlate with the lower of the two separated atom limits.

The study of Witko and Beckmann[68] is one of the few previous *ab initio* investigations of the excited states of the copper dimer. The case (a) terms that lead to spectroscopically accessible case (c) states are $^1\Sigma_u^+$ (0_u^+), $^1\Pi_u$ (1_u), $^3\Sigma_u^+$ (1_u), $^3\Pi_u$ (0_u^+ and 1_u) and $^3\Delta_u$ (1_u). According to Witko and Beckmann these terms are ordered as $^3\Sigma_u^+ < {}^3\Pi_u < {}^1\Sigma_u^+ < {}^1\Pi_u < {}^3\Sigma_u^+ < {}^3\Delta_u$. The

case (c) ordering then perfectly matches that of the experimentally determined states in the sd separated atoms limit: A' 1_u < A 0_u^+ < B 0_u^+ < C 1_u. In addition to being coherent with these previous calculations, the theoretical results from the present work give near quantitative agreement with the experimental values. They confirm the importance of spin-orbit couplings, which were omitted in Ref. [68].

Support for the aforementioned assignments can be found in studies of the electronically similar CuAu and Au_2. The work of Bishea *et al.*[69] on CuAu showed that despite the small spatial extent of the 3d Cu orbitals, they are split into bonding and antibonding orbitals. By following the example of Bishea and Morse for the case of Au_2,[23] and applying it to Cu_2, the energy ordering of the 3d orbitals is $d\sigma_g < d\pi_u < d\delta_g < d\delta_u < d\pi_g < d\sigma_u$, which leads to an ordering of the $^2S + {}^2D$ excited state terms for each multiplicity of $\Sigma_g^+ < \Pi_u < \Delta_g < \Delta_u < \Pi_g < \Sigma_u^+$. Due to exchange effects the triplet states are expected to lie below the respective singlet states of the same term. This analytical ordering of states is found to mostly hold for Au_2 with only a very major deviation found in the case of the $^1\Sigma_u^+$ term, which, instead of laying highest in energy, has the largest binding energy for this set of states,[23,70] very likely due to strong mixing with ion-pair states.

The *ab initio* calculations of Das and Balasubramanian on Au_2[70] provide significant insight into the excited electronic states of this species and can be extended to Cu_2. The A 0_u^+ state of Au_2, for example, was found to have 49% $^3\Pi_u$ ($s\sigma_u \leftarrow d\pi_g$), 21 $^1\Sigma_u^+$ ($s\sigma_u \leftarrow d\sigma_g$) and 12% $^1\Sigma_u^+$ ($s\sigma_u \leftarrow s\sigma_g$) character, where $s\sigma_u \leftarrow s\sigma_g$ corresponds to a charge transfer transition to an ion-pair state. The inclusion of 12% ion-pair state character is significant as it leads to the large oscillator strength observed for this transition.[23] The even larger oscillator strength of the B $0_u^+ \leftarrow$ X $^1\Sigma_g^+$ transition is in good agreement with the 49% ion-pair character calculated for this state.[23] The calculations of Das and Balasubramanian also reveal that the lowest two 1_u states have

primarily $^3\Pi_u$ and $^1\Pi_u$ character, respectively. Bishea and Morse[23] assert that these two states correlate with the experimentally measured A' and B' states of Au_2. They also observe that the primary $^1\Pi_u$ and not the $^3\Delta_u$ character of the second lowest 1_u implies that the energetic splitting of the 5d orbitals in Au_2 is larger than the exchange interactions.

When comparing the experimental and theoretical results for the gold and copper dimers many similarities are seen. The absorption cross sections of the A and B states in the copper dimer follow a very similar trend and are much larger than for transitions from the ground state to either of the experimentally observed 1_u states. Again, for Cu_2 the B-X transition is the strongest observed in the low energy regime and suggests that the B 0_u^+ state has significant ion-pair character, which is confirmed by the calculated transition dipole moments in the present work as well as by the *ab initio* calculations of Witko and Beckmann[68], who showed that the (ion pair) ...4sσ_g4sσ_u electronic configuration dominates over $^1\Sigma_u^+$ (sσ_u←dπ_g) for small internuclear distances. The large cross section of the A-X transition also implies that the A 0_u^+ state exhibits fractional ion-pair character.

Finally, a discussion on the inability of previous experimental studies to observe the A' state is merited. The first rotationally resolved study of the A state by Pesic and Weniger[7] noted the presence of Q-branches, which were not observed in subsequent experimental measurements of this state[8,9]. Later, experimentalists assumed that the observation of Q-branches in the spectra of Pesic and Weniger was erroneous born from confirmational bias due to the previous assignment of the B state to $^1\Sigma_u^+$, thus leaving only a single $^1\Pi_u$ state to couple spectroscopically with the ground state. Crucially however, the majority of these studies were performed using laser-induced fluorescence, an emission-based spectroscopic technique, whereas that of Pesic and Weniger is roughly described as a combination of absorption and emission spectroscopies.[7] Given the small separation of the A' and A

vibrationless levels of ≈300 cm^{-1}, the Q-branches recorded by Pesic and Weniger are almost certainly those of the A' state. Indeed the *v*'=1 level of A' is only ≈60 cm^{-1} below the A *v*'=0 level. We surmise that the A' *v*=0 state was also observed in the recent two photon ionisation/hole burning study of Parry *et al.*[20] There, it was assumed to be a hot-band of the A-X system, however no hot-bands are observed for the stronger B-X system. While a measurement of the lifetime of the A' state was not possible in this work, the calculations yield 3 µs. Such a long lifetime is likely inhibiting LIF studies in a molecular beam. For matrix-based LIF studies the A'-X (0,0) emission would have been buried under the much stronger A-X (0,1) and (0,2) signals. It would then only be observed if the excitation laser frequency were tuned exactly to the transition and no fluorescence from the A-X system were present.

4.5 Conclusion

This chapter reported the application of resonant four-wave mixing techniques to the identification of a new low lying 1_u state in the copper dimer. The highly selective nature of TC-RFWM enabled the separation of the spectra into single *J* components. The discovery of a second 1_u state in the low energy regime and the present ab initio calculations prove the assertion of earlier researchers that spin-orbit or *J*–*J* coupling is required to account for the number of observable states from the $^2S + {}^2D$ separated atom limits of Cu_2. This work also solves a more than 40 year old mystery in the initial experimental assignment of the A state.

5 The high-lying electronic states of Cu_2

Declaration: reproduces the main results with permission from [M. Beck, B. Visser, P. Bornhauser, G. Knopp, J. A. van Bokhoven, P. P. Radi, Rovibrational Characterization of High Lying Electronic States of Cu_2 by Double-Resonant Non-Linear Spectroscopy, J. Phys. Chem. A, 2017, 121, 8448-8452. Copyright 2017 American Chemical Society.] (Chapter 5.2) and [M. Beck, P. Bornhauser, B. Visser, G. Knopp, J. A. van Bokhoven, P. P. Radi, Spectroscopic disentanglement of the quantum states of highly excited Cu_2, Nat. Commun., 2019, 10, 3270] (Chapter 5.3 and 5.4). The author wrote the manuscripts based on experimental work contributed by Bradley Visser, Peter P. Radi, and the author.

5.1 Introduction

After the work on the A' state, described in Chapter 4, we decided to revisit the I and the J states, for which little information was given from literature (see Chapter 2.1). Instead, literature reported the failure in even assigning term symbols to these states. While the rotationally resolved spectra of the J-X bands could not be explained, the I state was not even visible in rotationally resolved measurements. Keeping the frequency of one dye laser fixed on the B-X system, second harmonic generation was used to produce the deep UV photons needed to probe the I-X and J-X systems. By applying TC-RFWM spectroscopy, the first rotationally resolved characterization of the I state succeeded and individual rotational levels within the J state could be reported as described in chapter 5.2. However, the J state was found to be to be highly perturbed and only a short series of assumingly unperturbed lines in the $^{63}Cu_2$ isotopologue allowed to report molecular constants. After this, it took additional two years to fully reveal the underlying network of perturbations and all the contributing dark states. These findings are described in Chapter 5.3.

5.2 Early findings in range of the I and J states

Figure 19 shows example TC-RFWM spectra, with the applied double-resonant scheme shown in the inset. The probe wavenumbers in the (1,0) B-X band are calculated based on the molecular constants from Ram *et al.*[17]. Good agreement of these constants with the results obtained by applying our setup has been demonstrated previously.[58] The pump wavenumbers were scanned over the bands of interest. To the left, the ("*x*+1",0) I-X band, and to the right, the neighboring (0,0) J-X one are shown. The vibrational numbering of the I state is not known, therefore the labelling used by Powers *et al.*[14] is adopted, where *x* represents the lowest experimentally known vibrational state. At the top the fluorescence emission of an excitation scan to the first vibrationally excited level of the electronic ground state (X, *v*=1) is presented. The spectrum in the J-X wavenumber range is too dense for assignment, while the I-X band, which is plotted on the same scale, is below the detection limit. The low intensity of this system is in agreement with the failure to observe the I-X electronic system using LIF as reported by Page *et al.*[11]. In contrast, I-X transitions are accessible by TC-RFWM. Selection of individual rotational lines by the probe laser simplifies the corresponding TC-RFWM spectra, which are obtained by scanning the pump wavelength. Only transitions that share the probed rotational level in the ground state produce signal. Therefore, even in the complex spectral regions of the band heads, the absorption spectrum is dramatically simplified and transitions can be assigned unambiguously.

The presence or absence of rotational Q lines in the I-X and J-X electronic systems, respectively, allows immediate assignment of the term symbol based on dipole selection rules. The spectrum of the I-X system corresponds to a $^1\Pi_u$-$^1\Sigma_g^+$ transition and the observed J-X transitions are in accordance with a $^1\Sigma_u^+$-$^1\Sigma_g^+$ transition. Consequently, the term symbol is $^1\Pi_u$ (1_u) for the I state and $^1\Sigma_u^+$ (0_u^+) for the J state. The treatment of Cu_2 in Hund's case (a)

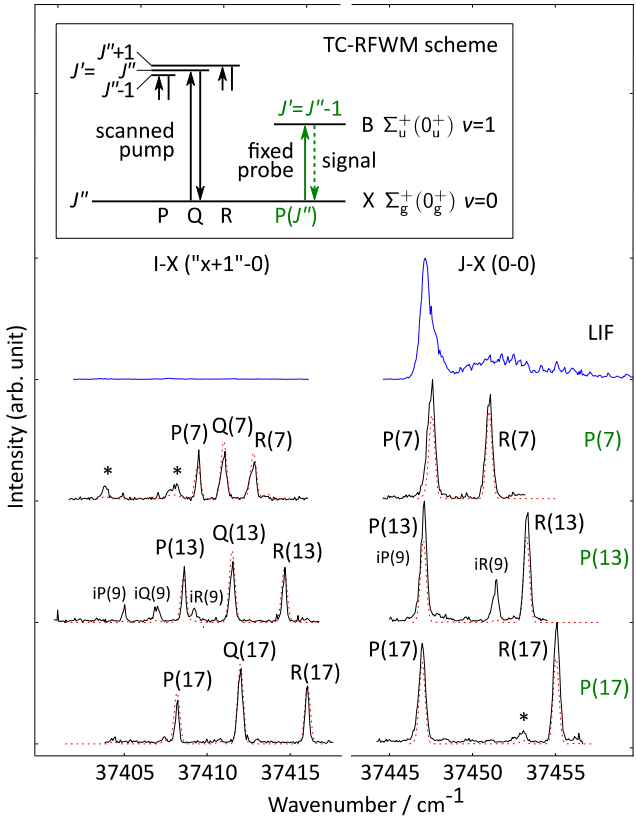

Figure 19: TC-RFWM spectra of the I-X and J-X transitions of $^{63}Cu_2$. The pump wavelength was scanned over the bands of interest while a single rotational line in the B-X (1,0) band (green label P(*J*″)) was probed. The inset illustrates this scheme that reduces the observed spectra to lines originating from a defined rotational level *J*″ of the ground state (X, *v*=0). For comparison (and determination of lifetimes), fluorescence into the X, *v*=1 level was recorded (blue excitation spectrum). Displayed on the same scale, virtually no dispersed fluorescence from the I state is visible. In the TC-RFWM spectra transitions to the I state are also weaker but clearly assignable. Overlaps of the probed B-X lines cause additional features (*) to appear. This is most apparent for the P(13) probe transition where overlap with the iP(9) line of $^{63}Cu^{65}Cu$ adds additional features to the spectrum (iP(9), iQ(9), iR(9). The label "i" is used to distinguish transitions of the isotopologue). The red dotted lines are simulations based on the fitted molecular constants. The presence of Q lines in the I-X transition allows assignment to a $^1\Pi_u\ (1_u)$ term symbol for the I state, and their absence in the J-X transition determines a $^1\Sigma_u^+\ (0_u^+)$ symbol for the J state.

is under discussion, therefore Hund's case (c) labels were added in parentheses.

Tables 12 and 13 (see appendix Chapter 10.4) contain 186 fitted line positions for transitions obtained by TC-RFWM scans. In addition, the corresponding lines in the (1-0) B-X band, which were used for selecting a rotational level *J"* in the ground state, are listed. They cover the J-X (0-0) and (1-0) as well as the I-X ("*x*+1"-0) and ("*x*+2"-0) bands. The line positions were used to fit molecular constants for the individual bands using PGOPHER[33]. The residuals displayed in the third column of the table denote the difference between the observed and the calculated line positions on the basis of the obtained molecular constants. For each band the origin T_v and rotational constant B_v were fitted. Higher order distortions could not be fitted as no data for higher rotational quantum numbers (*J'*) are available.

Table 6 displays the resulting molecular constants and the mean lifetimes, which were obtained by evaluation of the time-dependence of the dispersed LIF signal. In case of the I-X transition 10,000 averages on the band head of the P branch were used to compensate for the low number of events. The excitation pulse duration of approximately 10 ns was too long for a precise measurement of the lifetime, but an upper limit of the mean lifetime could be estimated by fitting to the final decay of the averaged signal. A lower limit of the lifetime can be estimated from the observed line width, which is comparable to those of the long-living J state. The reason for the short lifetime is unclear, but pre-dissociation effects could play a role. To assess the lifetime of the J state, a spectrally separated transition was chosen. The pump wavelength was tuned to the J-X (0,0) R(5) line of $^{63}Cu_2$, but some overlap with R(6) of the heavier isotopologue $^{63}Cu^{65}Cu$ cannot be ruled out. An exponential fit to the averaged LIF signal was used to estimate the mean lifetime.

Table 6: Molecular constants and lifetimes obtained for the I and J states of $^{63}Cu_2$

J state	this work	literature
T_0 [cm^{-1}]	37448.765(12)	37451.1[a]
T_1 [cm^{-1}]	37736.8868(91)	37738.4[a]
B_0 [cm^{-1}]	0.115556(36)	-
B_1 [cm^{-1}]	0.114233(17)	-
lifetime [ns]	65.75(34)	80(10)[b]
I state	this work	Literature
T_{x+1} [cm^{-1}]	37410.7775(60)	37413.3[a]
T_{x+2} [cm^{-1}]	37700.150(10)	37701.3[a]
B_{x+1} [cm^{-1}]	0.112447(28)	-
B_{x+2} [cm^{-1}]	0.112940(53)	-
lifetime τ	10 ps[c] $\leq \tau \leq$ 5 ns[d]	-

[a] Powers *et al.*[14]

[b] Page *et al.*[11]

[c] lower limit estimated by observed line width

[d] upper limit estimated by comparison of dispersed LIF and excitation pulses

The vibrational numbering of the I state is not known, therefore the labelling used by Powers *et al.*[14] is adopted. One standard deviation in units of the last figure was appended in parentheses.

Table 7 contains equilibrium molecular constants for the J state. They are estimated from the obtained constants for v=0 and v=1. The T_e and ω_e values are subject to comparatively large uncertainties, as they inherit the uncertainties of the literature value for $\omega_e x_e$[14]. For the I state, a similar procedure to obtain equilibrium constants is not applicable, because the absolute vibrational quantum numbers of the levels have not been determined.

Table 7: Derived equilibrium constants for the J state of $^{63}Cu_2$

J state	this work	literature
T_e [cm^{-1}]	37437.20(33)[a]	37437.7(1)[b,f]
ω_e [cm^{-1}]	289.40(88)[a]	288.4(21)[c]
B_e [cm^{-1}]	0.116218(54)	0.1165(5)[b]
α_e [cm^{-1}]	0.001323(40)	0.0010(5)[b]
r_e [Å]	2.14708(50)	2.15[b]
$\Delta G_{1/2}$ [cm^{-1}]	288.121(15)[d]	287.3[e]

[a] calculated using $\omega_e x_e$ = 0.64(44) cm^{-1} from Powers *et al.*[14]
[b] Page *et al.*[11]
[c] Powers *et al.*[14]
[d] calculated as T_1-T_0
[e] calculated as T_1-T_0 using the values reported by Powers *et al.*[14]
[f] seems to neglect propagation of uncertainty

As a consequence of the determined $^1\Sigma_u^+$ term symbol of the J state, its full electronic configuration can be established. Following the reasoning of Sappey *et al.*[16], the slightly higher vibrational constant of the J state (289 cm^{-1}) compared to the ground state X (266 cm^{-1})[17] suggests that the $4s\sigma^2$ bond of the ground state remains intact on excitation. As a consequence, the J-X transition involves the promotion of a 3d electron into a slightly bonding or non-bonding orbital. This promotion is likely into a 4p molecular orbital, as the energy involved is comparable to the one for a 4p-3d transition in atomic Cu. Also the diabatic dissociation energy of a Morse potential, which is determined by the molecular constants of the J state, is in the range of the $3d^9 4s4p + 3d^{10}4s$ asymptotes. Experimentally, Sappey *et al.* observed direct photoionization of the J state of Cu_2 to form a $^2\Pi$ state of Cu_2^+ in a facile, one-electron process. This can be attributed to the photoejection of the electron in a 4p molecular orbital, while the 3dπ hole of this ion state is already present in the J state of Cu_2. Therefore, out of the molecular orbitals with predominantly 4p character, only the slightly bonding $4p\sigma_g$ and $4p\pi_u$ orbitals remain as possible targets for the promoted 3dπ electron. Hence, Sappey *et al.* conclude that the Hund's case (a) description of the J state is

either $^1\Pi_u$ from $3d^{18}3d\pi_u4s\sigma_g^2 4p\sigma_g$ or $^1\Sigma_u^+$ from $3d^{18}3d\pi_g4s\sigma_g^2 4p\pi_u$ ($3d^{18}$ denotes nine doubly occupied 3d molecular orbitals). This work's unambiguous assignment of the J state to $^1\Sigma_u^+$ allows determination of the electronic configuration of the J state as $3d^{18}3d\pi_g4s\sigma_g^2 4p\pi_u$.

5.3 Spectroscopic disentanglement of the quantum states of highly excited Cu_2

5.3.1 The main challenges

The J state can be reached directly from the ground state by a strong transition, which was first described by Powers *et al.*[14]. However, in that work the bands recorded were accompanied by unknown features. In 1991, rotationally resolved measurements by Page *et al.* revealed a (0-0) J-X band that could not be assigned, as no set of contrived molecular constants reproduced it.[11] In light of our results, the reason for this becomes clear. Figure 20 shows an accurate simulation of the (0-0) J-X band and a Fortrat diagram, which maps the transitions to the individual rotational quantum number *J'* of the accessed state. There, not only transitions to the bright J state, but also hypothesized transitions into three dark vibronic states are shown. These states exhibit little transition strength from the initial ground state and cannot be accessed directly. However, they gain intensity and experience a line shift where their corresponding branches intersect with the J state. The reason behind this lies in the quantum mechanical mixing of energetically close bright and dark states, given sufficient overlap of their wave functions. Consequently, both states share part of the same character and level repulsion occurs.

5.3 Spectroscopic disentanglement of the quantum states of highly excited Cu_2

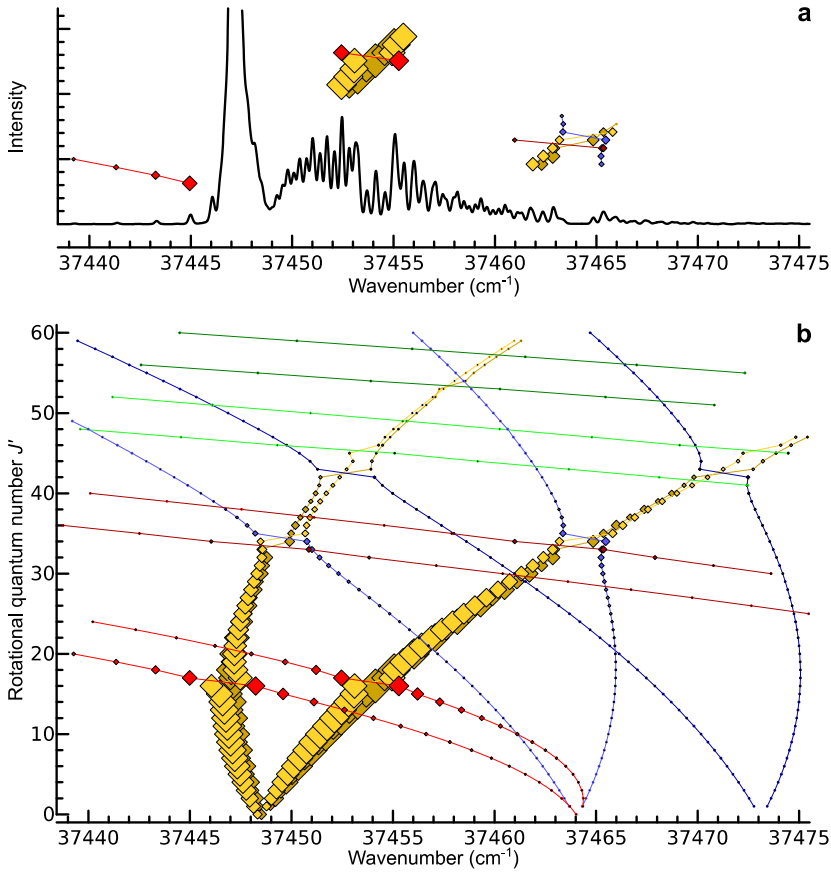

Figure 20: The underlying structure of a heavily perturbed band

a Simulation of the (0-0) J-X vibronic band of the copper dimer, limited to the two most abundant isotopologues. The irregular shape of the band originates from perturbations of the electronic J state by several dark states.

b Fortrat diagram of the same region, revealing the individual interactions occurring between the bright J state (yellow) and three dark states, G_{62} (red), $L1$ (blue), G_{63} (green), in both $^{63}Cu_2$ (dark colors) and $^{65}Cu^{63}Cu$ (light colors). While the color denotes the vibronic state, the area of the colored square indicates the intensity of the individual line. Band transitions are connected by lines to guide the eye. As dipole selection rules for this bands dictate that the rotational quantum number can change only by ±1 for a given initial J'', two branches occur for each state, a P and R-branch with $\Delta J = J' - J'' = -1$ and $\Delta J = +1$, respectively. Primes and double primes designate the excited and ground state quantum numbers, respectively.

As there is no way to extract the data in the Fortrat diagram from an experimental one-photon spectrum (as in the one simulated in Figure 20a), the underlying information on the molecular constants of the vibronic states and the interactions among them need to be obtained by a different experimental approach that simplifies the spectrum. In this work, we used TC-RFWM as a spectroscopic method (see Chapter 2.3.1.1). While this Optical-Optical Double Resonance (OODR) technique enables us to do spectroscopy on individually addressed quantum states of single isotopologues, the complex process of signal generation raises substantial requirements on the experimental set-up. In particular, the target dimeric species needs to be provided with both a high and a stable number density, which was only recently achieved (Chapter 5.1).

5.3.2 Rotational disentanglement of bands

TC-RFWM allows spectra to be collected that originate from a single known J'' level of the ground state X. The resulting spectra contain only one R, one P, and sometimes one Q line, depending on the symmetry of the excited state. This capability greatly simplifies the analysis of the spectra, especially in cases where perturbations destroy the regularity of rotational levels in the upper state. When a bright state is perturbed by a dark state, the quantum mechanical mixing of these states causes their energies to shift, but also the strengths of related transitions to redistribute. Hence, the dark state becomes detectable for rotational levels where both states are sufficiently close in energy to perturb each other substantially.

Figure 21a illustrates this effect on transitions from the ground state into the vibrationally excited J (v=2) state of the $^{65}Cu^{63}Cu$ dimer. Analogous to the computed Fortrat diagram in Figure 20b, the experimental spectra are arranged as a function of the rotational quantum number J'' in the ground state, which was directly provided by the applied method. As a result of the ordering in the ground state, the intersections of perturbing dark states

appear shifted by two rotational levels, when comparing the P-branch (ΔJ=−1) with the R-branch (ΔJ=+1). For some spectra, additional lines were visible and others remained unassigned, because of spectral overlap in the band used to determine J'' in the ground state. Such ambiguities can be resolved by using another transition to access the same J'. Figure 21b depicts the ordering and relative spacing between the rotational levels of the observed vibronic states. Most obvious is the strong interaction between the J (v=2) state and the vibronic state preliminarily labelled as G_{68}. The label G_{68} was chosen on purpose, as this level is part of a series of vibrational levels that was observed across all measured vibrational levels of the electronic J state. Using the isotopic shifts, it can be assumed that G_{68} corresponds to a vibrational level about v = 68, while its properties (*vide infra*) suggest an assignment to the electronic G state[1]. At its culmination, between rotational levels J = 29 and J = 30, the repulsion of these levels increases their separation from 2 to 10 cm^{-1}.

The perturbations between the J and G states have been analyzed by assuming a homogeneous perturbation on the basis of the observed effective rotational quantum numbers (Table 8). Mostly, both P and R branch transitions were observed with sufficient intensity. In contrast, the vibronic state preliminarily labelled $O1$ exhibits a combination of interesting properties. Starting from low rotational levels, the dark $O1$ state just becomes visible at its intersection with the J (v=2) state, where it causes a splitting of about 0.4 cm^{-1} at J = 14. However, in this range only the P-branch is visible. From J = 15 onwards the situation reverses and only the R-branch is visible. Further afield of the intersection, it does not fully disappear as expected from a dark state. Finally, $O1$ approaches the intersection with G_{68} where no significant splitting is added on top of the natural separation of about 1 cm^{-1} between the levels of $O1$ and G_{68}, the behavior of $O1$ changes again and we did not detect a single $O1$ line across the second intersection. Intensity anomalies between P(J+1) and R(J−1) lines have been observed and

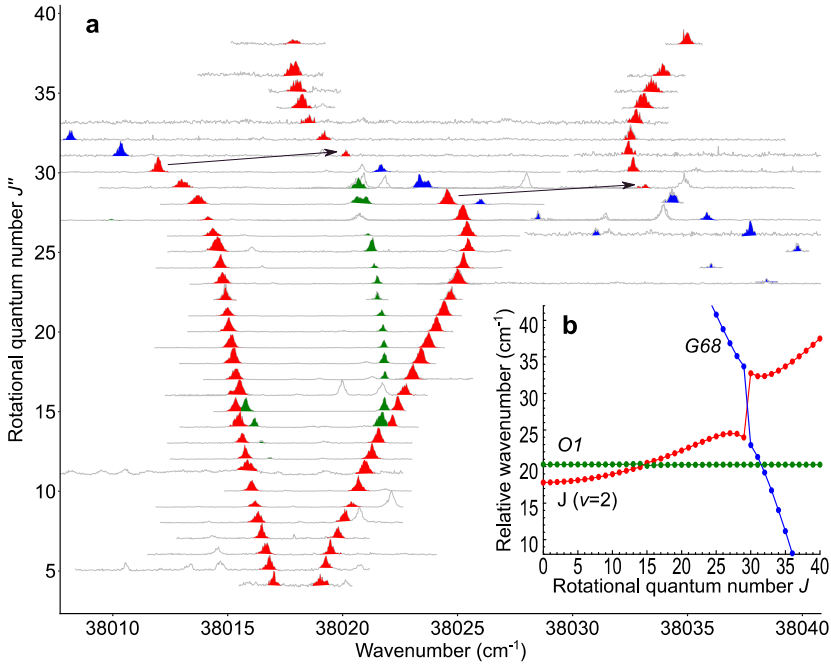

Figure 21: An experimental Fortrat diagram
a A series of two-color resonant four-wave mixing (TC-RFWM) spectra ordered by the experimentally determined rotational quantum number *J*'' of the ground state X0+g is shown. The regions of unambiguously assigned lines of the $^{65}Cu^{63}Cu$ isotopologue are colored based on the excited electronic state (blue: *G*68, green: *O*1 and red: J (*v* = 2)).
b The corresponding rovibronic levels are plotted, based on molecular constants fitted to the assigned line positions. For clarity, the energy scale was reduced by taking into account the rotational constant *B* of one state to straighten the parabolas.

attributed to the mixing of perturbing states.[71] The effect can be explained by quantum mechanical interference that comprises information on the perturbation class. For example, parallel and perpendicular transitions (with an orbital angular momentum change $\Delta\Lambda$ = 0 or ±1, respectively) display approximately equal intensities for the P(*J*+1) and R(*J*−1) lines for unperturbed states. If a perturbation occurs (L-uncoupling) between two states exhibiting an angular momentum difference of $\Delta\Lambda$ = ±1, the relative

intensity of the branches out of this state can be affected strongly. For parallel transitions the amplitude phases of P and R are identical while for perpendicular transitions they are opposite. As a consequence, P line interference is constructive and the R line interferes destructively and the branch may disappear completely.[24] Numerous intensity anomalies occurring due to perturbation have been observed and their intensity patterns contain information on the class of perturbation (ref. [24] and references therein). Additional information on perturbation effects is accessible by considering saturation and polarization features of the background-free double-resonant method applied in this work. In a simplified spectrum, exhibiting only few transitions owing to the stringent double-resonance selection rules, partially forbidden features (weak "extra lines" obtaining oscillator strength through perturbation) can be observed at high laser intensities. Even though bright transitions might substantially broaden upon saturation, they are in general well separated from the "extra lines" that are made visible at increased laser powers. Furthermore, specific linear and circular polarization configurations of the two resonant lasers allow further enhancement or discrimination of entire families of rovibronic transitions for the characterization of perturbation effects.[72] Considering the quantum mechanical interference for perturbed levels involving perpendicular transitions, L-uncoupling is suggested for the $O1 \sim G_{68}$ system and consequently a 1_u symmetry label for the $O1$ state. However, the classification of these perturbations requires more detailed experiments and is beyond the scope of this work.

Table 8: Molecular constants of the deperturbed vibronic states of $^{63}Cu_2$

Level	T_v	B_v	D_v
J (v=0)	37448.8417(70)	0.1156040(149)	6.49(52)e-8
J (v=1)	37736.7187(437)	0.1147198(382)	7.230(962)e-8
J (v=2)	38022.4414(243)	0.1138145(459)	9.45(204)e-8
G62	37513.6802(84)	0.058225(12)	
G63	37615.6*	0.0580*	
G64	37717.4036(545)	0.05788(10)	
G65	37818.6986(74)	0.0574771(85)	
G66	37919.3*	0.0573*	
G67	38020.048(30)	0.05698(12)	
G68	38120.011(164)	0.0567581(962)	
L1	37473.0678(668)	0.1024331(428)	
M1	38032.871(135)	0.099883(153)	
N1	38035.144(46)	0.07834(13)	
Perturbation	Strength		
<J (v=0)||*G62*>	1.153(11)		
<J (v=0)||*G63*>	1.1†		
<J (v=1)||*G64*>	2.514(218)		
<J (v=1||*G65*>	2.7194(71)		
<J (v=1||*G66*>	2.6†		
<J (v=2||*G67*>	5.171(16)		
<J (v=2||*G68*>	4.8045(73)		
<J (v=0)||*L1*>	1.2949(89)		
<J (v=2||*M1*>	0.345(11)		
<J (v=2||*N1*>	0.8866(83)		

All values in units of cm^{-1} (with one standard deviation in units of the last figure appended in parentheses).

T_v: origin (sum of electronic term T_e and vibrational term $G(v)$).

B_v: mean value of the rotational constant B in the vibrational state v.

D_v: mean value of the centrifugal distortion constant D in the vibrational state v.

* interpolated values.

† presumed values based on the other isotopologue.

Table 8b: Molecular constants of the deperturbed vibronic states of $^{63}Cu^{65}Cu$

Level	T_v	B_v	D_v
J (v=0)	37448.7096(95)	0.1138453(198)	7.425(837)e-8
J (v=1)	37734.3031(79)	0.1129210(174)	4.950(677)e-8
J (v=2)	38017.7408(81)	0.1120462(336)	1.18(25)e-7
G62	37464.8515(255)	0.057551(22)	
G63	37567.349(467)	0.056779(228)	
G64	37667.6*	0.0569*	
G65	37768.355(17)	0.056719(17)	
G66	37868.530(168)	0.0565208(720)	
G67	37968.5*	0.0563*	
G68	38067.939(33)	0.056131(44)	
L1	37463.8282(451)	0.1009676(354)	
O1	38020.244(18)	0.100307(34)	
Perturbation	Strength		
<J (v=0)||*G62*>	1.265(14)		
<J (v=0)||*G63*>	1.061(13)		
<J (v=1)||*G64*>	2.5†		
<J (v=1)||*G65*>	2.7288(74)		
<J (v=1)||*G66*>	2.590(13)		
<J (v=2)||*G67*>	5.2†		
<J (v=2)||*G68*>	4.8193(66)		
<J (v=0)||*L1*>	1.1064(61)		
<J (v=2)||*O1*>	0.1944(88)		
<*L1*||*G62*>‡	1.872(53)		

All values in units of cm^{-1} (with one standard deviation in units of the last figure appended in parentheses).

T_v: origin (sum of electronic term T_e and vibrational term $G(v)$).

B_v: mean value of the rotational constant B in the vibrational state v.

D_v: mean value of the centrifugal distortion constant D in the vibrational state v.

* interpolated values.

† presumed values based on the other isotopologue.

‡ a fit parameter used for approximation of overall effects by these states and at least one additional unknown perturber.

5.3.3 Isotope-selective tracing of dark bands

As the dark states exhibit different properties than the bright ones, the resulting mixed states can also act as gateways for perturbation-facilitated studies of other dark regions of the studied system.[34] For the copper dimer, a good example is provided by the series of vibrational levels that were preliminarily assigned to the G state. In a previous work, we could already affirm computationally that the B state and the G state emerge from the avoided crossing between a covalent bound state and an ion-pair state.[73] Transitions into ion-pair states are known for their high transition strength. As a consequence, strong emission into the vibronic ground state X (v=0) is observed from the B state, which has ion-pair character at the inner potential wall (towards low internuclear distance). By implication, the G state should provide similar properties at its outer potential wall. Owing to the shallow potential, this wall is located at a large internuclear distance, so that no vertical transitions into X (v=0) are possible. On the contrary, strong transitions from the outer potential wall of G would, if they exist, occur into highly excited vibrational levels of X. While scanning the (0-0) J – X band in the deep-ultraviolet range, we indeed found strong blue fluorescence, which corresponds to transitions into the ground state X at vibrational levels starting at v=83. Further analysis revealed that the vibronic state G_{62}, which is shown in red in Figure 20, is responsible for this. Only lines belonging to or perturbed by G_{62} exhibit this fluorescence. Figure 22 depicts excitation scans in which a spectrometer was used to split the laser-induced fluorescence into individual vibronic bands. In Figure 22a, the ultraviolet emission close to the excitation wavelength was chosen. Most extra features visible in Figure 20a disappear and just some particular changes in intensity indicate that this still is a heavily perturbed band. Taking a look at the blue fluorescence around ≈452 and 446 nm in Figure 22b, c, respectively, it becomes obvious why these features were missing. Already J levels that are sharing only a fraction of G_{62} character, strongly emit in the blue and deplete the excited

population rapidly. Therefore, the weaker UV fluorescence is strongly suppressed.

The fast emission of a photon in a totally different spectral range gives these excitation scans a high sensitivity for detecting the dark states. While the nonlinear four-wave mixing discloses the strongly perturbed lines of the dark

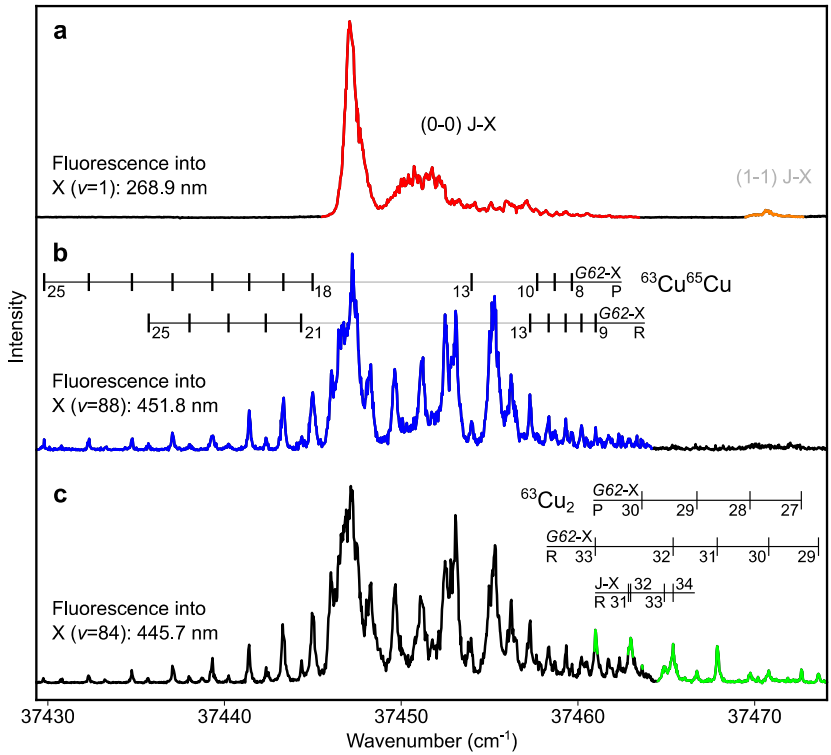

Figure 22: Spectral decomposition of the laser induced fluorescence
Excitation scans around the (0-0) J-X region of the copper dimer.
a Fluorescence of J ($v = 0$), into the first vibrational excited level $v = 1$ of the ground state X (red). In addition, the (1-1) hot band is weakly visible, as its emission into $v = 2$ occurs just 0.2 nm below (orange).
b Fluorescence into $v = 88$. Only the $^{63}Cu^{65}Cu$ isotopologue is visible (blue).
c Fluorescence into $v = 84$. Both isotopologues, $^{63}Cu^{65}Cu$ (black) and $^{63}Cu_2$ (green), are observed simultaneously. Assignments indicate the rotational quantum numbers of the J and G_{62} to X transitions for two isotopologues, which are defined by taking into account the unambiguous results obtained by four-wave mixing.

states close to their intersection with the bright state, the linear, incoherent method is more suitable for the observation of the weak transitions that are energetically more separated. TC-RFWM intensities depend quadratically on the population whereas laser-induced fluorescence intensities depend linearly, which is advantageous in the low-density environment of a molecular beam. In addition, the nonlinear method depends on different powers of the transition moment as the level of saturation changes[74] and is therefore further limiting the detection of weak transitions.

In Figure 22b, c numerous rotational levels of the dark G_{62} state are observed that are below the detection limit of four-wave mixing. The excitation scan in Figure 22b is obtained by monitoring the emission into the highly excited v = 88 level of the ground state X in the $^{65}Cu^{63}Cu$ isotopologue. The scan displays rotational levels of the G_{62} dark state up to J' = 25. The isotope shift of v = 84 in the ground state is not sufficiently large to separate the emission of the two main isotopologues by the limited resolution of the spectrometer. As a consequence, weak $^{63}Cu_2$ rotational P and R branch transitions up to J' = 33 of G_{62} are observed in addition as shown in the Figure 22c. In spite of the complex appearance of the excitation scans, the assignment of the dark states transitions is straightforward on the basis of the more intense transitions to the dark state that are unambiguously defined by double-resonance labelling.

5.3.4 Visualisation and deperturbation

By combining TC-RFWM and excitation scans, we could unambiguously assign approximately 1600 rovibronic lines in the vicinity of the J state of $^{63}Cu_2$ and $^{63}Cu^{65}Cu$. While the complete line list is appended in appendix Chapter 10.5, Figure 23 illustrates the data graphically by compiling all scans into a single plot. Only non-overlapping line positions were assigned, though some lines appear to overlap in this depiction. Many of the reported lines were assigned more than once. While this improves the statistics in

determination of the line position, the invariance of a line on change of the double-resonant excitation scheme also guarantees the correct assignment. As different excitation schemes involve different overlaps in the transition used for selecting the rotational quantum state, only the correctly assigned lines will remain at the same position.

Next to transitions into the three lowest vibrational bands of the electronic J state (shown in shades of blue), Figure 23 is dominated by transitions into two vibrational levels of the I state (shown in crimson tones). As the vibrational ground state of the I state was never observed, we use preliminary labels for its levels. *I*1 and *I*2 correspond to *v* = "*x*+1" and *v* = "*x*+2", respectively, in the nomenclature used by Powers *et al.*[14]. While transitions into the J state, and all dark states borrowing intensity from it, only exhibit P and R branches, the I state, whose different symmetry was already described in Chapter 5.1, also exhibits a Q branch. Brought to light by the excitation scans, the G_{62} and G_{65} bands fill significant image area, mostly by their raw spectra plotted in grey. The other *G* bands, as well as the unrelated *L*1, *M*1, *N*1 and *O*1 bands, were only measured close to their intersection with the electronic J state. The interaction of the *G* levels with the electronic J state increases for higher vibrational excitation, therefore, at higher vibrational levels *v* of the J state, an increasing number of rotational levels became visible also when employing four-wave mixing spectroscopy. In case of G_{67}, some levels became visible even without an actual intersection with the J (*v*=2) state. This was additionally favored by a high thermal population in the observed rotational range. Sufficient *J*'-levels were obtained in this system to evaluate the symmetry of the perturber (see Chapter 10.1.3). Based on the experimentally obtained line positions, we fitted molecular constants for the involved states. For the J state and the perturbing dark states, a deperturbation was possible. By this, we were able to not only obtain the molecular constants of these states, but also their interaction strengths (Table 8). For the *G* and *L* levels, also the calculated

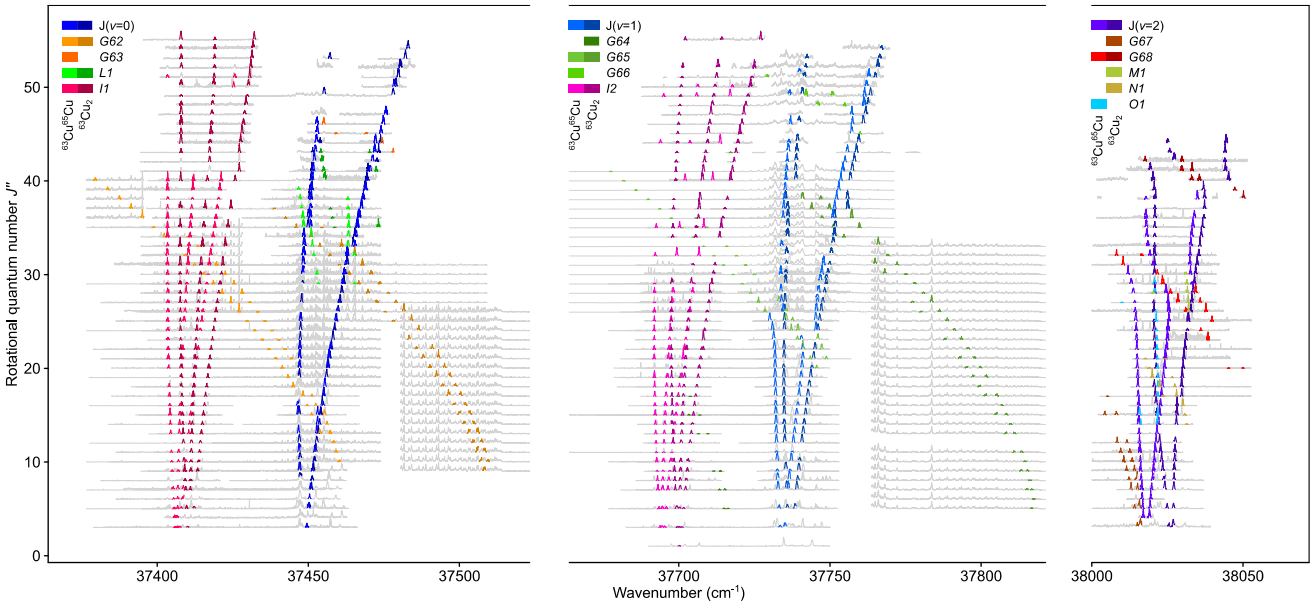

Figure 23: Overview of all assigned lines

Total view of the transitions that were rotationally assigned in this work. The regions containing assigned lines are printed color-coded, while the containing raw spectra are printed in grey. The colors denote the isotopologues and the vibronic states that were accessed by transitions from the vibronic ground state X ($v = 0$) with the corresponding rotational quantum number J'' as denoted on the ordinate. Starting from the bright transitions that were unambiguously assigned by double-resonant selection of J'', blocks of excitation scans into the dark regimes could be also assigned by numbering consecutively.

isotope shifts could be utilized for verification. For the J state, the data of both isotopologues were combined to refine the equilibrium constants. The resulting equilibrium constants for $^{63}Cu_2$ are presented in Table 9. More details are provided in Chapter 10.1.3. The I state is an anomaly in many respects. Only a few vibrational levels have been observed and even these are too weak to be observed by most methods. We previously reported its short fluorescence lifetime and molecular constants of seemingly unperturbed regions (Chapter 5.1).[75] The I state seems not to interact with the other states characterized in this work, but nevertheless is subject to a complicated pattern of perturbations. Therefore, the I state should be revisited in a subsequent study, so that the perturbing states may be investigated more thoroughly. Such a study can also help to assign the unrelated bands (*L*1, *M*1, *N*1 and *O*1) to specific electronic states. To be used for experimental purposes only, molecular constants that reproduce the observed range were added as Table 10.

Table 9: Equilibrium Constants of the J state of $^{63}Cu_2$

Constant	This work	Previous work[75]
T_e [cm^{-1}]	37437.107(95)	37437.20(33)
ω_e [cm^{-1}]	289.93(16)	289.40(88)
$\omega_e x_e$ [cm^{-1}]	1.075(53)	(0.64(44)[14])
B_e [cm^{-1}]	0.116062(12)	0.116218(54)
α_e [cm^{-1}]	0.0009123(77)	0.001323(40)
r_e [Å]	2.14853(11)	2.14708(50)

Values in parentheses denote one standard deviation in the last digit.
T_e: equilibrium electronic term.
ω_e: equilibrium vibrational constant.
x_e: equilibrium anharmonicity constant.
B_e: equilibrium rotational constant.
α_e: equilibrium vibration-rotation interaction constant.
r_e: equilibrium internuclear separation.

Table 10: Apparent molecular constants of the I state

	$^{63}Cu_2$				
Level	T_v	B_v	D_v	q_v	H_v
I1	37410.7859(76)	0.112440(27)	1.59(22)e-7	-1.456(47)e-4	-9.13(51)e-11
I2	37700.1238(64)	0.113071(14)	4.13(53)e-8	3.68(53)e-5	
	$^{63}Cu^{65}Cu$				
Level	T_v	B_v	D_v	q_v	
I1	37406.6047(61)	0.110851(14)	4.854(69)e-7	6.62(83)e-5	
I2	37694.3950(64)	0.111445(18)	5.55(76)e-8	1.56(93)e-5	

All values in units of cm^{-1}.
T_v: origin (sum of electronic term T_e and vibrational term $G(v)$).
B_v: mean value of the rotational constant B in the vibrational state v.
D_v: mean value of the quadratic centrifugal distortion constant D in the vibrational state v.
q_v: mean lambda doubling constant q in the vibrational state v.
H_v: mean value of the sextic centrifugal distortion constant H in the vibrational state v.

5.4 Conclusion

TC-RFWM spectroscopy allows overcoming the hindrances that have so far prevented experimental access to systems exhibiting a high density of states. Perturbations identified by this method can be used as gateways for experimental access into otherwise inaccessible regions, including the near-dissociation regime of the ground state. These mixed states oscillate between high- and low-vibrational quanta for large and small internuclear distances, respectively. While at short distance, a model based on the linear combination of atomic orbitals is appropriate, ligand-field theory might be better suited to address the behavior at long range.[76] The large size of the 4s and 4p orbitals serves to de-shield the atomic-ion cores from each other, leading to a positive point charge perturbing the 3d structures on the other atom. This relates to the foundational concept of "oxidation state"[****], which

[****] This conceptual reasoning should not be confused with the formal IUPAC definition of the oxidation state.

could be more properly thought of as the charge on one atom as seen by the atom to which it is bound [Field, R. W., personal communication (2019)]. The features of the nonlinear method open a wide field for future experiments on transition metal systems. The presented data also provide reference data to test new quantum chemical methods for computational handling of systems with a high density of states. Such insights lead to fundamental understanding of the complex electronic structure of transition metal clusters that govern their functionality. Ion-pair states, respectively, the states that originate from their avoided crossings with other states, affect almost all regions of the potential energy landscape of the copper dimer. Considering the commonness of perturbation-facilitated mixing between these and other quantum states, it is unlikely that other transition metal systems, which usually exhibit an even higher density of states, can be understood based on the assumption of pure states and the usage of the Born-Oppenheimer approximation. Even for the copper dimer itself, a glance behind the veil of overlapping lines exposed not only a complex network of perturbations, but also vibronic bands displaying interesting properties to access regions of the energy map beyond the possibilities of more conventional spectroscopic methods.

6 Summary

In Chapter 3 we describe the commissioning and further development of the laser ablation metal cluster source built for this work. Starting from a prototype already designed at the Paul Scherrer Institut, significant rework finally lead to a reliable source, meeting the high requirements established by the use of TC-RFWM spectroscopy. During commissioning, several mechanical design changes were necessary, on both the target mount and the sealing between the target assembly and the base plate. This process resulted in the design introduced in Chapter 3.1, which enabled our first spectroscopic studies on the copper dimer. Nonetheless, the cluster source was still far from reliable and the further changes are still implemented, even while this thesis is written. After a mode of operation for the electromechanical components had been established (Chapter 3.2), the main issues were related to achieve sufficient gas sealing. Chapter 3.3 describes the measures taken to improve sealing tightness. Mass spectra using different target elements were obtained using fs-ionization time-of-flight mass spectroscopy (Chapter 3.4). A clearly matured version of the cluster source, which achieved up to 150 hours of stable operation, is described in Chapter 3.5. Finally, Chapter 3.6 give an outlook on further redesigns already scheduled.

After proof of concept measurements on already known states of the copper dimer, an unexpectedly found low-lying electronic state gave rise to a combined spectroscopic and computational study in this range (Chapter 4). The optical detection of this state (Chapter 4.2) demonstrates the relevance of spin-orbit coupling, which changes the Hund's coupling case and makes this state optically accessible, also for a light transition metal like copper. Combining this finding with the already experimentally known relevance of ion-pair states (Chapter 2.1), this inspired the construction of a reduced

active space that finally allowed a first accurate description of the low-lying electronic states using quantum chemical *ab initio* methods (Chapter 4.3).

Changing from blue to deep UV laser light, Chapter 5 gives insight into the high-lying electronic states of the copper dimer. In this region, which so far resisted all attempts of in-depth characterization, both by experimental and theoretical approaches, we could directly decide term symbols and molecular constants (Chapter 5.2). However, these constants were only established for one isotopologue based on a seemingly unperturbed range of rovibronic lines, as a large number extra lines (contributed by several perturbing states) hindered the analysis by shifting line positions. Therefore, both the rotational and the vibrational range of the measurements were extended, but this resulted in the appearance of even more perturbing states. Still, utilizing a mixture of TC-RFWM and LIF excitation scans, we were finally able to identify patterns and could establish a full deperturbation study, which is presented in Chapter 5.3. The rich network of perturbations gives an impression on the complicated electronic structure present in excited transition metal systems. Next to demonstrating a method for spectroscopic studies on such systems, the obtained data set also provides experimental reference to test new computational approaches. Some of the possible implications of these findings are presented in the following chapter.

7 Outlook

7.1 The ground state of the copper dimer

In chapter 5.3.3, fluorescence into highly excited vibrational levels of the ground state X were utilized to characterize the dark vibronic levels G_{xx} by applying excitation scans. As a side effect, this allows to characterize also the ground state at energies close to its dissociation. Utilizing that the wave functions of the mixed G_{xx}∼J states overlap with wave functions of all vibrational levels of the ground state, optical access to all bound vibrational levels is enabled. According to preliminary analysis of data that will be treated after this thesis is completed, even transitions into unbound states slightly above dissociation of the ground state, so called bound-free transitions, were observed. Pumping a single rovibronic level of the G_{xx}∼J system, which also implies pumping a single isotopologue, all vibrational levels of the ground states X can be characterized. Obviously, the nodes in the wave function of the pumped mixed state will suppress emission into some levels, but in the smooth ground state potential, this is no obstacle. Utilizing TC-RFWM in a stimulated emission pumping scheme, strong transitions (comparable to those used in chapter 5.3.3) can be resolved with full laser resolution. Therefore, for the first time, the complete ground state potential curve of a transition metal dimer can be experimentally determined and the existing models can be corrected.

7.2 Basics of small transition metal systems

The presented work was simplified by previous knowledge on the copper dimer, and also by its “simple” ground state electronic configuration. This, however, does not imply a loss of generality. The method can be directly applied on comparable homo- and heteronuclear systems. An obvious

example would be the chromium dimer, exhibiting a formal bond order of 6 and a ground state potential of highly anharmonic shape.[77] While different quantum chemical approaches resulted in a various shapes of this potential, some even predicting a double-well shape[78], an analogous approach to our work on the copper dimer could yield a definitive clarification.

Next to studies of pure transition metal systems, the same setup could also be used for studies of reacted clusters. E.g. by dosing oxygen into the buffer gas, one would produce oxygen bridged transition metal clusters, which, already for the example of copper, are the proposed active sites in numerous metalloenzymatic[79] but also man-made catalytic systems[80].

7.3 Perturbation-facilitated chemistry

Taking a look beyond the borders of fully established knowledge, the findings in this work allow to put forward hypotheses on the mechanisms underlying the unique catalytic functionalities provided by transition metal species. Nature demonstrates that the activity of enzymes, which is provided by transition metal cofactors, can be controlled by remote allosteric sites. These often have no significant effect on the structure of the active sites, but can still activate or inhibit them. While it is unlikely that these minor structural changes imply pronounced changes in properties like oxidation states, the relative energies between the electronic states of the transition metal cofactors are sensitive to changes in the chemical environment. In the light of this work, it's obvious to relate this to a reordering in the network of perturbations between the involved quantum states. This might explain the limited success to reproduce catalysis by computation, as these mixing is ignored in the Born-Oppenheimer approximation, which underlies most theoretical methods. However, if perturbation is really key to the catalytic properties of transition metals, understanding of these effects would allow rational design of a new generation of catalysts, in which modeling of the environment of the active sites programs the reaction that should be

selectively catalyzed. Thereby, the electronic structure of the environment acts both as sensor and as logical circuit. The functionality of the transition metal active site would be quite versatile, as perturbations can bridge spin manifolds, covalent and ionic states, bond lengths, and so on. To weaken a bond, one could e.g. mix in properties of a state where a d electron is promoted to an s orbital to cause Pauli repulsion. A systematic study of functional environments is eased by the fact that, compared to biological models, one is not restricted by natural abundance and biocompatibility, but can utilize the complete periodic table.

8 Bibliography

1 Morse, M. D. in *Advances in Metal and Semiconductor Clusters* Vol. 1 (ed M. A. Duncan) 83-121 (JAI Press, 1993).

2 Bondybey, V. E. The Lowest-a 3-Sigma-U+ State of Cu2. *J Chem Phys* **77**, 3771-3772, doi:10.1063/1.444245 (1982).

3 Herzberg, G. *Spectra of diatomic molecules*. 2nd ed. edn, Vol. 1 (New York : Van Nostrand Reinhold, 1950).

4 Kleman, B. & Lindkvist, S. The Band-Spectrum of the Cu2-Molecule. *Ark Fys* **8**, 333-339 (1954).

5 Ruamps, J. Spectre Demission Des Molecules Cu-2, Ag-2 Et Au-2. *Cr Hebd Acad Sci* **238**, 1489-1491 (1954).

6 Aslund, N., Barrow, R. F., Richards, W. G. & Travis, D. N. Rotational Analysis of Bands of B-X System of Cu2 and of A-X System of Bi2. *Ark Fys* **30**, 171-185 (1965).

7 Pesic, D. S. & Weniger, S. Rotational Analysis of Bands of A-X System of Cu2 (Cu-63). *Cr Acad Sci B Phys* **273**, 602-& (1971).

8 Lochet, J. Laser-Induced Fluorescence of Cu2 Molecule. *J Phys B-at Mol Opt* **11**, L55-&, doi:10.1088/0022-3700/11/3/001 (1978).

9 Mccaffrey, J. G., Bennett, R. R., Morse, M. D. & Breckenridge, W. H. Laser Excitation Spectroscopy of the A-State and B-State of Jet-Cooled Copper Dimer - Evidence for Large Electronic Isotope Shifts. *J Chem Phys* **91**, 92-103, doi:10.1063/1.457454 (1989).

10 Preuss, D. R., Pace, S. A. & Gole, J. L. Supersonic Expansion of Pure Copper Vapor. *J Chem Phys* **71**, 3553-3560, doi:10.1063/1.438811 (1979).

11 Page, R. H. & Gudeman, C. S. Rotationally Resolved Dicopper (Cu2) Laser-Induced Fluorescence-Spectra. *J Chem Phys* **94**, 39-51, doi:10.1063/1.460355 (1991).

12 Bondybey, V. E. & English, J. H. Observation and Characterization of a New Electronic State of Cu-2 in Solid Neon. *J Phys Chem-Us* **87**, 4647-4650, doi:10.1021/j100246a023 (1983).

13 Morse, M. D. Clusters of transition-metal atoms. *Chem Rev* **86**, 1049-1109, doi:10.1021/cr00076a005 (1986).

14 Powers, D. E., Hansen, S. G., Geusic, M. E., Michalopoulos, D. L. & Smalley, R. E. Supersonic Copper Clusters. *J Chem Phys* **78**, 2866-2881, doi:10.1063/1.445273 (1983).

15 Rohlfing, E. A. & Valentini, J. J. UV laser excited fluorescence spectroscopy of the jet-cooled copper dimer. *The Journal of Chemical Physics* **84**, 6560-6566, doi:10.1063/1.450708 (1986).

16 Sappey, A. D., Harrington, J. E. & Weisshaar, J. C. Resonant 2-Photon Ionization-Photoelectron Spectroscopy of Cu-2 - Autoionization Dynamics and Cu-2+ Vibronic States. *J Chem Phys* **91**, 3854-3868, doi:10.1063/1.456870 (1989).

17 Ram, R. S., Jarman, C. N. & Bernath, P. F. Fourier-Transform Emission-Spectroscopy of the Copper Dimer. *J Mol Spectrosc* **156**, 468-486, doi:10.1016/0022-2852(92)90247-L (1992).

18 Okazaki, T. & Ando, Y. New optical absorption spectra of Cu2 molecules produced by the gas evaporation technique. *Mol Phys* **98**, 447-452, doi:10.1080/00268970009483310 (2000).

19 Lebedev, V., Moroshkin, P., Toennies, J. P. & Weis, A. Spectroscopy of the copper dimer in normal fluid, superfluid, and solid He-4. *J Chem Phys* **133**, doi:10.1063/1.3497643 (2010).

20 Parry, I. S., Hermes, A. C., Kartouzian, A. & Mackenzie, S. R. Imaging the photodissociation dynamics of neutral metal clusters: copper dimer, Cu2, and copper oxide, CuO. *Physical Chemistry Chemical Physics* **16**, 458-466, doi:10.1039/C3CP53214C (2014).

21 Gagliardi, L. & Roos, B. O. Quantum chemical calculations show that the uranium molecule U-2 has a quintuple bond. *Nature* **433**, 848-851, doi:10.1038/nature03249 (2005).

22 Knecht, S., Jensen, H. J. A. & Saue, T. Relativistic quantum chemical calculations show that the uranium molecule U-2 has a quadruple bond. *Nat Chem* **11**, 40-44, doi:10.1038/s41557-018-0158-9 (2019).

23 Bishea, G. A. & Morse, M. D. Spectroscopic studies of jet-cooled AgAu and Au2. *The Journal of Chemical Physics* **95**, 5646-5659, doi:10.1063/1.461639 (1991).

24 Lefebvre-Brion, H. & Field, R. W. *The Spectra and Dynamics of Diatomic Molecules*. (Academic Press, 2004).

25 Buntine, M. A., Chandler, D. W. & Hayden, C. C. A two-color laser-induced grating technique for gas-phase excited-state spectroscopy. *The Journal of Chemical Physics* **97**, 707-710, doi:10.1063/1.463567 (1992).

26 Butenhoff, T. J. & Rohlfing, E. A. Resonant 4-Wave-Mixing Spectroscopy of Transient Molecules in Free Jets. *J Chem Phys* **97**, 1595-1598, doi:10.1063/1.463234 (1992).
27 McCormack, E. F., Pratt, S. T., Dehmer, P. M. & Dehmer, J. L. Observation of Hyperfine Quantum Beats in 2-Color Laser-Induced Grating Spectroscopy of Nitric-Oxide. *Chem Phys Lett* **227**, 656-662, doi:Doi 10.1016/0009-2614(94)00875-2 (1994).
28 Buntine, M. A., Chandler, D. W. & Hayden, C. C. Detection of Vibrational-Overtone Excitation in Water Via Laser-Induced Grating Spectroscopy. *J Chem Phys* **102**, 2718-2726, doi:Doi 10.1063/1.468648 (1995).
29 Rohlfing, E. A., Tobiason, J. D., Dunlop, J. R. & Williams, S. Two-color resonant four-wave mixing: A tool for double resonance spectroscopy. *Proc. SPIE* **2548**, 209-219, doi:10.1117/12.220849 (1995).
30 Rokni, M. & Yatsiv, S. Stimulated Electronic Raman Effect and Parametric Anti-Stokes Radiation in Potassium Vapor. *Ieee J Quantum Elect* **Qe 3**, 329-&, doi:10.1109/Jqe.1967.1074595 (1967).
31 Oudar, J. L. & Shen, Y. R. Nonlinear spectroscopy by multiresonant four-wave mixing. *Phys Rev A* **22**, 1141-1158, doi:10.1103/PhysRevA.22.1141 (1980).
32 Green, D. S. *et al.* Boundary Layer Profiles in Plasma Chemical Vapor Deposition. *Science* **259**, 1726, doi:10.1126/science.259.5102.1726 (1993).
33 Western, C. M. PGOPHER. A Program for Simulating Rotational, Vibrational and Electronic Spectra, doi:10.5523/bris.160i6ixoo4kir1jxvawfws047m (University of Bristol, 2017).
34 Bornhauser, P. *et al.* Perturbation-facilitated detection of the first quintet-quintet band in C_2. *J Chem Phys* **142**, doi:10.1063/1.4913925 (2015).
35 Fowler, A. Investigations relating to the Spectra of Comets. (Plate 14.). *Mon Not R Astron Soc* **70**, 484-490, doi:10.1093/mnras/70.6.484 (1910).
36 Bornhauser, P., Sych, Y., Knopp, G., Gerber, T. & Radi, P. P. Shedding light on a dark state: The energetically lowest quintet state of C2. *The Journal of Chemical Physics* **134**, 044302, doi:10.1063/1.3526747 (2011).

37 Babb, J. F., Smyth, R. T. & McLaughlin, B. M. Dicarbon Formation in Collisions of Two Carbon Atoms. *The Astrophysical Journal* **876**, 38, doi:10.3847/1538-4357/ab1088 (2019).

38 Williams, S., Rohlfing, E. A., Rahn, L. A. & Zare, R. N. Two-color resonant four-wave mixing: Analytical expressions for signal intensity. *J Chem Phys* **106**, 3090-3102, doi:10.1063/1.473052 (1997).

39 Bornhauser, P. *et al.* Experimental and theoretical investigation of the vibrational band structure of the $1\ ^5\Pi_u - 1\ ^5\Pi_g$ high-spin system of C_2. *J Chem Phys* **146**, doi:10.1063/1.4978334 (2017).

40 Visser, B. *et al.* New experimental and theoretical assessment of the dissociation energy of C_2. *Mol Phys*, 1-8, doi:10.1080/00268976.2018.1564849 (2019).

41 Szalay, P. G., Muller, T., Gidofalvi, G., Lischka, H. & Shepard, R. Multiconfiguration Self-Consistent Field and Multireference Configuration Interaction Methods and Applications. *Chem Rev* **112**, 108-181, doi:10.1021/cr200137a (2012).

42 Knowles, P. J. & Werner, H.-J. An efficient method for the evaluation of coupling coefficients in configuration interaction calculations. *Chem Phys Lett* **145**, 514-522, doi:10.1016/0009-2614(88)87412-8 (1988).

43 Werner, H. J. & Knowles, P. J. An efficient internally contracted multiconfiguration–reference configuration interaction method. *The Journal of Chemical Physics* **89**, 5803-5814, doi:10.1063/1.455556 (1988).

44 Knowles, P. J. & Werner, H.-J. Internally contracted multiconfiguration-reference configuration interaction calculations for excited states. *Theoretica chimica acta* **84**, 95-103, doi:10.1007/BF01117405 (1992).

45 Werner, H.-J., Knowles, P. J., Knizia, G., Manby, F. R. & Schütz, M. MOLPRO version 2012.1. http://www.molpro.net (2012).

46 Douglas, M. & Kroll, N. M. Quantum electrodynamical corrections to the fine structure of helium. *Ann Phys-New York* **82**, 89-155, doi:10.1016/0003-4916(74)90333-9 (1974).

47 Jansen, G. & Hess, B. A. Revision of the Douglas-Kroll transformation. *Phys Rev A* **39**, 6016-6017, doi:10.1103/PhysRevA.39.6016 (1989).

48 Balabanov, N. B. & Peterson, K. A. Systematically convergent basis sets for transition metals. I. All-electron correlation consistent

basis sets for the 3d elements Sc–Zn. *The Journal of Chemical Physics* **123**, 064107, doi:10.1063/1.1998907 (2005).
49 Dunning, T. H., Botch, B. H. & Harrison, J. F. On the orbital description of the 4s3dn+1 states of the transition metal atoms. *The Journal of Chemical Physics* **72**, 3419-3420, doi:10.1063/1.439529 (1980).
50 Botch, B. H., Dunning, T. H. & Harrison, J. F. Valence correlation in the s2dn, sdn+1, and dn+2 states of the first-row transition metal atoms. *The Journal of Chemical Physics* **75**, 3466-3476, doi:10.1063/1.442456 (1981).
51 Krishna, B. M. & Marquardt, R. Ab initio calculations of the lowest electronic states in the CuNO system. *The Journal of Chemical Physics* **136**, 244303, doi:10.1063/1.4728155 (2012).
52 Guichemerre, M., Chambaud, G. & Stoll, H. Electronic structure and spectroscopy of monohalides of metals of group I-B. *Chem Phys* **280**, 71-102, doi:10.1016/S0301-0104(02)00510-4 (2002).
53 Tulej, M. *et al.* Multiplex spectroscopy of stable and transient species in a molecular beam. *Journal of Raman Spectroscopy* **38**, 1022-1031, doi:10.1002/jrs.1735 (2007).
54 Eckbreth, A. C. BOXCARS: Crossed-beam phase-matched CARS generation in gases. *Applied Physics Letters* **32**, 421-423, doi:10.1063/1.90070 (1978).
55 Linnartz, H. Planar plasma expansions as a tool for high resolution molecular spectroscopy. *Phys Scripta* **69**, C37-C40, doi:10.1238/Physica.Regular.069a00037 (2004).
56 Birza, P. *et al.* Cw cavity ring down spectroscopy in a pulsed planar plasma expansion. *Chem Phys* **283**, 119-124, doi:10.1016/S0301-0104(02)00503-7 (2002).
57 Duncan, M. A. Invited Review Article: Laser vaporization cluster sources. *Rev Sci Instrum* **83**, 041101, doi:10.1063/1.3697599 (2012).
58 Visser, B. *et al.* Unraveling the electronic structure of transition metal dimers using resonant four-wave mixing. *Journal of Raman Spectroscopy* **47**, 425-431, doi:10.1002/jrs.4841 (2016).
59 Rohlfing, E. A., Cox, D. M. & Kaldor, A. Production and characterization of supersonic carbon cluster beams. *The Journal of Chemical Physics* **81**, 3322-3330, doi:10.1063/1.447994 (1984).

60 Grzesiak, J. *et al.* Production of rotationally cold methyl radicals in pulsed supersonic beams. *Rev Sci Instrum* **89**, 113103, doi:10.1063/1.5052017 (2018).

61 Even, U. "The Even-Lavie valve as a source for high intensity supersonic beam". *EPJ Techniques and Instrumentation* **2**, 17, doi:10.1140/epjti/s40485-015-0027-5 (2015).

62 Kruger, V. *et al.* Forward degenerate four-wave-mixing spectra of NO in the strong-field regime including polarization, line coupling, and multipole effects. II. Experiments. *Phys Rev A* **64** (2001).

63 Mulliken, R. S. Report on Notation for the Spectra of Polyatomic Molecules. *The Journal of Chemical Physics* **23**, 1997-2011, doi:10.1063/1.1740655 (1955).

64 Moore, C. E. *Tables of Spectra of Hydrogen, Carbon, Nitrogen, and Oxygen Atoms and Ions*. (CRC Press, 1993).

65 Lanczos, J. C. *Applied Analysis*. (Prentice-Hall, 1956).

66 Light, J. C. & Carrington, T. in *Advances in Chemical Physics* Vol. 114 (eds I. Prigogine & S. A. Rice) 263-310 (John Wiley & Sons, 2000).

67 Doverstål, M., Lindgren, B., Sassenberg, U. & Yu, H. The A-X system of the copper dimer studied by resonant two-photon ionization spectroscopy. *Chem Phys Lett* **192**, 283-288, doi:10.1016/0009-2614(92)85466-N (1992).

68 Witko, M. & Beckmann, H.-O. Ab initio MRD CI calculations for ground and excited states of Cu2 molecule. *Mol Phys* **47**, 945-957, doi:10.1080/00268978200100712 (1982).

69 Bishea, G. A., Pinegar, J. C. & Morse, M. D. The ground state and excited d-hole states of CuAu. *The Journal of Chemical Physics* **95**, 5630-5645, doi:10.1063/1.461638 (1991).

70 Das, K. K. & Balasubramanian, K. Spectroscopic properties of low-lying electronic states of Au2. *J Mol Spectrosc* **140**, 280-294, doi:10.1016/0022-2852(90)90141-C (1990).

71 Ikoma, H., Kasahara, S. & Kato, H. Perturbations, Intensity Anomalies, and Line Broadening of (Nak)-Na-23-K-39 Studied by Optical-Optical Double-Resonance Polarization Spectroscopy. *Mol Phys* **85**, 799-820, doi:10.1080/00268979500101501 (1995).

72 Murdock, D., Burns, L. A. & Vaccaro, P. H. Dissection of Rovibronic Structure by Polarization-Resolved Two-Color Resonant Four-Wave Mixing Spectroscopy. *J Phys Chem A* **113**, 13184-13198, doi:10.1021/jp903970d (2009).

73 Visser, B. *et al.* Identification of a new low energy 1_u state in dicopper with resonant four-wave mixing. *J Chem Phys* **147**, 214308, doi:10.1063/1.5006107 (2017).
74 Farrow, R. L., Rakestraw, D. J. & Dreier, T. Investigation of the Dependence of Degenerate 4-Wave-Mixing Line-Intensities on Transition Dipole-Moment. *J Opt Soc Am B* **9**, 1770-1777, doi:10.1364/Josab.9.001770 (1992).
75 Beck, M. *et al.* Rovibrational Characterization of High-Lying Electronic States of Cu_2 by Double-Resonant Nonlinear Spectroscopy. *J Phys Chem A* **121**, 8448-8452, doi:10.1021/acs.jpca.7b09838 (2017).
76 Spain, E. M. & Morse, M. D. Ligand-Field Theory Applied to Diatomic Transition-Metals - Results for the D9ad9b-Sigma-2 States of Ni2, the D9nid10cu-Sigma-2 States of Nicu, and the D8ni(3f)D10cu-Sigma-2-Sigma-Asterisk-1 Excited-States of Nicu. *J Chem Phys* **97**, 4641-4660, doi:Doi 10.1063/1.463867 (1992).
77 Muller, T. Large-Scale Parallel Uncontracted Multireference-Averaged Quadratic Coupled Cluster: The Ground State of the Chromium Dimer Revisited. *J Phys Chem A* **113**, 12729-12740, doi:10.1021/jp905254u (2009).
78 Edgecombe, K. E. & Becke, A. D. Cr-2 in Density-Functional Theory - Approximate Spin Projection. *Chem Phys Lett* **244**, 427-432, doi:10.1016/0009-2614(95)00945-Z (1995).
79 Messerschmidt, A. in *Comprehensive Natural Products II* (eds Hung-Wen Liu & Lew Mander) 489-545 (Elsevier, 2010).
80 Ravi, M., Ranocchiari, M. & van Bokhoven, J. A. The Direct Catalytic Oxidation of Methane to Methanol-A Critical Assessment. *Angew Chem Int Edit* **56**, 16464-16483, doi:10.1002/anie.201702550 (2017).
81 Bender, D. *UV-Laserspektroskopie gestörter Zustände des Bariumoxids*, Hannover, (1985).
82 Bender, D., Schaefer, S. H. & Tiemann, E. Laser spectroscopy of perturbed states of BaO in the region above 32 000 cm−1. *J Mol Spectrosc* **116**, 286-314, doi:10.1016/0022-2852(86)90128-1 (1986).
83 Pashov, A., Kowalczyk, P. & Jastrzebski, W. Absolute vibrational numbering from isotope shifts in fragmentary spectroscopic data. *J Mol Spectrosc* **347**, 48-55, doi:10.1016/j.jms.2018.03.016 (2018).

9 Acknowledgement

The work presented in this thesis would never have been possible without strong support by others.

First and foremost, I want to express my gratitude to Dr. Peter P. Radi and Prof. Dr. Jeroen A. van Bokhoven, whose joined project gave me the possibility to carry out all these exciting experiments described in the thesis. I greatly appreciate their forbearance in regards to my actions, which often differed from their expectations. Working with them at Paul Scherrer Institute (PSI) was a unique experience to which I always look back with good memorys.

I also want to thank all people that were contributing in carrying out these studies at PSI:
Dr. Bradley Visser, with whom I shared office and experiment for two years. It was a great time in any respect.
Dr. Peter Bornhauser, who was contributing to analysis and interpretation of the experimental spectra.
Dr. Gregor Knopp, who often gave valuable hints on optics and was an enrichment when discussing the findings.

For his contributions to the theoretical aspects of our work and some really inspiring discussions, I want to thank Prof. Dr. Roberto Marquardt (Université de Strasbourg).

I also want to thank the members of all groups, I was working in during my years at PSI (Molecular Dynamics Group, Alvra Group), but also the joined PSI/ETH Zürich van Bokhoven Group. It really was a great time.

Further thanks goes to my co-examiner Prof. Dr. Hans Jakob Wörner for reviewing this thesis.

Besides science, I want to also thank my family and especially my wife Lea, which had to go through so many tasks alone, while I was busy with science. Without their support, I could not have spent so much time on science.

Last but not least, for financial support of our work, including funding for my position at PSI, I want to thank the Swiss National Science Foundation (projects #200021_1531701 and #200020_1754901).

10 Appendix

10.1 Personal publication list

10.1.1 Publications related to this thesis

1. *M. Beck*, B. Visser, P. Bornhauser, G. Knopp, J. A. van Bokhoven, P. P. Radi, "Spectroscopic disentanglement of the quantum states of highly excited Cu_2", Nat. Commun., 2019, 10, 3270.
2. B. Visser, *M. Beck*, P. Bornhauser, G. Knopp, J. A. van Bokhoven, P. Radi, C. Gourlaouen, R. Marquardt, "New experimental and theoretical assessment of the dissociation energy of C_2", Mol. Phys., 2019, 117 (13), pp. 1645-1652.
3. B. Visser, *M. Beck*, P. Bornhauser, G. Knopp, J. A. van Bokhoven, R. Marquardt, C. Gourlaouen, and P. P. Radi, "Identification of a new low energy 1_u state in dicopper with resonant four-wave mixing", J. Chem. Phys., 2017, 147, 214308.
4. *M. Beck*, B. Visser, P. Bornhauser, G. Knopp, J. A. van Bokhoven, P. P. Radi, "Rovibrational Characterization of High Lying Electronic States of Cu_2 by Double-Resonant Non-Linear Spectroscopy", J. Phys. Chem. A, 2017, 121 (44), pp 8448–8452.
5. P. Bornhauser, B. Visser, *M. Beck*, G. Knopp, J. A. van Bokhoven, R. Marquardt, P. P. Radi, "Experimental and theoretical investigation of the vibrational band structure of the $1^5\Pi_u$–$1^5\Pi_g$ high-spin system of C_2", J. Chem. Phys., 2017, 146, 114309.
6. B. Visser, *M. Beck*, P. Bornhauser, G. Knopp, T. Gerber, R. Abela, J.A. van Bokhoven, P.P. Radi, "Unraveling the electronic structure of transition metal dimers using resonant four-wave mixing", J. Raman Spectrosc., 2016, 47, 425-431.
7. P. Bornhauser, R. Marquardt, C. Gourlaouen, G. Knopp, M. Beck, T. Gerber, J.A. van Bokhoven, P. Radi, "Perturbation-facilitated detection of the first quintet-quintet band in C_2", J. Chem. Phys., 2015, 142, 094313.

10.1.2 Other publications

8. C. Svetina, R. Mankowsky, G. Knopp, F. Koch, G. Seniutinas, B. Rösner, A. Kubec, M. Lebugle, I. Mochi, *M. Beck*, C. Cirelli, J. Krempasky, C. Pradervand, J. Rouxel, G. F. Mancini, S. Zerdane, B. Pedrini, V. Esposito, G. Ingold, U. Wagner, U. Flechsig, R. Follath, M. Chergui, C. Milne, H. T. Lemke, C. David, P. Beaud, "Towards X-ray transient grating spectroscopy", Opt. Lett., 2019, 44, 574-577.
9. A. Dollinger, L. Stolch, Y. Luo, *M. Beck*, C. H. Strobel, M. Hagner, S. Dilger, M. Bein, S. Polarz, G. F. Gantefoer, Y. D. Kim, S. Proch, "Size-Selected Gold Clusters on Porous Titania as the most "Gold-Efficient" Heterogeneous Catalysts", Phys. Chem. Chem. Phys., 2014, 16, 11017-11023.
10. Y. Luo, H. O. Seo, *M. Beck*, S. Proch, Y. D. Kim, G. Ganteför, "Parallel deposition of size-selected clusters: a novel technique for studying size-selectivity on the atomic scale", Phys. Chem. Chem. Phys., 2014, 16, 9233-9237.

10.1.3 Post-deadline publications

Prospective work of Martin Beck can be found using his ORCID iD:

https://orcid.org/0000-0002-4475-3587

10.2 Methods used to prepare chapter 5.3

Declaration: this chapter reproduces a large portion of the methods section of [M. Beck, P. Bornhauser, B. Visser, G. Knopp, J. A. van Bokhoven, P. P. Radi, Spectroscopic disentanglement of the quantum states of highly excited Cu_2, Nat. Commun., 2019, 10, 3270.]. The author wrote the underlying manuscript based on experimental work equally contributed by Bradley Visser and the author. Within this work, the classification of the *G* states and the calculations of the Frank-Condon overlaps were contributed by P. Bornhauser and P. P. Radi.

10.2.1 Equilibrium constants of the J state

Utilizing the well-established relationships between the molecular constants of different isotopologues[3], we merged the deperturbed constants of both isotopologues before fitting equilibrium constants. While for most constants, the knowledge of the isotopes' masses is sufficient, the determination of the electronic term T_e depends on the knowledge of the ground state zero-point energy, as all experimental data is referenced

against it. Based on the Dunham coefficients reported by Ram *et al.*[17], we calculated the zero-point contributions for $^{63}Cu_2$ (132.9711(19) cm^{-1}) and $^{63}Cu^{65}Cu$ (131.9360(18) cm^{-1}). After merging the isotopologues, T_e, ω_e and $\omega_e x_e$ were fitted to the T_v values and B_e, and α_e were fitted to the B_v values. The equilibrium value for the internuclear distance r_e was then calculated based on B_e and the isotopic masses. To stay consistent within literature, Table 9 presents the equilibrium constants in terms of the lightest isotopologue $^{63}Cu_2$. However, by using the same relationships, the constants for any isotopologue can be derived. For $^{63}Cu^{65}Cu$, for example, one obtains slightly lower values for ω_e (287.67(17) cm^{-1}), $\omega_e x_e$ (1.054(57) cm^{-1}), B_e (0.114276(11) cm^{-1}) and α_e (0.0008913(75) cm^{-1}).

10.2.2 Deperturbation and classification of the G_{67} state

The $G_{xx} \sim$ J perturbation strength listed in Table 8 were obtained by assuming a homogeneous, *J* independent perturbation. Trials performed using a heterogeneous perturbation yielded significantly larger residuals for the $G_{67} \sim$ J (v = 2) system. A graphical perturbation analysis has been proposed by Bender[81,82] and is shown in Figure 24. The effective rotational constants, B_{eff}, of the $G_{67} \sim$ J (v = 2) system vs. *J* are plotted. The crossing of the traces occurs at J<0 and corroborates the homogeneous perturbation mechanism. Since the symmetry of the bright state J is certainly an Ω=0_u^+ state, a homogeneous perturbation determines the perturber G_{67} and the other members of the G_{xx} progression as 0_u^+ states. For comparison, a homogeneous perturbation model is applied for the deperturbation of the *L*1, *M*1, *N*1 and *O*1 perturber states. A definitive assignment, however, requires more detailed investigations.

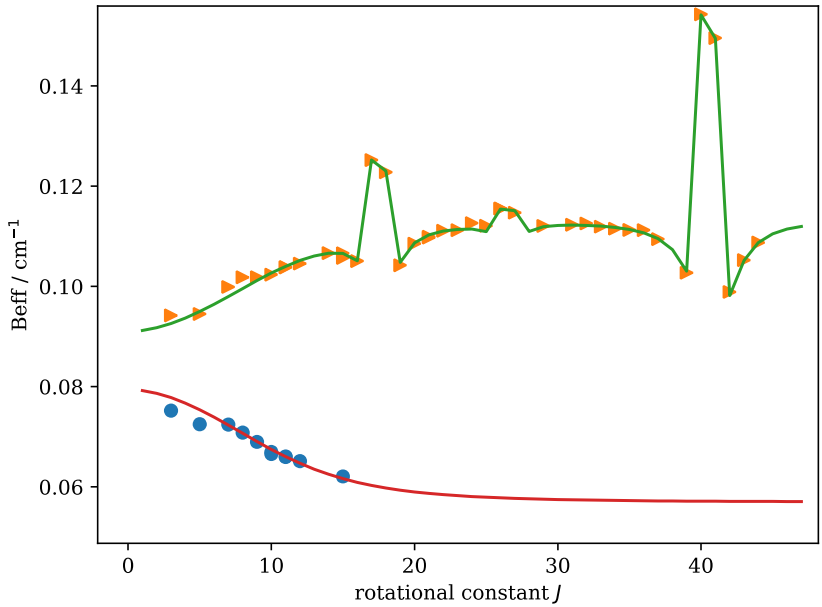

Figure 24: Homogeneous perturbation of the J (v=2) ~ G_{67} system
The effective rotational constants, B_{eff} vs. J are shown for J (v = 2) and G_{67} (upper and lower trace, respectively). The solid lines are obtained from the deperturbation analysis of the system. A crossing of the two levels at J < 0 is indicative for a homogeneous perturbation.[81,82] Perturbations of the J (v = 2) level with N1, M1 and G_{68} appear in addition at approximately J = 18, 28, and 40, respectively.

10.2.3 Vibrational quantum numbers of the G_{xx} states

The deperturbed molecular constants in Table 8 allowed determination of the absolute vibrational numbering. The presumption that the vibrational progression of the G_{62} to G_{68} levels belong to the G state was supported by a good qualitative match between their spacing and the expected spacing extrapolating from the reported levels from Powers *et al.*[14]. Following the established approach of determining the vibrational level v based on the isotope shift[3], we fitted our values to a Dunham expansion, which led to an absolute value of about v = 62 for the lowest of these levels. The initial approach in doing so was to use an equilibrium term energy of

T_e = 30695 cm^{-1}. This value was derived from the levels reported by Powers *et al.*, but taking into account a correction of the numbering assignments ($v_N \rightarrow v_{N-1}$) already proposed by Rohlfing *et al.*[15]. However, defining T_e as a free fit parameter, the obtained value $v = 62$ barely changed (e.g., 62.28 → 62.33). This is in good agreement with recent work by Pashov *et al.* [83], in which they demonstrate the establishment of absolute vibrational numbering based on four term energies in one isotopologue and one term energy in another. Also when using their method, which was applied after simulating unperturbed bands using PGOPHER, G_{62} was also assigned to $v = 62$. Nevertheless, one should take these values with caution. We have already demonstrated that the low-lying electronic states of the copper dimer can be only explained by assuming spin–orbit states given by Hund's case (c) coupling[73]. In the computational part of that work, only the potential curves of states corresponding to separated atom limits with only a single excitation were fully covered. Therefore, only two covalently bound 0_u^+ states interact with the 0_u^+ ion-pair ground state to bring forth the A, the B, and the G states. Taking a look at the experimentally derived potential energy curves of Cu_2, which were illustrated, e.g., in a book chapter by Morse[1] (see Figure 2), it becomes obvious that the separated atom limits with double excitation cannot be ignored, and further 0+u states originate from the $^2D + {}^2D$ atomic limits. As these states also contribute avoided crossings and, in addition, $v = 0$ of the G state was never observed, it is still too early to decide if the methods used above are applicable for this system.

10.2.4 Interpolation of missing vibrational origins

Within Table 8, only the numbers with a specified standard deviation are directly derived from experimental data. The missing T_v values of G_{xx} states were filled based on the fitted Dunham expansion that was also used to determine the absolute vibrational levels. For the perturbations, the strengths were similar whenever we had experimental access to both

isotopologues. Therefore, we presumed a similarity also when only one isotopologue was measured.

10.2.5 Franck-Condon overlaps in the $G_{xx} \sim$ J systems

Figure 25 shows the RKR potentials of the J and *G* states, which were constructed by performing Dunham fits to the molecular constants listed in the Table 8. The wave functions and the overlap integrals are then obtained by solving the radial Schrödinger equation. A ratio of 1 : 3 : 6 is computed for the overlaps between $G_{62}\sim J(v = 0) \approx G_{63}\sim J(v = 0)$: $G_{64}\sim J(v = 1) \approx G_{65}\sim J(v = 1) \approx G_{66}\sim J(v = 1)$: $G_{67}\sim J(v = 2) \approx G_{68}\sim J(v = 2)$, which is in good agreement with the values for the homogeneous perturbation strength between the G_{xx} and J states deduced from the experiment and shown in Table 8.

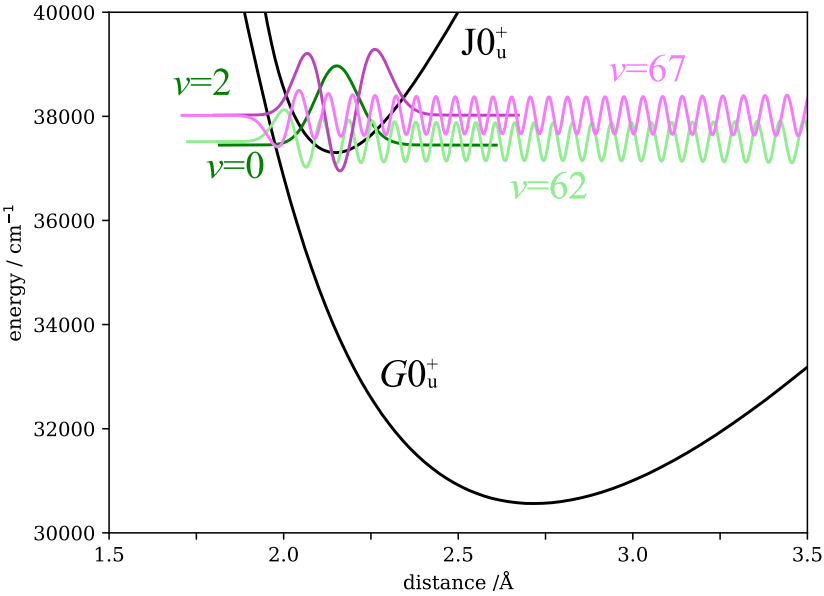

Figure 25: Vibrational Overlap
The wave functions of the near resonant G62 and J (v = 0) states shown in magenta and the G67 and J (v = 2) shown in turquoise. The overlap integrals are very favorable in both cases.

10.2.6 Simulation of perturbed bands

To generate Figure 20, we used PGOPHER to simulate the (0-0) J-X band of Cu_2 based on the constants and interactions reported in Table 8. For the spectrum (Figure 20a), a rotational temperature of 50 K was chosen, in order to achieve a close resemblance of the intensity distribution observed in our experiment. The abundance of the isotopologues was based on natural abundance. As the different statistical weight of symmetrical and asymmetrical rotational levels (3 and 5) in the homonuclear isotopologue is taken into account in the simulation, an average statistical weight of 4 was chosen for all levels of the heteronuclear isotopologue to match the average intensity. In the Fortrat diagram, straight lines between the points of each branch were added as a guide to the eye. To emphasize the perturbations that yield some obvious spectral features, the corresponding regions of the Fortrat diagram were copied into the simulated spectra.

10.2.7 Generation of Figure 21

Parsing the raw list of all assigned lines, the corresponding raw spectra were loaded and normalized. They were then added to the scalable vector graphics (SVG) file, using the rotational quantum number in the ground state as a vertical offset. Therefore, the peak heights do not scale with the absolute intensity, when comparing different scans. For some rotational levels, different lines were used to select the rotational quantum state. Owing to the different overlaps associated with these lines, only the peaks that belong to the targeted rotational state reproduce. In a second round, windows around the assigned line positions were selected from each raw spectrum. These were redrawn with a colorized background to highlight the assigned peak. To achieve a clearer presentation, a few peaks were manually rescaled and the colorized ranges were slightly readjusted when arranging and formatting the final Figure 21a. For the corresponding level diagram in Figure 21b, we used the simulation based on the fitted molecular constants. At the scale employed, this does not affect the position of the data points,

but improves clarity by extrapolating points missing within the experimental dataset. To further clarify the level repulsion, the levels were plotted as relative wavenumber $\tilde{\nu}_{\text{relative}} = \tilde{\nu}_{\text{absolute}} - 38{,}000\text{cm}^{-1} - B_{O1}J(J+1)$ where B_{O1} is the rotational constant of the $O1$ state as reported in Table 4. Therefore, the relative values are referenced against an unperturbed, harmonic version of $O1$.

10.2.8 Details on the excitation scans

When recording the spectrum in Figure 22a, some stray light of the UV pump laser passed the spectrometer off-axis. Therefore, we started integration 20 ns after the maximum of the pump pulse to ensure that also the electrical response of the photomultiplier had concluded. In contrast, the strong, and therefore short-lived, blue fluorescence shown in Figure 22b,c was integrated over the complete pulse. This timing difference is responsible for the complete disappearance of the G_{62}-related lines in Figure 22.

10.2.9 Generation of Figure 23

This overview figure was created by reusing the code used for Figure 21, but applying it on the full line list. As this inevitably produces overlapping spectra, colored lines (instead of colored fills) were used to indicate the assigned lines. While the full spectral raw data was exposed to the Matplotlib library, some data points that did not contribute to significant changes in the shape of the curve were dropped. Therefore, zooming into the vector graphic will not always show the full details of the background noise. The total absence of background in some of the excitation scans allowed to still obtain clear peaks even when averaging at event rates of less than one event per laser pulse. Because of the normalization of the plotted raw spectra, these features can be invisible, if there are strong lines in the same spectrum. An extreme example of this are the high rotational levels of the G_{65} state in the $^{63}Cu^{65}Cu$ isotopologue. There, the background is plotted as a completely

flat line and the colored peaks are just visible, because the amplitude was manually increased when composing the final depiction.

10.3 Line list underlying Chapter 4

Table 11: Rotationally resolved transitions from the vibronic ground state (X) into the two lowest vibrational levels of the A' states of $^{63}Cu_2$ and $^{63}Cu^{65}Cu$. Line positions were fitted for clearly assignable observations. Overlapping and distorted features were not assigned. The residuals presented are from fitting the molecular constants shown in Table 4. The probe column specifies the lines used for double-resonant labeling in the (1,0) B-X band. The corresponding wavelengths were calculated based on the constants reported by Ram *et al.*[17] Intensity fluctuations occur owing to pulse to pulse variations of the cluster source and the spectroscopy lasers. As a consequence small deviations occur for the fitted line positions, even on re-measured identical lines.

Transition	Observed	Residuals	Probe	Transition	Observed	Residuals	Probe
$^{63}Cu_2$: (0-0) A'–X							
pP21(29)	20092.191	0.003	P(27)	qQ21(12)	20100.204	0.004	P(12)
pP21(20)	20095.271	0.005	P(17)	qQ21(10)	20100.313	-0.011	P(5)
pP21(17)	20096.203	0.000	P(17)	qQ21(10)	20100.329	0.005	P(5)
pP21(17)	20096.209	0.006	P(17)	qQ21(9)	20100.377	0.000	P(9)
pP21(16)	20096.516	0.010	P(16)	qQ21(8)	20100.429	0.003	R(21)
pP21(15)	20096.803	0.001	P(15)	qQ21(7)	20100.466	-0.004	R(19)
pP21(14)	20097.103	0.009	P(14)	qQ21(6)	20100.492	-0.015	R(18)
pP21(13)	20097.378	-0.003	P(13)	qQ21(5)	20100.524	-0.015	P(5)
pP21(13)	20097.393	0.013	P(13)	qQ21(3)	20100.581	-0.007	R(15)
qQ21(33)	20097.663	-0.015	P(33)	rR21(3)	20101.424	-0.011	R(15)
pP21(12)	20097.665	0.004	P(12)	rR21(5)	20101.805	-0.004	P(5)
qQ21(31)	20097.996	-0.013	P(29)	rR21(6)	20101.986	-0.002	R(18)
pP21(10)	20098.206	-0.003	P(5)	rR21(7)	20102.146	-0.016	R(19)
qQ21(29)	20098.328	0.006	P(27)	rR21(8)	20102.32	-0.009	R(21)
pP21(9)	20098.471	-0.003	P(9)	rR21(9)	20102.493	0.000	P(9)
pP21(8)	20098.728	-0.006	R(21)	qQ21(12)	20100.204	0.004	P(12)
pP21(8)	20098.728	-0.006	R(21)	rR21(10)	20102.649	-0.002	P(5)
pP21(6)	20099.222	-0.015	R(18)	rR21(12)	20102.956	0.006	P(12)

Transition	Observed	Residuals	Probe	Transition	Observed	Residuals	Probe
pP21(6)	20099.222	-0.015	R(18)	rR21(12)	20102.956	0.006	P(12)
pP21(5)	20099.472	-0.010	P(5)	rR21(13)	20103.092	0.000	P(13)
qQ21(19)	20099.607	0.004	P(19)	rR21(13)	20103.096	0.004	P(13)
qQ21(17)	20099.808	0.009	P(17)	rR21(14)	20103.231	0.003	P(14)
qQ21(16)	20099.899	0.009	P(16)	rR21(15)	20103.367	0.008	P(15)
qQ21(15)	20099.974	-0.001	P(15)	rR21(16)	20103.497	0.011	P(16)
qQ21(14)	20100.06	0.005	P(14)	rR21(17)	20103.614	0.007	P(17)
qQ21(13)	20100.141	0.010	P(13)	rR21(19)	20103.845	0.012	P(19)
qQ21(13)	20100.145	0.015	P(13)	rR21(33)	20104.86	-0.009	P(33)
$^{63}Cu_2$: (1-0) A'–X							
pP21(19)	20328.410	0.006	R(19)	qQ21(9)	20333.391	0.009	R(13)
pP21(18)	20328.733	-0.010	R(17)	qQ21(7)	20333.500	0.001	R(13)
pP21(17)	20329.081	0.006	R(17)	qQ21(7)	20333.502	0.003	R(19)
pP21(17)	20329.082	0.007	P(17)	rR21(5)	20334.832	-0.016	R(11)
pP21(16)	20329.396	-0.004	P(16)	rR21(7)	20335.182	0.002	R(19)
pP21(15)	20329.707	-0.012	P(11)	rR21(7)	20335.185	0.005	R(13)
pP21(15)	20329.722	0.003	R(15)	rR21(8)	20335.357	0.022	R(13)
pP21(14)	20330.023	-0.008	P(14)	rR21(9)	20335.476	-0.007	R(11)
pP21(11)	20330.936	0.008	R(13)	rR21(9)	20335.479	-0.004	R(13)
pP21(9)	20331.467	-0.025	R(11)	rR21(9)	20335.483	0.000	R(11)
pP21(9)	20331.478	-0.014	R(11)	rR21(9)	20335.488	0.005	P(9)
pP21(9)	20331.493	0.001	P(9)	rR21(9)	20335.494	0.011	R(11)
pP21(9)	20331.498	0.006	R(13)	rR21(10)	20335.619	-0.006	R(13)
pP21(7)	20332.025	-0.004	R(19)	rR21(11)	20335.751	-0.008	R(13)
qQ21(19)	20332.399	0.004	R(19)	rR21(11)	20335.751	-0.008	R(11)
qQ21(18)	20332.535	0.012	P(15)	rR21(13)	20335.996	-0.013	R(11)
pP21(5)	20332.547	0.009	R(11)	rR21(14)	20336.121	-0.002	P(14)
qQ21(18)	20332.560	0.036	R(17)	rR21(15)	20336.223	-0.008	R(13)
qQ21(17)	20332.656	0.010	R(17)	rR21(15)	20336.230	-0.001	R(15)
qQ21(17)	20332.656	0.010	P(17)	rR21(15)	20336.233	0.002	P(11)
qQ21(16)	20332.766	0.005	P(16)	rR21(16)	20336.337	0.005	P(11)

Transition	Observed	Residuals	Probe	Transition	Observed	Residuals	Probe
qQ21(15)	20332.877	0.006	R(15)	rR21(17)	20336.413	-0.013	P(17)
qQ21(14)	20332.989	0.017	P(14)	rR21(17)	20336.415	-0.012	R(17)
qQ21(11)	20333.249	0.010	R(13)	rR21(18)	20336.501	-0.014	R(17)
qQ21(9)	20333.368	-0.014	R(11)	rR21(18)	20336.510	-0.005	P(15)
qQ21(9)	20333.382	0.000	R(11)	rR21(19)	20336.576	-0.020	R(19)
qQ21(9)	20333.390	0.008	P(9)				
$^{63}Cu^{65}Cu$: (0-0) A'–X							
pP21(31)	20091.677	-0.021	P(31)	qQ21(13)	20100.238	0.016	P(13)
pP21(29)	20092.411	-0.009	P(29)	qQ21(12)	20100.303	0.013	P(12)
pP21(20)	20095.438	-0.001	P(20)	qQ21(11)	20100.357	0.005	P(11)
pP21(19)	20095.745	-0.005	P(19)	qQ21(10)	20100.405	-0.006	P(14)
pP21(19)	20095.762	0.011	P(19)	qQ21(10)	20100.412	0.001	P(14)
pP21(18)	20096.059	0.002	P(18)	qQ21(9)	20100.458	-0.005	P(13)
pP21(17)	20096.366	0.007	P(17)	qQ21(9)	20100.465	0.002	P(13)
pP21(16)	20096.658	0.003	P(19)	qQ21(9)	20100.465	0.003	P(13)
pP21(15)	20096.960	0.013	P(15)	qQ21(8)	20100.514	0.004	P(8)
pP21(14)	20097.231	-0.002	P(14)	qQ21(7)	20100.550	-0.002	P(7)
pP21(13)	20097.514	-0.001	P(13)	qQ21(6)	20100.588	-0.001	R(25)
pP21(13)	20097.516	0.002	P(13)	qQ21(5)	20100.611	-0.009	P(5)
pP21(12)	20097.789	-0.001	P(12)	qQ21(5)	20100.627	0.006	P(5)
pP21(11)	20098.053	-0.009	P(11)	qQ21(4)	20100.643	-0.004	P(9)
qQ21(31)	20098.140	-0.016	P(31)	qQ21(3)	20100.667	-0.001	R(22)
pP21(10)	20098.322	-0.005	P(14)	rR21(3)	20101.490	-0.011	R(22)
qQ21(29)	20098.446	-0.015	P(29)	rR21(4)	20101.689	0.001	P(9)
pP21(9)	20098.596	0.008	P(13)	rR21(5)	20101.855	-0.016	P(5)
pP21(9)	20098.597	0.009	P(13)	rR21(5)	20101.864	-0.006	P(5)
qQ21(27)	20098.756	0.007	P(27)	rR21(7)	20102.203	-0.015	P(7)
pP21(8)	20098.846	0.003	P(8)	rR21(8)	20102.379	-0.006	P(8)
pP21(7)	20099.083	-0.011	P(7)	rR21(9)	20102.543	-0.003	P(13)
pP21(6)	20099.330	-0.009	R(25)	rR21(9)	20102.548	0.002	P(13)
pP21(6)	20099.330	-0.009	R(25)	rR21(9)	20102.550	0.004	P(13)

Transition	Observed	Residuals	Probe	Transition	Observed	Residuals	Probe
qQ21(21)	20099.509	0.012	P(21)	rR21(10)	20102.688	-0.014	P(14)
pP21(5)	20099.564	-0.015	P(5)	rR21(10)	20102.697	-0.005	P(14)
pP21(5)	20099.572	-0.007	P(5)	rR21(11)	20102.852	0.000	P(11)
qQ21(20)	20099.616	0.011	P(20)	rR21(12)	20102.995	-0.004	P(12)
qQ21(19)	20099.717	0.009	P(19)	rR21(13)	20103.135	-0.003	P(13)
qQ21(19)	20099.723	0.014	P(19)	rR21(14)	20103.277	0.003	P(14)
qQ21(18)	20099.821	0.014	P(18)	rR21(15)	20103.404	0.000	P(15)
pP21(4)	20099.823	0.009	P(9)	rR21(16)	20103.538	0.008	P(19)
qQ21(17)	20099.907	0.007	P(17)	rR21(17)	20103.656	0.006	P(17)
qQ21(16)	20099.997	0.009	P(19)	rR21(18)	20103.768	0.003	P(18)
pP21(3)	20100.035	-0.008	R(22)	rR21(19)	20103.887	0.012	P(19)
qQ21(15)	20100.071	0.000	P(15)	rR21(20)	20103.994	0.013	P(20)
qQ21(14)	20100.150	0.001	P(14)	rR21(21)	20104.082	0.001	P(21)
qQ21(13)	20100.226	0.004	P(13)				
^{63}Cu^{65}Cu: (1-0) A'–X							
pP21(13)	20328.678	-0.013	R(13)	rR21(8)	20333.639	0.024	R(13)
pP21(12)	20328.991	0.004	R(13)	rR21(9)	20333.759	-0.001	R(11)
pP21(12)	20328.995	0.008	R(13)	rR21(9)	20333.760	0.000	R(13)
qQ21(29)	20329.070	0.014	P(14)	rR21(9)	20333.767	0.006	R(11)
pP21(11)	20329.274	-0.002	R(13)	rR21(10)	20333.895	-0.004	R(11)
pP21(10)	20329.552	-0.006	P(14)	rR21(10)	20333.898	-0.001	R(11)
pP21(10)	20329.565	0.007	R(13)	rR21(10)	20333.901	0.003	R(13)
pP21(9)	20329.814	-0.019	R(13)	rR21(11)	20334.019	-0.011	R(11)
qQ21(15)	20331.195	0.016	R(15)	rR21(11)	20334.025	-0.005	R(13)
qQ21(13)	20331.388	0.010	R(11)	rR21(11)	20334.038	0.009	R(13)
qQ21(13)	20331.399	0.021	R(13)	rR21(11)	20334.046	0.017	R(11)
qQ21(12)	20331.459	-0.009	R(13)	rR21(12)	20334.141	-0.013	R(11)
qQ21(12)	20331.487	0.020	R(13)	rR21(12)	20334.142	-0.012	R(13)
qQ21(11)	20331.547	-0.002	R(13)	rR21(12)	20334.146	-0.008	R(13)
qQ21(9)	20331.678	-0.015	R(13)	rR21(13)	20334.250	-0.022	R(11)

Transition	Observed	Residuals	Probe	Transition	Observed	Residuals	Probe
qQ21(9)	20331.692	-0.001	R(11)	rR21(13)	20334.272	0.001	R(13)
qQ21(9)	20331.698	0.004	R(11)	rR21(15)	20334.486	-0.001	R(15)
qQ21(8)	20331.749	-0.007	R(11)	rR21(15)	20334.486	-0.001	R(15)
rR21(7)	20333.468	0.004	R(13)	rR21(29)	20335.244	-0.013	P(14)

10.4 Line list underlying Chapter 5.2

Table 12: Rotationally resolved transitions from the vibronic ground state (X) into the two lowest vibrational levels of the J state of $^{63}Cu_2$. Line positions were fitted for clearly assignable observations. Overlapping and distorted features were not assigned. The residuals presented are from fitting the molecular constants shown in Table 4. The probe column specifies the lines used for double-resonant labeling in the (1,0) B-X band. The corresponding wavelengths were calculated based on the constants reported by Ram *et al.*[17] Intensity fluctuations occur owing to pulse to pulse variations of the cluster source and the spectroscopy lasers. As a consequence small deviations occur for the fitted line positions, even on re-measured identical lines.

Transition	Observed	Residuals	Probe	Transition	Observed	Residuals	Probe
(0,0) J-X							
P(15)	37446.91	-0.07	P(15)	R(9)	37451.67	-0.02	P(9)
P(12)	37447.05	-0.03	P(12)	R(10)	37452.08	0.02	P(10)
P(20)	37447.05	-0.05	R(20)	R(11)	37452.52	0.06	P(11)
P(19)	37447.06	0.02	P(19)	R(12)	37452.80	-0.05	P(12)
P(19)	37447.08	0.03	P(19)	R(13)	37453.30	0.03	P(13)
P(20)	37447.10	0.00	P(20)	R(13)	37453.32	0.05	P(13)
P(21)	37447.13	-0.04	P(21)	R(14)	37453.75	0.05	P(14)
P(21)	37447.18	0.01	P(21)	R(15)	37454.14	0.00	P(15)
P(11)	37447.18	0.04	R(11)	R(15)	37454.18	0.04	P(15)
P(9)	37447.25	-0.05	P(9)	R(16)	37454.62	0.02	P(16)
P(22)	37447.28	0.03	P(22)	R(17)	37455.04	-0.03	P(17)
P(10)	37447.30	0.08	P(10)	R(17)	37455.08	0.01	P(17)
P(8)	37447.35	-0.06	P(8)	R(19)	37456.07	0.01	P(19)
P(23)	37447.37	0.02	P(23)	R(20)	37456.53	-0.05	R(20)
P(24)	37447.48	0.02	P(24)	R(20)	37456.57	0.00	P(20)
P(25)	37447.58	0.00	P(25)	R(20)	37456.58	0.00	P(20)
R(3)	37449.73	-0.03	P(3)	R(21)	37457.09	-0.01	P(21)
R(5)	37450.28	-0.06	P(5)	R(21)	37457.14	0.04	P(21)
R(7)	37451.01	0.02	P(7)	R(22)	37457.57	-0.07	R(22)
R(7)	37451.06	0.07	P(7)	R(22)	37457.65	0.01	P(22)
R(8)	37451.28	-0.05	P(8)	R(23)	37458.20	0.00	P(23)

Transition	Observed	Residuals	Probe	Transition	Observed	Residuals	Probe
(1,0) J-X							
P(20)	37734.68	-0.07	P(20)	R(8)	37739.35	0.00	P(8)
P(18)	37734.74	-0.02	P(18)	R(9)	37739.71	0.02	P(9)
P(17)	37734.77	0.00	P(17)	R(10)	37739.97	-0.06	P(10)
P(19)	37734.78	0.03	P(19)	R(12)	37740.76	0.00	P(12)
P(22)	37734.80	0.00	P(22)	R(13)	37741.15	0.01	P(13)
P(21)	37734.82	0.05	P(21)	R(14)	37741.50	-0.03	P(14)
P(16)	37734.83	0.03	P(16)	R(14)	37741.50	-0.03	P(14)
P(14)	37734.85	-0.05	P(14)	R(15)	37741.96	0.03	P(15)
P(14)	37734.88	-0.03	P(14)	R(16)	37742.37	0.02	P(16)
P(15)	37734.90	0.05	P(15)	R(17)	37742.74	-0.03	P(17)
P(24)	37734.94	0.05	P(24)	R(18)	37743.19	-0.01	P(18)
P(25)	37734.98	0.03	P(25)	R(19)	37743.68	0.02	P(19)
P(13)	37735.01	0.04	P(13)	R(20)	37744.04	-0.08	P(20)
P(12)	37735.01	-0.03	P(12)	R(21)	37744.66	0.07	P(21)
P(26)	37735.06	0.03	P(26)	R(22)	37745.06	-0.02	P(22)
P(27)	37735.15	0.03	P(27)	R(24)	37746.07	-0.02	P(24)
P(29)	37735.34	0.01	P(29)	R(25)	37746.63	0.02	P(25)
P(9)	37735.38	0.03	P(9)	R(26)	37747.18	0.04	P(26)
P(30)	37735.45	-0.01	P(30)	R(27)	37747.67	-0.02	P(27)
P(31)	37735.63	0.03	R(31)	R(28)	37748.26	0.02	P(28)
P(7)	37735.64	0.03	P(7)	R(29)	37748.75	-0.06	R(29)
P(5)	37735.88	-0.04	P(5)	R(29)	37748.78	-0.03	P(29)
R(5)	37738.42	-0.01	P(5)	R(30)	37749.38	-0.01	P(30)
R(7)	37739.04	0.00	P(7)	R(31)	37749.94	-0.05	R(31)

Table 13: Rotationally resolved transitions from the vibronic ground state (X) into two vibrational levels of the I state of $^{63}Cu_2$. Line positions were fitted for clearly assignable observations. As the vibrational ground state of I is not known, vibrational levels are labelled relative to a level "x" defined by Powers *et al.*[14]. The residuals presented are from fitting the molecular constants shown in Table 1. The probe column specifies the lines used for double-resonant labeling in the (1-0) B-X band. The corresponding wavelengths were calculated based on the constants reported by Ram *et al.*[17] Intensity fluctuations occur owing to pulse to pulse variations of the cluster source and the spectroscopy lasers. As a consequence small deviations occur for the fitted line positions, even on re-measured identical lines.

Transition	Observed	Residuals	Probe	Transition	Observed	Residuals	Probe
("*x*+1",0) I-X							
P(18)	37408.11	0.01	P(18)	Q(10)	37411.20	-0.01	P(10)
P(17)	37408.20	0.03	P(17)	Q(11)	37411.32	0.01	P(11)
P(16)	37408.28	0.01	P(16)	Q(12)	37411.38	-0.02	P(12)
P(15)	37408.36	-0.01	P(15)	Q(13)	37411.51	0.00	P(13)
P(15)	37408.36	0.00	P(15)	Q(13)	37411.52	0.02	P(13)
P(15)	37408.39	0.03	P(15)	Q(14)	37411.63	0.02	P(14)
P(14)	37408.48	0.01	P(14)	Q(15)	37411.69	-0.05	P(15)
P(13)	37408.59	0.01	P(13)	Q(15)	37411.73	-0.01	P(15)
P(13)	37408.62	0.04	P(13)	Q(15)	37411.73	0.00	P(15)
P(12)	37408.68	-0.02	P(12)	Q(16)	37411.86	0.00	P(16)
P(10)	37408.91	-0.06	P(10)	Q(17)	37411.98	-0.02	P(17)
P(9)	37409.12	0.01	P(9)	Q(17)	37411.99	-0.02	P(17)
P(9)	37409.13	0.01	P(9)	Q(18)	37412.10	-0.04	P(18)
P(8)	37409.25	-0.01	P(8)	Q(18)	37412.17	0.02	P(18)
P(7)	37409.44	0.01	P(7)	R(5)	37412.23	-0.02	P(5)
P(5)	37409.76	-0.01	P(5)	R(9)	37413.39	0.00	P(9)
P(3)	37410.11	-0.04	P(3)	R(9)	37413.39	0.00	P(9)
Q(7)	37411.00	0.00	P(7)	R(11)	37414.03	0.03	P(11)
Q(7)	37411.02	0.02	P(7)	R(12)	37414.31	-0.02	P(12)
Q(8)	37411.07	0.01	P(8)	R(13)	37414.65	-0.01	P(13)
Q(9)	37411.15	0.01	P(9)	R(13)	37414.68	0.03	P(13)
Q(9)	37411.16	0.02	P(9)	R(14)	37415.00	0.01	P(14)

Transition	Observed	Residuals	Probe	Transition	Observed	Residuals	Probe
R(15)	37415.34	0.00	P(15)	R(17)	37416.04	-0.01	P(17)
R(15)	37415.34	0.00	P(15)	R(18)	37416.41	-0.01	P(18)
R(15)	37415.36	0.02	P(15)	R(18)	37416.42	0.00	P(18)
R(16)	37415.68	-0.01	P(16)				
("*x*+2",0) I-X							
P(20)	37734.68	-0.07	P(20)	Q(14)	37701.01	-0.08	P(14)
P(18)	37734.74	-0.02	P(18)	R(3)	37701.04	-0.07	P(3)
P(17)	37734.77	0.00	P(17)	Q(14)	37701.07	-0.02	P(14)
P(19)	37734.78	0.03	P(19)	Q(15)	37701.17	-0.05	P(15)
P(22)	37734.80	0.00	P(22)	Q(15)	37701.24	0.01	P(15)
P(21)	37734.82	0.05	P(21)	Q(16)	37701.39	0.02	P(16)
P(16)	37734.83	0.03	P(16)	Q(17)	37701.50	-0.03	P(17)
P(14)	37734.85	-0.05	P(14)	R(5)	37701.62	-0.02	P(5)
P(14)	37734.88	-0.03	P(14)	Q(18)	37701.69	0.00	P(18)
P(15)	37734.90	0.05	P(15)	R(7)	37702.26	0.05	P(7)
P(24)	37734.94	0.05	P(24)	R(8)	37702.51	0.00	P(8)
P(25)	37734.98	0.03	P(25)	R(9)	37702.85	0.04	P(9)
P(13)	37735.01	0.04	P(13)	R(10)	37703.07	-0.06	P(10)
P(12)	37735.01	-0.03	P(12)	R(10)	37703.12	-0.01	P(10)
P(26)	37735.06	0.03	P(26)	R(12)	37703.76	-0.03	P(12)
P(27)	37735.15	0.03	P(27)	R(13)	37704.15	0.03	P(13)
Q(5)	37700.22	-0.07	P(5)	R(14)	37704.46	-0.02	P(14)
Q(8)	37700.47	0.00	P(8)	R(14)	37704.49	0.01	P(14)
Q(7)	37700.47	0.07	P(7)	R(15)	37704.81	-0.03	P(15)
Q(9)	37700.55	0.00	P(9)	R(15)	37704.87	0.03	P(15)
Q(10)	37700.59	-0.05	P(10)	R(16)	37705.22	0.01	P(16)
Q(10)	37700.68	0.03	P(10)	R(17)	37705.60	0.01	P(17)
Q(12)	37700.77	-0.08	P(12)	R(18)	37705.99	0.01	P(18)
Q(13)	37700.97	0.00	P(13)				

10.5 Line list underlying Chapter 5.3

Table 14: List of all lines assigned. For all TC-RFWM assignments, the probe transition is specified. Assignments without probe originate in LIF excitation scans.

Transition	Observed	Residuals	Probe	Transition	Observed	Residuals	Probe
$^{63}Cu_2$: *G62* – X (*v*=0)							
P(9)	37508.150	0.018		R(10)	37509.463	0.005	
P(10)	37506.998	-0.014		R(11)	37508.445	-0.025	
P(11)	37505.770	-0.021		R(12)	37507.353	-0.029	
P(12)	37504.485	0.016		R(13)	37506.155	-0.038	
P(13)	37503.066	0.018		R(14)	37504.916	0.012	
P(14)	37501.499	-0.027		R(15)	37503.521	0.005	
P(15)	37499.900	-0.004		R(16)	37502.018	-0.009	
P(16)	37498.191	0.009		R(17)	37500.417	-0.020	
P(17)	37496.356	-0.003		R(18)	37498.741	-0.007	
P(18)	37494.450	0.013		R(19)	37496.957	-0.002	
P(19)	37492.426	0.012		R(20)	37495.080	0.010	
P(20)	37490.255	-0.037		R(21)	37493.074	-0.007	
P(21)	37488.070	0.000		R(22)	37491.018	0.025	
P(22)	37485.755	0.008		R(24)	37486.539	0.020	
P(23)	37483.343	0.017		R(25)	37484.157	0.023	
P(25)	37478.196	0.012		R(26)	37481.676	0.026	
P(26)	37475.461	-0.004		R(27)	37479.059	-0.012	
P(27)	37472.645	-0.002		R(28)	37476.410	0.011	
P(27)	37472.660	0.013		R(29)	37473.600	-0.001	
P(28)	37469.737	0.006		R(29)	37473.612	0.011	
P(28)	37469.760	0.029		R(30)	37470.789	0.010	
P(29)	37466.732	0.013		R(30)	37470.809	0.030	
P(29)	37466.736	0.017		R(31)	37467.876	-0.032	P(31)
P(30)	37463.631	0.016		R(31)	37467.896	-0.012	
P(31)	37460.369	-0.015	P(31)	R(31)	37467.937	0.029	
P(32)	37457.142	0.012	P(32)	R(32)	37465.343	-0.038	P(32)

Transition	Observed	Residuals	Probe	Transition	Observed	Residuals	Probe
P(33)	37453.808	-0.019	P(33)	R(32)	37465.383	0.002	
P(34)	37450.861	-0.007	P(34)	R(33)	37460.962	-0.023	P(33)
P(35)	37446.008	-0.033	P(35)	R(33)	37461.008	0.023	
P(36)	37442.493	-0.020	P(36)	R(35)	37454.564	-0.001	P(35)
P(37)	37438.719	-0.038					
$^{63}Cu_2$: *G64* – X (*v*=0)							
P(5)	37714.993	-0.008	P(5)	R(7)	37715.242	0.013	P(7)
P(7)	37713.471	-0.001	P(7)	R(9)	37713.763	0.000	P(9)
P(9)	37711.536	-0.005	P(9)	R(13)	37709.616	-0.002	P(13)
P(13)	37706.473	0.003	P(13)	R(15)	37706.960	0.023	P(15)
P(15)	37703.348	0.020	P(15)	R(17)	37703.816	-0.035	P(17)
P(17)	37699.775	-0.006	P(17)	R(19)	37700.367	0.008	P(19)
R(5)	37716.283	-0.009	P(5)				
$^{63}Cu_2$: *G65* – X (*v*=0)							
P(5)	37816.680	-0.006		R(11)	37813.415	-0.034	
P(7)	37815.090	-0.041		R(13)	37811.110	-0.025	
P(9)	37813.188	0.018		R(14)	37809.792	-0.034	
P(11)	37810.772	-0.030		R(15)	37808.383	-0.032	
P(13)	37808.045	0.018		R(16)	37806.935	0.032	
P(15)	37804.828	-0.018		R(17)	37805.251	-0.038	
P(17)	37801.311	0.053		R(19)	37801.762	0.004	
P(18)	37799.332	0.019		R(20)	37799.818	-0.023	
P(19)	37797.285	0.019		R(21)	37797.828	0.005	
P(20)	37795.144	0.026		R(22)	37795.674	-0.031	
P(21)	37792.948	0.079		R(23)	37793.488	0.002	
P(23)	37788.079	0.011		R(24)	37791.186	0.018	
P(26)	37780.133	0.020		R(25)	37788.760	0.011	
P(27)	37777.287	0.025		R(26)	37786.264	0.033	
P(30)	37768.103	-0.015		R(27)	37783.648	0.032	
P(31)	37764.919	0.042		R(28)	37780.913	0.011	
P(34)	37754.591	-0.027	P(34)	R(29)	37778.102	0.008	

Transition	Observed	Residuals	Probe	Transition	Observed	Residuals	Probe
P(34)	37754.595	-0.023	P(34)	R(30)	37775.158	-0.034	
P(35)	37751.057	0.005	P(35)	R(31)	37772.216	0.014	
P(36)	37747.457	-0.005	P(36)	R(32)	37769.181	0.050	
P(37)	37743.944	-0.018	P(37)	R(33)	37766.008	0.011	
P(37)	37743.944	-0.018	P(37)	R(35)	37759.759	-0.011	P(35)
P(37)	37743.946	-0.016	P(37)	R(35)	37759.760	-0.010	P(35)
P(38)	37740.961	0.022	P(38)	R(35)	37759.779	0.009	
P(38)	37740.973	0.034	P(38)	R(36)	37757.169	-0.010	
P(43)	37717.149	-0.049	P(43)	R(36)	37757.186	0.007	P(36)
P(43)	37717.162	-0.036	P(43)	R(36)	37757.187	0.008	P(36)
R(6)	37817.435	-0.020		R(37)	37749.820	-0.009	P(37)
R(7)	37816.808	-0.050		R(37)	37749.820	-0.009	P(37)
R(8)	37816.105	-0.053		R(37)	37749.829	0.000	P(37)
R(9)	37815.368	0.011		R(38)	37746.878	0.023	P(38)
R(10)	37814.506	0.052					
$^{63}Cu_2$: *G67* – X (*v*=0)							
P(3)	38015.035	0.030	P(3)	R(5)	38015.744	-0.057	P(5)
P(5)	38014.149	0.007	P(5)	R(7)	38015.167	0.016	P(7)
P(7)	38012.994	0.013	P(7)	R(8)	38014.670	-0.004	P(8)
P(8)	38012.262	-0.008	P(8)	R(9)	38014.100	0.013	P(9)
P(9)	38011.479	0.016	P(9)	R(10)	38013.369	-0.018	P(5)
P(10)	38010.573	0.021	P(10)	R(10)	38013.385	-0.002	P(10)
P(10)	38010.574	0.022	P(5)	R(11)	38012.556	-0.013	P(11)
P(11)	38009.522	-0.010	P(11)	R(11)	38012.566	-0.003	P(11)
P(11)	38009.527	-0.005	P(11)	R(12)	38011.641	0.008	P(12)
P(12)	38008.384	-0.014	P(12)	R(15)	38008.112	0.003	P(15)
P(15)	38004.263	-0.025	P(15)	R(17)	38005.191	0.018	P(17)
R(3)	38016.088	-0.006	P(3)				
$^{63}Cu_2$: *G68* – X (*v*=0)							
P(40)	38032.963	-0.062	P(40)	R(40)	38035.560	-0.037	P(40)
P(40)	38033.004	-0.021	P(27)	R(40)	38035.578	-0.019	P(40)

Transition	Observed	Residuals	Probe	Transition	Observed	Residuals	Probe
P(40)	38033.045	0.020	P(40)	R(40)	38035.578	-0.019	P(27)
P(41)	38029.713	-0.029	P(41)	R(41)	38033.149	-0.011	P(41)
P(41)	38029.783	0.041	P(41)	R(41)	38033.188	0.029	P(41)
P(42)	38017.640	0.007	P(42)	R(42)	38029.854	-0.004	P(42)
R(38)	38050.177	0.050	P(38)	R(42)	38029.872	0.014	P(42)
R(39)	38047.294	0.019	P(39)				
$^{63}Cu_2$: *I1* – X (*v*=0)							
P(3)	37410.110	-0.048	P(3)	Q(24)	37413.073	-0.067	P(5)
P(5)	37409.715	-0.064	P(5)	Q(24)	37413.142	0.002	P(24)
P(5)	37409.760	-0.019	P(5)	Q(25)	37413.301	-0.027	P(25)
P(7)	37409.435	0.004	P(1)	Q(26)	37413.501	-0.021	P(26)
P(8)	37409.224	-0.045	P(2)	Q(27)	37413.658	-0.063	P(27)
P(8)	37409.254	-0.015	P(8)	Q(28)	37413.879	-0.046	P(28)
P(9)	37409.101	-0.013	P(4)	Q(29)	37414.053	-0.081	P(27)
P(9)	37409.121	0.007	P(9)	Q(29)	37414.106	-0.028	P(29)
P(9)	37409.125	0.011	P(9)	Q(30)	37414.338	-0.010	P(30)
P(10)	37408.911	-0.056	P(10)	Q(31)	37414.470	-0.096	P(31)
P(12)	37408.684	-0.013	P(12)	Q(31)	37414.569	0.003	P(31)
P(13)	37408.589	0.016	P(9)	Q(33)	37414.963	-0.050	P(33)
P(13)	37408.619	0.046	P(13)	Q(33)	37415.011	-0.002	P(33)
P(14)	37408.478	0.021	P(14)	Q(33)	37415.016	0.003	P(33)
P(15)	37408.357	0.008	P(15)	Q(35)	37415.457	-0.013	P(35)
P(15)	37408.362	0.013	P(15)	Q(37)	37415.952	0.018	P(37)
P(15)	37408.392	0.043	P(11)	Q(40)	37416.605	-0.024	P(40)
P(16)	37408.277	0.029	P(16)	Q(43)	37417.381	0.076	P(43)
P(17)	37408.204	0.049	P(17)	Q(44)	37417.542	0.020	P(44)
P(18)	37408.105	0.035	P(18)	Q(45)	37417.781	0.048	P(45)
P(19)	37408.043	0.051	P(19)	Q(46)	37417.996	0.060	P(46)
P(19)	37408.046	0.054	P(16)	Q(47)	37418.126	-0.005	P(47)
P(21)	37407.873	0.015	P(21)	Q(48)	37418.363	0.047	P(48)
P(21)	37407.886	0.028	P(21)	Q(49)	37418.583	0.092	P(49)

Transition	Observed	Residuals	Probe	Transition	Observed	Residuals	Probe
P(22)	37407.844	0.042	P(22)	Q(50)	37418.699	0.047	P(50)
P(23)	37407.767	0.014	P(23)	Q(51)	37418.874	0.074	P(51)
P(24)	37407.733	0.023	P(24)	Q(52)	37418.984	0.052	P(52)
P(25)	37407.681	0.006	P(25)	Q(53)	37418.977	-0.069	P(53)
P(26)	37407.670	0.023	P(26)	Q(54)	37419.096	-0.045	P(54)
P(27)	37407.626	0.002	P(27)	Q(55)	37419.122	-0.093	P(55)
P(28)	37407.631	0.022	P(25)	R(5)	37412.226	-0.025	P(5)
P(28)	37407.658	0.049	P(28)	R(9)	37413.385	0.002	P(9)
P(29)	37407.584	-0.015	P(27)	R(9)	37413.388	0.005	P(9)
P(29)	37407.610	0.011	P(5)	R(11)	37414.032	0.037	P(6)
P(29)	37407.611	0.012	P(29)	R(12)	37414.308	-0.005	P(12)
P(30)	37407.603	0.008	P(30)	R(13)	37414.647	0.009	P(9)
P(31)	37407.568	-0.028	P(31)	R(13)	37414.681	0.043	P(13)
P(31)	37407.618	0.022	P(31)	R(14)	37414.995	0.024	P(14)
P(33)	37407.606	-0.008	P(33)	R(15)	37415.338	0.026	P(15)
P(33)	37407.610	-0.004	P(33)	R(15)	37415.339	0.027	P(15)
P(35)	37407.626	-0.024	P(35)	R(15)	37415.358	0.046	P(11)
P(37)	37407.694	-0.006	P(37)	R(16)	37415.678	0.018	P(16)
P(40)	37407.800	0.008	P(40)	R(17)	37416.037	0.022	P(17)
P(43)	37407.906	0.016	P(43)	R(18)	37416.411	0.034	P(15)
P(44)	37407.879	-0.042	P(44)	R(18)	37416.417	0.040	P(18)
P(45)	37407.933	-0.016	P(45)	R(19)	37416.791	0.044	P(19)
P(46)	37407.949	-0.024	P(46)	R(19)	37416.801	0.054	P(16)
P(46)	37407.977	0.004	P(46)	R(20)	37417.079	-0.045	P(1)
P(47)	37407.959	-0.034	P(47)	R(20)	37417.148	0.024	P(20)
P(48)	37408.004	-0.003	P(48)	R(20)	37417.238	0.114	P(17)
P(49)	37407.979	-0.036	P(49)	R(21)	37417.507	-0.001	P(21)
P(50)	37407.958	-0.056	P(50)	R(21)	37417.517	0.009	P(21)
P(52)	37408.021	0.038	P(52)	R(22)	37417.929	0.030	P(22)
P(53)	37407.975	0.025	P(53)	R(23)	37418.318	0.021	P(23)
P(54)	37407.901	-0.002	P(54)	R(24)	37418.723	0.022	P(24)

Transition	Observed	Residuals	Probe	Transition	Observed	Residuals	Probe
P(55)	37407.868	0.028	P(55)	R(25)	37419.129	0.018	P(25)
Q(7)	37411.003	-0.009	P(1)	R(26)	37419.531	0.003	P(1)
Q(7)	37411.020	0.008	P(7)	R(26)	37419.535	0.007	P(26)
Q(8)	37411.060	-0.016	P(2)	R(27)	37419.930	-0.021	P(8)
Q(8)	37411.074	-0.002	P(8)	R(27)	37419.943	-0.008	P(27)
Q(9)	37411.115	-0.033	P(4)	R(28)	37420.385	0.006	P(28)
Q(9)	37411.145	-0.003	P(9)	R(29)	37420.776	-0.036	P(10)
Q(9)	37411.155	0.007	P(9)	R(29)	37420.776	-0.036	P(10)
Q(10)	37411.192	-0.037	P(5)	R(29)	37420.798	-0.014	P(27)
Q(10)	37411.202	-0.027	P(10)	R(29)	37420.816	0.004	P(29)
Q(11)	37411.316	-0.001	P(6)	R(29)	37420.828	0.016	P(5)
Q(12)	37411.382	-0.031	P(12)	R(30)	37421.310	0.059	P(30)
Q(13)	37411.505	-0.011	P(9)	R(31)	37421.708	0.013	P(31)
Q(13)	37411.519	0.003	P(13)	R(31)	37421.723	0.028	P(31)
Q(14)	37411.632	0.004	P(14)	R(33)	37422.569	-0.025	P(33)
Q(15)	37411.689	-0.057	P(15)	R(33)	37422.575	-0.019	P(33)
Q(15)	37411.727	-0.019	P(15)	R(35)	37423.510	0.003	P(35)
Q(15)	37411.733	-0.013	P(11)	R(37)	37424.442	0.012	P(37)
Q(16)	37411.861	-0.012	P(16)	R(40)	37425.819	-0.003	P(40)
Q(17)	37411.983	-0.024	P(14)	R(43)	37427.178	-0.026	P(43)
Q(17)	37411.985	-0.022	P(17)	R(44)	37427.634	-0.025	P(44)
Q(18)	37412.104	-0.044	P(15)	R(45)	37428.066	-0.043	P(45)
Q(18)	37412.168	0.020	P(18)	R(46)	37428.561	0.008	P(46)
Q(19)	37412.286	-0.010	P(16)	R(47)	37428.965	-0.025	P(47)
Q(19)	37412.290	-0.006	P(19)	R(48)	37429.407	-0.012	P(48)
Q(20)	37412.431	-0.021	P(17)	R(49)	37429.853	0.015	P(49)
Q(20)	37412.456	0.004	P(20)	R(50)	37430.210	-0.037	P(50)
Q(21)	37412.575	-0.039	P(21)	R(51)	37430.636	-0.007	P(51)
Q(21)	37412.597	-0.017	P(21)	R(52)	37431.035	0.011	P(52)
Q(21)	37412.605	-0.009	P(18)	R(53)	37431.380	-0.011	P(53)
Q(22)	37412.755	-0.028	P(22)	R(54)	37431.731	-0.008	P(54)

Transition	Observed	Residuals	Probe	Transition	Observed	Residuals	Probe
Q(23)	37412.922	-0.036	P(23)	R(55)	37432.110	0.041	P(55)
$^{63}Cu_2$: *I2* – X (*v*=0)							
P(3)	37699.503	0.002	P(3)	Q(29)	37704.163	0.027	P(27)
P(5)	37699.205	0.073	P(5)	Q(31)	37704.724	0.022	P(8)
P(7)	37698.874	0.075	P(7)	Q(34)	37705.540	-0.084	P(34)
P(8)	37698.669	0.022	P(8)	Q(35)	37705.853	-0.097	P(35)
P(9)	37698.550	0.046	P(9)	Q(35)	37705.871	-0.079	P(35)
P(9)	37698.571	0.067	P(9)	Q(37)	37706.734	0.102	P(37)
P(10)	37698.402	0.031	P(5)	Q(38)	37707.051	0.063	P(38)
P(12)	37698.141	0.010	P(12)	Q(40)	37707.766	0.038	P(40)
P(13)	37698.070	0.044	P(13)	Q(41)	37708.146	0.033	P(41)
P(14)	37697.930	0.001	P(10)	Q(42)	37708.536	0.028	P(42)
P(14)	37697.937	0.008	P(14)	Q(43)	37708.896	-0.016	P(43)
P(15)	37697.862	0.020	P(15)	Q(45)	37709.792	0.041	P(45)
P(16)	37697.792	0.028	P(16)	Q(46)	37710.240	0.054	P(46)
P(17)	37697.725	0.029	P(17)	Q(47)	37710.664	0.034	P(47)
P(18)	37697.623	-0.014	P(18)	Q(48)	37711.121	0.036	P(48)
P(19)	37697.615	0.027	P(19)	Q(49)	37711.560	0.011	P(49)
P(20)	37697.516	-0.031	P(17)	Q(50)	37711.981	-0.043	P(50)
P(20)	37697.534	-0.013	P(1)	Q(51)	37712.508	-0.001	P(51)
P(21)	37697.504	-0.013	P(18)	Q(52)	37712.948	-0.056	P(52)
P(21)	37697.547	0.030	P(21)	R(3)	37701.036	-0.048	P(3)
P(22)	37697.452	-0.043	P(3)	R(5)	37701.617	-0.002	P(5)
P(22)	37697.506	0.011	P(23)	R(7)	37702.255	0.063	P(7)
P(22)	37697.524	0.029	P(22)	R(8)	37702.509	0.017	P(8)
P(24)	37697.512	0.031	P(24)	R(9)	37702.841	0.040	P(9)
P(25)	37697.508	0.020	P(25)	R(9)	37702.848	0.047	P(9)
P(26)	37697.490	-0.015	P(26)	R(10)	37703.067	-0.053	P(10)
P(27)	37697.511	-0.020	P(8)	R(10)	37703.121	0.001	P(5)
P(27)	37697.564	0.033	P(27)	R(12)	37703.760	-0.025	P(12)
P(34)	37697.975	-0.009	P(34)	R(13)	37704.154	0.022	P(13)

Transition	Observed	Residuals	Probe	Transition	Observed	Residuals	Probe
P(35)	37698.057	-0.030	P(35)	R(14)	37704.464	-0.023	P(14)
P(35)	37698.062	-0.025	P(35)	R(14)	37704.486	-0.001	P(10)
P(37)	37698.265	-0.059	P(37)	R(15)	37704.808	-0.044	P(11)
P(38)	37698.367	-0.090	P(38)	R(15)	37704.867	0.015	P(15)
P(42)	37699.164	0.077	P(42)	R(16)	37705.224	-0.003	P(16)
P(43)	37699.346	0.077	P(43)	R(17)	37705.598	-0.013	P(17)
P(44)	37699.571	0.109	P(44)	R(18)	37705.990	-0.014	P(18)
P(45)	37699.681	0.017	P(45)	R(19)	37706.432	0.026	P(19)
P(46)	37699.889	0.012	P(46)	R(20)	37706.788	-0.030	P(17)
P(47)	37700.160	0.060	P(47)	R(20)	37706.797	-0.021	P(1)
P(48)	37700.328	-0.005	P(48)	R(21)	37707.232	-0.007	P(18)
P(49)	37700.627	0.051	P(49)	R(21)	37707.241	0.002	P(21)
P(50)	37700.816	-0.014	P(50)	R(22)	37707.618	-0.052	P(3)
P(51)	37701.058	-0.035	P(51)	R(22)	37707.660	-0.010	P(22)
P(52)	37701.325	-0.042	P(52)	R(23)	37708.109	-0.001	P(23)
P(55)	37702.176	-0.076	P(55)	R(24)	37708.496	-0.063	P(5)
Q(1)	37700.177	0.044	P(1)	R(24)	37708.561	0.002	P(24)
Q(3)	37700.177	-0.002	P(3)	R(25)	37709.018	0.000	P(25)
Q(5)	37700.215	-0.046	P(5)	R(26)	37709.439	-0.047	P(7)
Q(7)	37700.470	0.089	P(7)	R(26)	37709.439	-0.047	P(26)
Q(8)	37700.469	0.015	P(8)	R(27)	37709.937	-0.027	P(8)
Q(9)	37700.554	0.018	P(9)	R(27)	37709.964	0.000	P(27)
Q(9)	37700.569	0.033	P(9)	R(28)	37710.444	-0.008	P(26)
Q(10)	37700.588	-0.040	P(5)	R(29)	37710.946	-0.002	P(27)
Q(10)	37700.677	0.049	P(10)	R(30)	37711.475	0.020	P(28)
Q(12)	37700.766	-0.073	P(12)	R(31)	37711.984	0.013	P(8)
Q(13)	37700.968	0.009	P(13)	R(34)	37713.560	-0.017	P(34)
Q(14)	37701.014	-0.074	P(14)	R(35)	37714.078	-0.053	P(35)
Q(14)	37701.071	-0.017	P(10)	R(35)	37714.083	-0.048	P(35)
Q(15)	37701.172	-0.053	P(11)	R(36)	37714.603	-0.093	P(36)
Q(15)	37701.238	0.013	P(15)	R(37)	37715.281	0.011	P(37)

Transition	Observed	Residuals	Probe	Transition	Observed	Residuals	Probe
Q(16)	37701.388	0.015	P(16)	R(40)	37717.148	0.098	P(40)
Q(17)	37701.497	-0.032	P(17)	R(41)	37717.741	0.077	P(41)
Q(18)	37701.690	-0.005	P(18)	R(42)	37718.351	0.064	P(42)
Q(19)	37701.899	0.029	P(19)	R(43)	37718.968	0.048	P(43)
Q(20)	37701.998	-0.056	P(1)	R(44)	37719.617	0.054	P(44)
Q(20)	37702.024	-0.030	P(17)	R(45)	37720.190	-0.026	P(45)
Q(21)	37702.209	-0.039	P(18)	R(45)	37720.228	0.012	P(45)
Q(21)	37702.260	0.012	P(21)	R(46)	37720.922	0.043	P(46)
Q(22)	37702.385	-0.066	P(3)	R(47)	37721.532	-0.020	P(47)
Q(22)	37702.422	-0.029	P(22)	R(48)	37722.206	-0.029	P(48)
Q(24)	37702.815	-0.070	P(5)	R(49)	37722.941	0.013	P(49)
Q(24)	37702.896	0.011	P(24)	R(50)	37723.607	-0.024	P(50)
Q(25)	37703.100	-0.016	P(25)	R(50)	37723.745	0.114	P(50)
Q(26)	37703.317	-0.040	P(7)	R(51)	37724.300	-0.045	P(51)
Q(26)	37703.373	0.016	P(26)	R(52)	37724.996	-0.073	P(51)
Q(27)	37703.554	-0.053	P(8)	R(52)	37725.006	-0.063	P(52)
Q(27)	37703.613	0.006	P(27)				
$^{63}Cu_2$: (0,0) J – X							
P(8)	37447.350	-0.056	P(8)	R(17)	37455.038	-0.026	P(14)
P(9)	37447.252	-0.050	P(9)	R(17)	37455.082	0.018	P(17)
P(10)	37447.295	0.083	P(10)	R(19)	37456.071	0.025	P(19)
P(11)	37447.178	0.041	R(11)	R(20)	37456.525	-0.033	P(1)
P(12)	37447.051	-0.025	P(12)	R(20)	37456.571	0.014	P(20)
P(15)	37446.909	-0.067	P(15)	R(20)	37456.578	0.021	P(17)
P(15)	37446.941	-0.035	P(15)	R(21)	37457.089	0.006	P(21)
P(19)	37447.064	0.024	P(19)	R(21)	37457.140	0.057	P(21)
P(19)	37447.075	0.035	P(16)	R(22)	37457.573	-0.048	P(3)
P(20)	37447.053	-0.039	P(1)	R(22)	37457.654	0.033	P(22)
P(20)	37447.102	0.011	P(20)	R(23)	37458.202	0.029	P(23)
P(21)	37447.132	-0.024	P(21)	R(24)	37458.661	-0.077	P(5)
P(21)	37447.176	0.020	P(21)	R(24)	37458.673	-0.065	P(5)

Transition	Observed	Residuals	Probe	Transition	Observed	Residuals	Probe
P(22)	37447.279	0.044	P(22)	R(24)	37458.744	0.006	P(24)
P(23)	37447.366	0.039	P(23)	R(25)	37459.338	0.022	P(25)
P(24)	37447.480	0.047	P(24)	R(26)	37459.924	0.019	P(26)
P(25)	37447.582	0.030	P(25)	R(27)	37460.476	-0.028	P(8)
P(27)	37447.845	0.016	P(27)	R(27)	37460.479	-0.025	P(3)
P(29)	37448.132	-0.021	P(5)	R(27)	37460.528	0.024	P(27)
P(31)	37448.467	-0.041	P(31)	R(28)	37461.101	-0.012	P(4)
P(32)	37448.642	-0.037	P(32)	R(28)	37461.145	0.033	P(28)
P(33)	37448.804	0.012	P(33)	R(29)	37461.700	-0.024	P(10)
P(34)	37448.467	-0.004	P(34)	R(29)	37461.707	-0.017	P(5)
P(35)	37449.960	0.029	P(35)	R(29)	37461.742	0.018	P(27)
P(36)	37450.032	0.030	P(36)	R(29)	37461.745	0.021	P(5)
P(38)	37450.424	-0.033	P(38)	R(29)	37461.749	0.025	P(29)
P(39)	37450.687	-0.030	P(39)	R(30)	37462.357	0.030	P(30)
P(40)	37450.977	0.003	P(40)	R(31)	37462.856	-0.016	P(31)
P(41)	37451.201	-0.010	P(41)	R(31)	37462.900	0.028	P(31)
P(41)	37451.202	-0.009	P(41)	R(32)	37462.998	0.014	P(32)
P(43)	37451.463	0.012	P(43)	R(33)	37464.890	0.014	P(33)
P(44)	37453.929	-0.013	P(44)	R(34)	37465.378	-0.001	P(34)
P(49)	37455.247	-0.064	P(49)	R(35)	37466.099	0.081	P(35)
P(53)	37457.170	0.031	P(53)	R(36)	37466.615	-0.081	P(36)
R(3)	37449.726	-0.028	P(3)	R(36)	37466.623	-0.073	P(36)
R(5)	37450.280	-0.064	P(5)	R(38)	37468.039	-0.037	P(38)
R(5)	37450.290	-0.054	P(5)	R(39)	37468.730	-0.014	P(39)
R(7)	37451.012	0.022	P(7)	R(40)	37469.319	-0.036	P(40)
R(7)	37451.063	0.073	P(1)	R(40)	37469.381	0.026	P(40)
R(8)	37451.280	-0.054	P(8)	R(41)	37469.775	-0.071	P(41)
R(8)	37451.285	-0.049	P(2)	R(41)	37469.836	-0.010	P(41)
R(9)	37451.665	-0.027	P(4)	R(41)	37469.898	0.052	P(41)
R(9)	37451.670	-0.022	P(9)	R(42)	37472.787	0.020	P(42)
R(10)	37452.012	-0.052	P(5)	R(43)	37473.276	0.027	P(43)

Transition	Observed	Residuals	Probe	Transition	Observed	Residuals	Probe
R(10)	37452.082	0.018	P(10)	R(44)	37473.936	0.041	P(44)
R(11)	37452.515	0.064	P(6)	R(49)	37478.100	0.055	P(49)
R(12)	37452.802	-0.049	P(12)	R(50)	37478.947	0.002	R(50)
R(13)	37453.301	0.035	P(13)	R(51)	37479.799	-0.033	R(51)
R(13)	37453.319	0.053	P(9)	R(51)	37479.841	0.009	P(51)
R(14)	37453.750	0.056	P(14)	R(52)	37480.465	-0.052	P(52)
R(15)	37454.142	0.005	P(15)	R(52)	37480.497	-0.020	R(52)
R(15)	37454.161	0.024	P(15)	R(52)	37480.559	0.042	P(52)
R(15)	37454.184	0.047	P(11)	R(53)	37482.137	-0.072	P(53)
R(16)	37454.621	0.028	P(16)	R(54)	37483.029	0.008	P(54)
$^{63}Cu_2$: (1,0) J – X							
P(5)	37735.880	-0.056	P(5)	R(12)	37740.761	0.015	P(12)
P(7)	37735.643	0.022	P(7)	R(13)	37741.147	0.023	P(13)
P(9)	37735.381	0.029	P(9)	R(14)	37741.497	-0.018	P(10)
P(12)	37735.014	-0.024	P(12)	R(14)	37741.498	-0.017	P(14)
P(13)	37735.006	0.049	P(13)	R(15)	37741.958	0.040	P(15)
P(14)	37734.847	-0.043	P(14)	R(16)	37742.368	0.034	P(16)
P(14)	37734.875	-0.015	P(10)	R(17)	37742.737	-0.026	P(17)
P(15)	37734.897	0.063	P(15)	R(18)	37743.194	-0.009	P(18)
P(16)	37734.833	0.041	P(16)	R(19)	37743.681	0.025	P(19)
P(17)	37734.769	0.007	P(17)	R(20)	37744.038	-0.084	P(17)
P(18)	37734.736	-0.008	P(18)	R(21)	37744.656	0.057	P(21)
P(19)	37734.778	0.039	P(19)	R(22)	37745.056	-0.033	P(22)
P(20)	37734.679	-0.068	P(17)	R(24)	37746.065	-0.037	P(24)
P(21)	37734.821	0.054	P(21)	R(25)	37746.625	0.000	P(25)
P(22)	37734.798	-0.001	P(22)	R(26)	37747.177	0.018	P(26)
P(24)	37734.936	0.036	P(24)	R(27)	37747.666	-0.037	P(27)
P(25)	37734.984	0.016	P(25)	R(28)	37748.259	0.004	P(26)
P(26)	37735.062	0.014	P(26)	R(29)	37748.754	-0.060	P(5)
P(27)	37735.148	0.010	P(27)	R(29)	37748.779	-0.035	P(27)
P(29)	37735.292	-0.059	P(29)	R(29)	37748.807	-0.007	P(29)

Transition	Observed	Residuals	Probe	Transition	Observed	Residuals	Probe
P(29)	37735.341	-0.010	P(27)	R(30)	37749.382	0.005	P(28)
P(30)	37735.448	-0.022	P(28)	R(31)	37749.939	-0.001	P(8)
P(31)	37735.627	0.030	P(8)	R(32)	37750.486	-0.010	P(32)
P(32)	37735.668	-0.060	P(32)	R(33)	37751.081	0.055	P(33)
P(34)	37735.948	-0.035	P(34)	R(34)	37751.442	-0.050	P(34)
P(34)	37735.960	-0.023	P(34)	R(34)	37751.506	0.014	P(34)
P(34)	37736.016	0.033	P(34)	R(34)	37751.509	0.017	P(34)
P(35)	37736.089	0.008	P(35)	R(35)	37751.735	-0.044	P(35)
P(35)	37736.110	0.029	P(35)	R(35)	37751.751	-0.028	P(35)
P(36)	37736.127	0.012	P(36)	R(36)	37751.496	-0.005	P(36)
P(36)	37736.141	0.026	P(36)	R(36)	37751.496	-0.005	P(36)
P(37)	37736.034	0.063	P(37)	R(37)	37755.882	-0.011	P(37)
P(37)	37736.035	0.064	P(37)	R(37)	37755.883	-0.010	P(37)
P(38)	37735.256	-0.006	P(38)	R(37)	37755.886	-0.007	P(37)
P(38)	37735.285	0.023	P(38)	R(38)	37755.796	-0.024	P(38)
P(40)	37738.743	0.025	P(40)	R(38)	37755.801	-0.019	P(38)
P(41)	37738.661	-0.020	P(41)	R(40)	37756.769	-0.005	P(40)
P(42)	37738.871	0.060	P(42)	R(41)	37757.415	0.003	P(41)
P(43)	37739.048	0.030	P(43)	R(42)	37758.079	-0.016	P(42)
P(43)	37739.061	0.043	P(43)	R(43)	37758.805	-0.003	P(43)
P(44)	37739.256	-0.014	P(44)	R(43)	37758.805	-0.003	P(43)
P(46)	37739.847	-0.011	P(46)	R(44)	37759.567	0.023	P(44)
P(49)	37740.887	0.010	P(49)	R(46)	37761.048	-0.021	P(46)
P(51)	37741.525	-0.093	P(50)	R(47)	37761.832	-0.021	P(47)
P(52)	37742.016	0.019	P(51)	R(48)	37762.675	0.027	P(48)
P(53)	37742.409	0.033	P(53)	R(49)	37763.426	-0.026	P(49)
R(5)	37738.421	-0.020	P(5)	R(51)	37765.003	-0.066	P(51)
R(7)	37739.040	0.001	P(7)	R(52)	37765.837	-0.023	P(52)
R(8)	37739.354	-0.002	P(8)	R(52)	37765.929	0.069	P(52)
R(9)	37739.707	0.022	P(9)	R(53)	37766.502	-0.094	P(53)
R(10)	37739.972	-0.054	P(5)	R(54)	37767.081	-0.049	P(54)

Transition	Observed	Residuals	Probe	Transition	Observed	Residuals	Probe
$^{63}Cu_2$: (2,0) J – X							
P(3)	38025.595	0.011	P(3)	R(7)	38027.147	0.010	P(7)
P(5)	38024.932	0.004	P(5)	R(8)	38027.231	0.023	P(8)
P(7)	38024.150	-0.047	P(7)	R(9)	38027.329	0.035	P(9)
P(8)	38023.769	-0.053	P(8)	R(10)	38027.388	-0.011	P(10)
P(9)	38023.459	0.010	P(9)	R(11)	38027.517	-0.007	P(11)
P(10)	38023.089	0.002	P(10)	R(11)	38027.524	0.000	P(11)
P(11)	38022.739	0.000	P(11)	R(12)	38027.627	-0.042	P(12)
P(11)	38022.750	0.011	P(11)	R(14)	38028.003	0.005	P(14)
P(12)	38022.399	-0.011	P(12)	R(15)	38028.138	-0.011	P(15)
P(14)	38021.818	0.005	P(14)	R(15)	38028.154	0.006	P(15)
P(15)	38021.543	0.003	P(15)	R(16)	38028.204	-0.009	P(16)
P(15)	38021.585	0.045	P(15)	R(16)	38028.205	-0.008	P(16)
P(16)	38021.271	-0.004	P(16)	R(17)	38029.740	-0.020	P(17)
P(17)	38020.974	-0.018	P(17)	R(18)	38029.711	-0.017	P(18)
P(18)	38020.664	0.041	P(18)	R(18)	38029.751	0.023	P(18)
P(19)	38021.784	0.047	P(19)	R(19)	38029.914	0.004	P(19)
P(20)	38021.295	0.023	P(17)	R(19)	38029.916	0.006	P(16)
P(20)	38021.298	0.026	P(20)	R(20)	38030.197	0.012	P(20)
P(21)	38021.019	-0.002	P(21)	R(20)	38030.225	0.040	P(17)
P(21)	38021.023	0.002	R(33)	R(21)	38030.461	-0.045	R(33)
P(22)	38020.870	0.008	P(22)	R(21)	38030.474	-0.032	P(21)
P(23)	38020.734	-0.017	P(23)	R(22)	38030.870	0.014	P(22)
P(24)	38020.575	-0.092	P(24)	R(23)	38031.189	-0.032	P(23)
P(25)	38020.549	-0.051	P(25)	R(24)	38031.614	0.025	P(24)
P(26)	38020.525	-0.010	P(26)	R(25)	38031.870	-0.044	P(25)
P(26)	38020.546	0.011	P(26)	R(25)	38031.911	-0.003	P(25)
P(26)	38020.582	0.047	P(26)	R(25)	38031.983	0.069	P(25)
P(27)	38020.467	0.040	P(27)	R(26)	38032.772	0.001	P(26)
P(28)	38020.892	0.040	P(28)	R(26)	38032.792	0.021	P(26)
P(29)	38020.716	-0.023	P(29)	R(27)	38033.077	-0.013	P(25)

Transition	Observed	Residuals	Probe	Transition	Observed	Residuals	Probe
P(29)	38020.752	0.013	P(5)	R(27)	38033.086	-0.004	P(27)
P(30)	38020.672	-0.047	P(28)	R(28)	38033.543	0.040	P(28)
P(30)	38020.705	-0.014	P(30)	R(29)	38033.941	-0.005	P(29)
P(31)	38020.717	-0.013	P(31)	R(29)	38033.970	0.024	P(27)
P(31)	38020.728	-0.002	P(8)	R(30)	38034.348	-0.057	P(30)
P(32)	38020.726	-0.030	P(32)	R(31)	38034.866	-0.005	P(29)
P(32)	38020.778	0.022	P(32)	R(31)	38034.868	-0.003	P(31)
P(33)	38020.760	-0.030	P(33)	R(32)	38035.359	0.020	P(32)
P(34)	38020.831	0.004	P(34)	R(32)	38035.380	0.041	P(30)
P(35)	38020.848	-0.011	P(35)	R(33)	38035.759	-0.044	P(33)
P(36)	38020.881	0.004	P(36)	R(34)	38036.223	-0.030	P(34)
P(37)	38020.863	-0.003	P(37)	R(35)	38036.649	-0.025	P(35)
P(38)	38020.885	0.085	P(38)	R(36)	38037.122	0.082	P(36)
P(39)	38020.633	0.007	P(39)	R(37)	38037.280	-0.017	P(37)
P(39)	38020.707	0.081	P(39)	R(38)	38037.303	-0.030	P(38)
P(40)	38020.217	-0.015	P(40)	R(39)	38036.937	0.032	P(39)
P(40)	38020.223	-0.009	P(40)	R(40)	38045.221	0.009	P(40)
P(40)	38020.235	0.003	P(40)	R(40)	38045.242	0.030	P(40)
P(41)	38019.346	-0.027	P(41)	R(40)	38045.242	0.030	P(27)
P(42)	38027.218	-0.031	P(42)	R(41)	38044.162	-0.026	P(41)
P(42)	38027.229	-0.020	P(42)	R(41)	38044.174	-0.014	P(41)
P(43)	38025.772	-0.022	P(43)	R(42)	38044.030	0.092	P(42)
P(44)	38025.080	-0.033	P(44)	R(43)	38044.085	-0.014	P(43)
R(3)	38026.914	0.034	P(3)	R(44)	38044.439	-0.030	P(44)
R(5)	38027.011	-0.006	P(5)				
$^{63}Cu_2$: *L1* – X (*v*=0)							
P(35)	37458.673	0.073	P(35)	P(42)	37454.498	0.001	P(42)
P(36)	37458.017	0.021	P(36)	P(43)	37454.131	0.014	P(43)
P(37)	37457.322	-0.064	P(37)	R(35)	37473.220	0.026	P(35)
P(40)	37455.483	-0.088	P(40)	R(41)	37472.484	-0.027	P(41)
P(41)	37454.981	-0.022	P(41)	R(41)	37472.485	-0.026	P(41)

Transition	Observed	Residuals	Probe	Transition	Observed	Residuals	Probe
P(41)	37455.015	0.012	P(41)	R(43)	37470.288	0.084	P(43)
$^{63}Cu_2$: *M1* – X (*v*=0)							
P(28)	38020.141	0.021	P(28)	R(28)	38031.608	-0.066	P(28)
R(26)	38032.022	-0.018	P(26)	R(29)	38031.432	0.030	P(27)
R(26)	38032.057	0.017	P(26)	R(29)	38031.433	0.031	P(29)
R(27)	38031.860	-0.047	P(27)	R(30)	38031.107	0.001	P(28)
$^{63}Cu_2$: *N1* – X (*v*=0)							
P(16)	38024.647	-0.028	P(16)	R(14)	38031.418	0.020	P(14)
P(17)	38023.621	0.033	P(17)	R(15)	38030.749	0.005	P(15)
P(18)	38022.475	-0.076	P(18)	R(16)	38030.156	0.015	P(16)
P(19)	38019.981	-0.013	P(16)	R(17)	38028.020	0.003	P(17)
P(19)	38020.019	0.025	P(19)	R(18)	38027.438	0.005	P(18)
P(20)	38018.953	-0.024	P(20)	R(19)	38026.566	-0.029	P(19)
P(20)	38018.996	0.019	P(17)	R(21)	38024.569	0.013	R(33)
P(21)	38017.706	0.001	R(33)				
$^{63}Cu^{65}Cu$: *G62* – X (*v*=0)							
P(13)	37453.987	0.036		P(39)	37383.610	-0.028	
P(15)	37451.104	-0.023	P(15)	P(40)	37379.537	-0.068	
P(16)	37449.643	0.005	P(16)	R(10)	37460.212	0.083	
P(17)	37448.249	-0.042	P(17)	R(11)	37459.300	0.010	
P(18)	37444.994	-0.037		R(12)	37458.334	-0.013	
P(18)	37445.005	-0.026	P(18)	R(13)	37457.294	-0.025	
P(19)	37443.321	-0.049		R(13)	37457.314	-0.005	P(13)
P(20)	37441.408	-0.022		R(14)	37456.218	-0.039	P(14)
P(21)	37439.319	-0.011		R(15)	37455.320	-0.016	P(15)
P(22)	37437.068	-0.038		R(16)	37452.486	-0.017	P(16)
P(23)	37434.767	-0.002		R(17)	37451.213	-0.056	P(17)
P(24)	37432.320	-0.006		R(21)	37444.367	-0.007	
P(25)	37429.791	0.013		R(22)	37442.356	-0.001	
P(26)	37427.141	0.013		R(23)	37440.229	-0.007	
P(26)	37427.151	0.023		R(24)	37438.022	0.010	

Transition	Observed	Residuals	Probe	Transition	Observed	Residuals	Probe
P(27)	37424.388	0.011		R(25)	37435.685	-0.002	
P(27)	37424.388	0.011		R(26)	37433.292	0.031	
P(28)	37421.526	0.000		R(27)	37430.767	0.031	
P(28)	37421.542	0.016		R(28)	37428.116	0.005	
P(29)	37418.589	0.015		R(28)	37428.195	0.084	
P(29)	37418.608	0.034		R(29)	37425.387	0.000	
P(30)	37415.551	0.027		R(29)	37425.408	0.021	
P(31)	37412.399	0.025		R(30)	37422.542	-0.022	
P(32)	37409.177	0.051		R(30)	37422.542	-0.022	
P(34)	37402.346	0.012		R(31)	37419.636	-0.007	
P(35)	37398.812	0.022		R(31)	37419.698	0.055	
P(36)	37395.129	-0.020		R(33)	37413.494	-0.011	
P(37)	37391.404	-0.005		R(34)	37410.256	-0.032	
P(38)	37387.532	-0.040					
^{63}Cu^{65}Cu: *G63* – X (*v*=0)							
P(45)	37459.229	0.031	P(45)	R(44)	37474.445	-0.025	P(44)
P(46)	37455.104	0.017	P(46)	R(45)	37469.114	0.003	P(45)
R(43)	37478.131	-0.027	P(43)				
^{63}Cu^{65}Cu: *G65* – X (*v*=0)							
P(20)	37745.590	-0.038	P(20)	P(37)	37693.691	-0.018	
P(21)	37743.526	0.005	P(21)	P(38)	37689.874	0.052	
P(22)	37741.395	0.023	P(3)	P(39)	37685.851	0.017	
P(23)	37739.241	0.011	P(23)	P(40)	37681.741	-0.004	
P(24)	37737.225	0.013	P(24)	P(41)	37677.532	-0.024	
P(25)	37735.503	-0.051	P(25)	R(21)	37748.789	-0.046	P(21)
P(26)	37728.495	-0.026	P(7)	R(22)	37747.251	0.008	P(3)
P(26)	37728.550	0.029		R(23)	37746.051	0.040	P(23)
P(27)	37726.348	0.016		R(24)	37739.375	-0.030	P(24)
P(27)	37726.351	0.019	P(27)	R(25)	37737.649	0.008	P(25)
P(28)	37723.763	0.008		R(26)	37735.484	-0.007	P(7)
P(29)	37720.962	0.022		R(27)	37733.072	-0.030	P(29)

Transition	Observed	Residuals	Probe	Transition	Observed	Residuals	Probe
P(30)	37717.974	0.019		R(30)	37725.028	0.005	
P(31)	37714.836	0.004		R(31)	37722.123	0.035	
P(32)	37711.615	0.030		R(32)	37719.067	0.025	
P(33)	37708.215	-0.009		R(33)	37715.881	-0.009	
P(34)	37704.744	-0.009		R(35)	37709.291	0.017	
P(35)	37701.189	0.013		R(36)	37705.727	-0.085	
P(36)	37697.481	-0.013					
^{63}Cu^{65}Cu: *G66* – X (*v*=0)							
P(45)	37759.988	0.015	P(45)	P(51)	37729.279	0.009	P(51)
P(48)	37746.057	-0.037	P(48)	R(48)	37754.879	-0.018	P(48)
P(48)	37746.121	0.027	P(48)	R(49)	37750.800	0.031	P(49)
P(49)	37742.115	0.009	P(49)				
^{63}Cu^{65}Cu: *G68* – X (*v*=0)							
P(20)	38045.225	0.010	P(20)	P(30)	38021.667	-0.028	P(30)
P(23)	38038.394	-0.041	P(23)	P(31)	38010.357	0.010	P(31)
P(23)	38038.435	0.000	P(23)	P(32)	38008.171	0.053	P(32)
P(24)	38036.032	0.013	P(24)	R(20)	38049.976	0.019	P(20)
P(26)	38031.021	0.001	P(28)	R(25)	38039.779	-0.023	P(25)
P(26)	38031.033	0.013	P(26)	R(26)	38037.739	-0.013	P(26)
P(27)	38028.508	0.016	P(27)	R(27)	38035.843	-0.016	P(27)
P(28)	38026.013	-0.004	P(28)	R(28)	38034.341	0.059	P(30)
P(28)	38026.014	-0.003	P(30)	R(29)	38023.350	-0.010	P(29)
P(29)	38023.666	-0.032	P(14)	R(29)	38023.372	0.012	P(14)
P(29)	38023.674	-0.024	P(29)	R(32)	38016.543	-0.052	P(32)
^{63}Cu^{65}Cu: *I1* – X (*v*=0)							
P(3)	37405.977	-0.011	P(3)	Q(21)	37408.276	-0.099	P(8)
P(3)	37405.990	0.002	P(3)	Q(21)	37408.336	-0.039	P(2)
P(3)	37405.993	0.005	P(3)	Q(21)	37408.342	-0.033	P(21)
P(4)	37405.812	0.013	P(4)	Q(22)	37408.439	-0.095	P(3)
P(5)	37405.594	-0.024	P(10)	Q(22)	37408.464	-0.070	P(3)
P(5)	37405.689	0.071	P(5)	Q(22)	37408.479	-0.055	P(3)

Transition	Observed	Residuals	Probe	Transition	Observed	Residuals	Probe
P(6)	37405.498	0.053	P(6)	Q(22)	37408.541	0.007	P(22)
P(7)	37405.280	-0.001	P(7)	Q(26)	37409.271	0.046	P(28)
P(9)	37405.011	0.036	P(9)	Q(27)	37409.413	0.004	P(29)
P(9)	37405.014	0.039	P(13)	Q(27)	37409.414	0.005	P(27)
P(10)	37404.854	0.020	P(14)	Q(28)	37409.602	0.004	P(30)
P(11)	37404.714	0.014	P(11)	Q(29)	37409.843	0.052	P(31)
P(13)	37404.487	0.031	P(13)	Q(30)	37409.975	-0.013	P(30)
P(14)	37404.354	0.008	P(14)	Q(31)	37410.161	-0.027	P(31)
P(15)	37404.237	-0.005	P(18)	Q(31)	37410.188	0.000	P(31)
P(15)	37404.276	0.034	P(15)	Q(32)	37410.357	-0.034	P(32)
P(16)	37404.151	0.005	P(19)	Q(33)	37410.575	-0.022	P(33)
P(16)	37404.152	0.006	P(16)	Q(34)	37410.799	-0.007	P(34)
P(17)	37404.070	0.013	P(17)	Q(34)	37410.842	0.036	P(34)
P(17)	37404.075	0.018	P(20)	Q(34)	37410.936	0.130	P(34)
P(18)	37403.972	-0.002	P(18)	Q(35)	37411.004	-0.012	P(35)
P(20)	37403.814	-0.015	P(20)	Q(35)	37411.098	0.082	P(35)
P(21)	37403.701	-0.065	P(8)	Q(36)	37411.222	-0.007	P(36)
P(21)	37403.724	-0.042	P(2)	Q(36)	37411.228	-0.001	P(36)
P(21)	37403.730	-0.036	P(21)	Q(36)	37411.271	0.042	P(36)
P(22)	37403.576	-0.134	P(3)	Q(37)	37411.452	0.010	P(37)
P(22)	37403.688	-0.022	P(22)	Q(39)	37411.816	-0.057	P(39)
P(22)	37403.699	-0.011	P(3)	Q(40)	37412.052	-0.037	P(40)
P(22)	37403.701	-0.009	P(3)	R(3)	37407.537	-0.004	P(3)
P(23)	37403.577	-0.082	P(4)	R(5)	37408.075	0.018	P(5)
P(24)	37403.570	-0.044	P(5)	R(6)	37408.365	0.038	P(6)
P(25)	37403.488	-0.086	P(6)	R(7)	37408.654	0.048	P(7)
P(25)	37403.515	-0.059	P(25)	R(9)	37409.221	0.036	P(13)
P(26)	37403.525	-0.014	P(28)	R(9)	37409.265	0.080	P(9)
P(27)	37403.451	-0.059	P(27)	R(10)	37409.516	0.030	P(14)
P(27)	37403.498	-0.012	P(29)	R(13)	37410.449	0.014	P(13)
P(28)	37403.509	0.024	P(30)	R(14)	37410.776	0.011	P(14)

Transition	Observed	Residuals	Probe	Transition	Observed	Residuals	Probe
P(29)	37403.413	-0.052	P(31)	R(15)	37411.093	-0.010	P(15)
P(29)	37403.470	0.005	P(31)	R(15)	37411.099	-0.004	P(18)
P(30)	37403.442	-0.007	P(11)	R(16)	37411.468	0.021	P(16)
P(30)	37403.461	0.012	P(30)	R(16)	37411.471	0.024	P(19)
P(31)	37403.416	-0.021	P(31)	R(17)	37411.760	-0.038	P(17)
P(31)	37403.427	-0.010	P(31)	R(17)	37411.786	-0.012	P(20)
P(32)	37403.376	-0.052	P(32)	R(18)	37412.146	-0.009	P(18)
P(33)	37403.415	-0.008	P(33)	R(20)	37412.866	-0.022	P(20)
P(34)	37403.395	-0.026	P(34)	R(21)	37413.260	-0.004	P(21)
P(34)	37403.408	-0.013	P(34)	R(22)	37413.539	-0.106	P(3)
P(34)	37403.412	-0.009	P(34)	R(22)	37413.582	-0.063	P(3)
P(34)	37403.466	0.045	P(34)	R(22)	37413.616	-0.029	P(3)
P(35)	37403.415	-0.006	P(35)	R(22)	37413.647	0.002	P(22)
P(35)	37403.420	-0.001	P(35)	R(24)	37414.310	-0.113	P(10)
P(36)	37403.429	0.005	P(36)	R(25)	37414.786	-0.034	P(6)
P(36)	37403.462	0.038	P(36)	R(25)	37414.812	-0.008	P(25)
P(37)	37403.449	0.021	P(37)	R(26)	37415.161	-0.060	P(28)
P(38)	37403.490	0.055	P(38)	R(27)	37415.604	-0.022	P(27)
P(39)	37403.445	0.003	P(39)	R(27)	37415.612	-0.014	P(29)
P(39)	37403.504	0.062	P(39)	R(28)	37415.999	-0.037	P(30)
P(40)	37403.496	0.045	P(40)	R(29)	37416.417	-0.033	P(31)
P(40)	37403.536	0.085	P(40)	R(29)	37416.459	0.009	P(31)
P(51)	37403.446	-0.037	P(52)	R(30)	37416.841	-0.026	P(11)
Q(3)	37406.664	0.011	P(3)	R(31)	37417.232	-0.055	P(31)
Q(3)	37406.692	0.039	P(3)	R(31)	37417.286	-0.001	P(31)
Q(3)	37406.708	0.055	P(3)	R(32)	37417.696	-0.014	P(32)
Q(4)	37406.642	-0.043	P(4)	R(34)	37418.567	0.004	P(34)
Q(5)	37406.773	0.048	P(5)	R(34)	37418.592	0.029	P(34)
Q(5)	37406.839	0.114	P(10)	R(35)	37419.015	0.022	P(35)
Q(6)	37406.803	0.030	P(6)	R(35)	37419.059	0.066	P(35)
Q(7)	37406.842	0.013	P(7)	R(35)	37419.059	0.066	P(35)

Transition	Observed	Residuals	Probe	Transition	Observed	Residuals	Probe
Q(9)	37406.940	-0.023	P(13)	R(36)	37419.464	0.040	P(36)
Q(9)	37406.986	0.023	P(9)	R(36)	37419.466	0.042	P(36)
Q(10)	37407.037	-0.005	P(14)	R(36)	37419.470	0.046	P(36)
Q(11)	37407.147	0.018	P(11)	R(37)	37419.879	0.023	P(37)
Q(13)	37407.344	0.021	P(13)	R(38)	37420.367	0.078	P(38)
Q(14)	37407.416	-0.015	P(17)	R(39)	37420.759	0.036	P(39)
Q(14)	37407.447	0.016	P(14)	R(39)	37420.820	0.097	P(39)
Q(15)	37407.546	0.000	P(18)	R(40)	37421.204	0.048	P(40)
Q(15)	37407.560	0.014	P(15)	R(40)	37421.241	0.085	P(40)
Q(16)	37407.632	-0.036	P(19)	R(50)	37425.313	-0.078	P(51)
Q(16)	37407.673	0.005	P(16)	R(51)	37425.681	-0.114	P(52)
Q(20)	37408.233	0.012	P(20)				
^{63}Cu^{65}Cu: *I2* – X (*v*=0)							
P(3)	37693.797	0.015	P(3)	Q(19)	37696.155	-0.006	P(19)
P(5)	37693.447	0.027	P(10)	Q(19)	37696.205	0.044	P(7)
P(5)	37693.463	0.043	P(5)	Q(21)	37696.545	0.002	P(21)
P(5)	37693.477	0.057	P(5)	Q(21)	37696.582	0.039	P(8)
P(7)	37693.100	0.004	P(7)	Q(22)	37696.723	-0.025	P(3)
P(7)	37693.103	0.007	P(7)	Q(22)	37696.772	0.024	P(22)
P(8)	37692.977	0.030	P(8)	Q(23)	37696.956	-0.006	P(23)
P(9)	37692.835	0.027	P(13)	Q(24)	37697.161	-0.025	P(24)
P(10)	37692.678	-0.001	P(10)	Q(24)	37697.168	-0.018	P(5)
P(10)	37692.683	0.004	P(14)	Q(25)	37697.465	0.046	P(25)
P(11)	37692.588	0.030	P(11)	Q(26)	37697.593	-0.069	P(7)
P(12)	37692.468	0.020	P(12)	Q(26)	37697.593	-0.069	P(26)
P(13)	37692.359	0.013	P(13)	Q(26)	37697.623	-0.039	P(7)
P(14)	37692.263	0.009	P(14)	Q(27)	37697.942	0.029	P(27)
P(15)	37692.129	-0.042	P(18)	Q(28)	37698.152	-0.023	P(28)
P(15)	37692.166	-0.005	P(15)	Q(32)	37699.326	0.011	P(32)
P(16)	37692.066	-0.032	P(5)	Q(35)	37700.244	-0.025	P(35)
P(16)	37692.108	0.010	P(19)	Q(40)	37702.092	0.042	P(40)

Transition	Observed	Residuals	Probe	Transition	Observed	Residuals	Probe
P(17)	37692.049	0.016	P(17)	Q(44)	37703.700	0.052	P(44)
P(18)	37692.002	0.023	P(18)	Q(49)	37705.899	0.037	P(50)
P(19)	37691.892	-0.042	P(7)	Q(50)	37706.282	-0.052	P(51)
P(19)	37691.912	-0.022	P(20)	R(3)	37695.336	-0.007	P(3)
P(19)	37691.945	0.011	P(19)	R(3)	37695.337	-0.006	P(3)
P(21)	37691.856	-0.015	P(8)	R(5)	37695.878	0.006	P(5)
P(21)	37691.859	-0.012	P(21)	R(5)	37695.880	0.008	P(5)
P(22)	37691.813	-0.041	P(3)	R(5)	37695.900	0.028	P(10)
P(22)	37691.834	-0.020	P(3)	R(7)	37696.405	-0.034	P(7)
P(22)	37691.900	0.046	P(22)	R(7)	37696.413	-0.026	P(7)
P(23)	37691.873	0.026	P(23)	R(8)	37696.744	0.008	P(8)
P(24)	37691.812	-0.037	P(5)	R(9)	37697.046	0.003	P(13)
P(24)	37691.875	0.026	P(24)	R(10)	37697.356	-0.003	P(14)
P(25)	37691.900	0.040	P(25)	R(10)	37697.372	0.013	P(10)
P(26)	37691.870	-0.011	P(7)	R(11)	37697.700	0.015	P(11)
P(26)	37691.897	0.016	P(7)	R(12)	37698.036	0.017	P(12)
P(26)	37691.903	0.022	P(26)	R(13)	37698.348	-0.015	P(13)
P(27)	37691.917	0.006	P(8)	R(14)	37698.698	-0.019	P(14)
P(28)	37691.965	0.014	P(28)	R(15)	37699.049	-0.030	P(18)
P(29)	37691.959	-0.041	P(10)	R(15)	37699.083	0.004	P(15)
P(32)	37692.227	0.022	P(32)	R(16)	37699.386	-0.065	P(5)
P(35)	37692.528	0.032	P(35)	R(16)	37699.456	0.005	P(19)
P(44)	37693.930	0.040	P(44)	R(17)	37699.833	0.000	P(17)
P(49)	37694.977	-0.027	P(50)	R(18)	37700.211	-0.012	P(18)
Q(3)	37694.445	-0.006	P(3)	R(19)	37700.628	0.004	P(19)
Q(5)	37694.542	0.008	P(5)	R(21)	37701.429	-0.023	P(21)
Q(5)	37694.543	0.009	P(5)	R(21)	37701.465	0.013	P(8)
Q(5)	37694.549	0.015	P(10)	R(22)	37701.880	0.000	P(22)
Q(7)	37694.630	-0.025	P(7)	R(22)	37701.881	0.001	P(3)
Q(7)	37694.667	0.012	P(7)	R(22)	37701.882	0.002	P(3)
Q(8)	37694.696	-0.033	P(8)	R(23)	37702.316	-0.002	P(23)

Transition	Observed	Residuals	Probe	Transition	Observed	Residuals	Probe
Q(9)	37694.817	0.004	P(13)	R(24)	37702.781	0.017	P(24)
Q(10)	37694.859	-0.047	P(14)	R(25)	37703.215	-0.006	P(25)
Q(10)	37694.928	0.022	P(10)	R(26)	37703.646	-0.041	P(7)
Q(11)	37694.988	-0.020	P(11)	R(26)	37703.689	0.002	P(7)
Q(12)	37695.114	-0.006	P(12)	R(26)	37703.736	0.049	P(26)
Q(13)	37695.214	-0.026	P(13)	R(28)	37704.613	-0.033	P(28)
Q(14)	37695.366	-0.005	P(14)	R(32)	37706.705	0.026	P(32)
Q(15)	37695.465	-0.045	P(18)	R(35)	37708.282	-0.021	P(35)
Q(15)	37695.545	0.035	P(15)	R(40)	37711.232	0.032	P(40)
Q(16)	37695.671	0.012	P(19)	R(44)	37713.699	0.010	P(44)
Q(17)	37695.797	-0.020	P(17)	R(49)	37716.978	-0.039	P(50)
Q(18)	37695.962	-0.022	P(18)	R(50)	37717.709	-0.003	P(51)
$^{63}Cu^{65}Cu$: (0,0) J – X							
P(9)	37447.053	-0.043	P(9)	R(15)	37453.124	0.006	P(15)
P(11)	37446.947	0.035	P(11)	R(16)	37454.974	-0.005	P(16)
P(13)	37446.773	0.009	P(13)	R(17)	37455.159	0.008	P(17)
P(15)	37446.573	-0.033	P(15)	R(18)	37455.503	-0.009	P(18)
P(16)	37446.462	0.005	P(16)	R(20)	37456.399	-0.011	P(20)
P(20)	37447.207	0.021	P(20)	R(21)	37456.842	-0.060	P(21)
P(21)	37447.185	-0.006	P(21)	R(21)	37456.857	-0.045	P(2)
P(22)	37447.212	-0.020	P(3)	R(22)	37457.370	-0.043	P(3)
P(22)	37447.223	-0.009	P(22)	R(22)	37457.389	-0.024	P(22)
P(25)	37447.389	-0.093	P(25)	R(25)	37459.099	0.065	P(25)
P(30)	37448.189	0.034	P(32)	R(26)	37459.583	-0.014	P(7)
P(30)	37448.205	0.050	P(30)	R(27)	37460.176	0.008	P(27)
P(31)	37448.266	-0.036	P(31)	R(29)	37461.369	0.054	P(31)
P(32)	37448.431	-0.005	P(32)	R(30)	37461.886	0.012	P(32)
P(32)	37448.436	0.000	P(32)	R(30)	37461.900	0.026	P(30)
P(33)	37448.602	0.067	P(33)	R(31)	37462.397	-0.002	P(31)
P(34)	37448.595	0.032	P(34)	R(32)	37462.839	-0.013	P(32)
P(35)	37450.759	-0.012	P(35)	R(32)	37462.887	0.035	P(34)

Transition	Observed	Residuals	Probe	Transition	Observed	Residuals	Probe
P(35)	37450.816	0.045	P(35)	R(32)	37462.892	0.040	P(32)
P(36)	37450.637	-0.054	P(36)	R(33)	37465.475	-0.011	P(33)
P(36)	37450.668	-0.023	P(36)	R(34)	37465.880	0.050	P(34)
P(36)	37450.737	0.046	P(36)	R(35)	37466.275	-0.046	P(35)
P(37)	37450.778	0.022	P(37)	R(35)	37466.291	-0.030	P(35)
P(38)	37450.887	-0.034	P(38)	R(35)	37466.389	0.068	P(35)
P(38)	37450.981	0.060	P(38)	R(36)	37466.872	-0.038	P(36)
P(39)	37451.127	-0.023	P(39)	R(36)	37466.887	-0.023	P(36)
P(39)	37451.243	0.094	P(39)	R(36)	37466.887	-0.023	P(36)
P(40)	37451.430	0.010	P(40)	R(37)	37467.574	0.011	P(37)
P(41)	37451.731	0.011	P(41)	R(37)	37467.597	0.034	P(37)
P(42)	37452.018	-0.024	P(42)	R(38)	37468.230	-0.028	P(38)
P(43)	37452.334	-0.045	P(43)	R(38)	37468.262	0.004	P(38)
P(44)	37452.680	-0.041	P(44)	R(39)	37468.992	0.009	P(39)
P(44)	37452.680	-0.041	P(44)	R(39)	37469.023	0.040	P(39)
P(45)	37453.010	-0.018	P(45)	R(40)	37469.773	0.044	P(40)
P(45)	37453.013	-0.015	P(45)	R(41)	37470.474	-0.017	P(41)
P(46)	37452.868	0.008	P(46)	R(42)	37471.295	0.039	P(42)
P(46)	37452.870	0.010	P(46)	R(43)	37471.965	-0.022	P(43)
R(3)	37449.538	0.009	P(3)	R(43)	37471.982	-0.005	P(43)
R(3)	37449.567	0.038	P(3)	R(44)	37472.232	-0.012	P(44)
R(5)	37450.095	-0.007	P(5)	R(44)	37472.245	0.001	P(44)
R(5)	37450.152	0.050	P(10)	R(45)	37474.057	-0.031	P(45)
R(6)	37450.451	0.043	P(6)	R(45)	37474.080	-0.008	P(45)
R(7)	37450.754	0.028	P(7)	R(46)	37474.814	-0.015	P(46)
R(9)	37451.361	-0.036	P(9)	R(46)	37474.836	0.007	P(46)
R(11)	37452.111	0.008	P(11)	R(47)	37475.714	0.046	P(47)
R(13)	37452.797	-0.002	P(13)	R(50)	37478.367	0.012	P(51)
R(14)	37453.085	0.009	P(14)				
$^{63}Cu^{65}Cu$: (1,0) J – X							
P(3)	37733.530	0.014	P(3)	R(10)	37737.247	0.038	P(10)

Transition	Observed	Residuals	Probe	Transition	Observed	Residuals	Probe
P(5)	37733.235	0.067	P(5)	R(11)	37737.547	-0.007	P(11)
P(7)	37732.834	-0.031	P(7)	R(12)	37737.915	0.008	P(12)
P(8)	37732.708	-0.022	P(8)	R(13)	37738.308	0.039	P(13)
P(9)	37732.587	-0.019	P(13)	R(14)	37738.644	0.006	P(14)
P(10)	37732.544	0.051	P(10)	R(15)	37738.995	-0.018	P(15)
P(11)	37732.366	-0.024	P(11)	R(16)	37739.396	0.006	P(19)
P(12)	37732.270	-0.028	P(12)	R(17)	37739.817	0.050	P(17)
P(13)	37732.237	0.022	P(13)	R(18)	37740.093	-0.042	P(18)
P(14)	37732.118	-0.024	P(14)	R(19)	37740.468	-0.016	P(19)
P(15)	37732.047	-0.030	P(15)	R(20)	37740.771	-0.017	P(20)
P(16)	37732.020	0.001	P(19)	R(21)	37741.016	0.019	P(21)
P(17)	37732.022	0.055	P(17)	R(22)	37740.984	-0.011	P(22)
P(18)	37731.915	-0.003	P(18)	R(23)	37740.530	-0.015	P(23)
P(19)	37731.861	-0.007	P(19)	R(24)	37745.368	-0.014	P(24)
P(20)	37731.846	0.036	P(20)	R(25)	37745.298	0.009	P(25)
P(21)	37731.810	0.079	P(21)	R(26)	37745.512	0.016	P(26)
P(22)	37731.625	0.016	P(22)	R(27)	37745.813	-0.041	P(29)
P(23)	37731.395	0.003	P(23)	R(27)	37745.858	0.004	P(27)
P(24)	37730.962	-0.001	P(24)	R(28)	37746.329	0.035	P(28)
P(25)	37730.088	0.000	P(25)	R(29)	37746.819	0.033	P(29)
P(26)	37734.535	0.036	P(26)	R(30)	37747.383	0.069	P(30)
P(27)	37733.931	-0.049	P(27)	R(31)	37747.917	0.048	P(31)
P(28)	37733.794	0.033	P(28)	R(36)	37750.970	0.040	P(36)
P(30)	37733.676	-0.031	P(32)	R(37)	37751.579	-0.009	P(37)
P(30)	37733.723	0.016	P(30)	R(38)	37752.238	-0.019	P(38)
P(33)	37734.041	0.035	P(33)	R(39)	37752.939	0.001	P(39)
P(36)	37734.528	0.010	P(36)	R(40)	37753.615	-0.013	P(40)
P(37)	37734.719	-0.003	P(37)	R(41)	37754.294	-0.032	P(41)
P(38)	37734.939	-0.002	P(38)	R(41)	37754.308	-0.018	P(41)
P(39)	37735.201	0.027	P(39)	R(42)	37754.998	-0.030	P(42)
P(40)	37735.459	0.041	P(40)	R(43)	37755.826	0.099	P(43)

Transition	Observed	Residuals	Probe	Transition	Observed	Residuals	Probe
P(41)	37735.615	-0.060	P(41)	R(45)	37757.116	0.073	P(45)
P(42)	37735.897	-0.044	P(42)	R(46)	37757.475	-0.037	P(46)
P(43)	37736.234	0.019	P(43)	R(47)	37757.254	-0.042	P(47)
P(44)	37736.462	-0.031	P(44)	R(48)	37761.225	-0.069	P(48)
P(46)	37737.002	-0.026	P(46)	R(48)	37761.299	0.005	P(48)
P(49)	37736.642	-0.001	P(49)	R(49)	37761.479	0.007	P(49)
P(51)	37739.903	-0.070	P(51)	R(50)	37762.084	0.004	P(50)
R(3)	37735.160	0.070	P(3)	R(50)	37762.151	0.071	P(51)
R(7)	37736.186	-0.051	P(7)	R(51)	37762.836	0.016	P(52)
R(8)	37736.560	0.009	P(8)	R(51)	37762.874	0.054	P(51)
R(9)	37736.829	-0.046	P(13)				
$^{63}Cu^{65}Cu$: (2,0) J – X							
P(4)	38017.020	0.017	P(4)	R(9)	38020.399	0.014	P(9)
P(4)	38017.043	0.040	P(4)	R(10)	38020.690	0.008	P(10)
P(5)	38016.811	-0.011	P(5)	R(10)	38020.698	0.016	P(14)
P(6)	38016.672	0.023	P(6)	R(11)	38020.964	-0.019	P(11)
P(7)	38016.470	-0.014	P(7)	R(11)	38020.990	0.007	P(11)
P(7)	38016.520	0.036	P(7)	R(11)	38020.991	0.008	P(11)
P(8)	38016.319	-0.008	P(8)	R(12)	38021.276	-0.005	P(12)
P(9)	38016.157	-0.020	P(9)	R(13)	38021.563	0.006	P(13)
P(9)	38016.191	0.014	P(9)	R(14)	38022.172	0.022	P(14)
P(10)	38016.043	0.008	P(10)	R(15)	38022.404	-0.011	P(15)
P(11)	38015.863	-0.037	P(11)	R(15)	38022.421	0.006	P(15)
P(11)	38015.899	-0.001	P(11)	R(15)	38022.471	0.056	P(18)
P(11)	38015.905	0.005	P(11)	R(16)	38022.711	-0.019	P(16)
P(12)	38015.760	-0.011	P(12)	R(16)	38022.723	-0.007	P(16)
P(13)	38015.644	-0.001	P(13)	R(17)	38023.029	-0.034	P(20)
P(14)	38015.517	0.001	P(14)	R(17)	38023.043	-0.020	P(17)
P(14)	38015.541	0.025	P(16)	R(17)	38023.058	-0.005	P(17)
P(15)	38015.342	-0.022	P(15)	R(18)	38023.420	0.016	P(18)
P(15)	38015.370	0.006	P(15)	R(19)	38023.747	0.000	P(19)

Transition	Observed	Residuals	Probe	Transition	Observed	Residuals	Probe
P(16)	38015.517	-0.014	P(16)	R(20)	38024.079	-0.008	P(20)
P(16)	38015.525	-0.006	P(16)	R(20)	38024.100	0.013	P(20)
P(17)	38015.363	-0.006	P(17)	R(21)	38024.324	-0.096	P(21)
P(18)	38015.267	0.010	P(18)	R(21)	38024.418	-0.002	P(21)
P(19)	38015.177	0.013	P(19)	R(22)	38024.719	-0.017	P(22)
P(20)	38015.042	-0.036	P(20)	R(22)	38024.794	0.058	P(22)
P(21)	38014.978	-0.017	P(21)	R(23)	38025.003	-0.021	P(23)
P(22)	38014.885	-0.024	P(22)	R(23)	38025.008	-0.016	P(23)
P(23)	38014.790	-0.025	P(23)	R(23)	38025.012	-0.012	P(23)
P(24)	38014.678	-0.027	P(5)	R(24)	38025.227	-0.036	P(24)
P(24)	38014.695	-0.010	P(24)	R(24)	38025.239	-0.024	P(24)
P(25)	38014.556	-0.010	P(25)	R(24)	38025.258	-0.005	P(24)
P(26)	38014.357	-0.023	P(26)	R(25)	38025.447	0.027	P(25)
P(27)	38014.154	0.043	P(27)	R(25)	38025.484	0.064	P(25)
P(28)	38013.718	0.019	P(28)	R(26)	38025.419	-0.016	P(26)
P(29)	38013.010	-0.032	P(29)	R(26)	38025.456	0.021	P(28)
P(30)	38011.984	0.006	P(30)	R(26)	38025.456	0.021	P(26)
P(31)	38020.155	-0.014	P(31)	R(26)	38025.473	0.038	P(28)
P(32)	38019.191	0.036	P(32)	R(27)	38025.203	0.000	P(29)
P(33)	38018.583	0.040	P(33)	R(27)	38025.226	0.023	P(27)
P(34)	38018.233	0.040	P(34)	R(28)	38024.558	-0.007	P(28)
P(35)	38018.032	0.027	P(35)	R(28)	38024.595	0.030	P(30)
P(36)	38017.853	-0.068	P(20)	R(29)	38033.160	-0.022	P(14)
P(36)	38017.902	-0.019	P(36)	R(29)	38033.170	-0.012	P(29)
P(38)	38017.872	-0.068	P(38)	R(30)	38032.640	0.046	P(30)
R(4)	38019.023	0.025	P(4)	R(31)	38032.428	0.021	P(31)
R(4)	38019.065	0.067	P(4)	R(32)	38032.517	0.035	P(32)
R(5)	38019.275	0.015	P(5)	R(33)	38032.786	0.066	P(33)
R(6)	38019.471	-0.059	P(6)	R(34)	38033.063	0.003	P(34)
R(7)	38019.791	-0.017	P(7)	R(35)	38033.465	-0.005	P(35)
R(8)	38020.124	0.031	P(8)	R(36)	38033.925	-0.004	P(36)

Transition	Observed	Residuals	Probe	Transition	Observed	Residuals	Probe
R(9)	38020.380	-0.005	P(9)	R(38)	38034.936	-0.015	P(38)
^{63}Cu^{65}Cu: *L1* – X (*v*=0)							
P(29)	37453.361	0.031	P(31)	R(32)	37465.289	-0.015	P(32)
P(30)	37452.847	0.026	P(32)	R(33)	37463.229	0.047	P(33)
P(32)	37451.808	-0.025	P(32)	R(34)	37463.309	-0.043	P(34)
P(33)	37451.382	-0.005	P(33)	R(35)	37463.352	-0.028	P(35)
P(34)	37450.987	-0.028	P(34)	R(35)	37463.367	-0.013	P(35)
P(35)	37448.414	-0.054	P(35)	R(35)	37463.372	-0.008	P(35)
P(35)	37448.468	0.000	P(35)	R(36)	37463.285	-0.026	P(36)
P(36)	37448.167	-0.045	P(36)	R(36)	37463.287	-0.024	P(36)
P(36)	37448.173	-0.039	P(36)	R(36)	37463.316	0.005	P(36)
P(36)	37448.197	-0.015	P(36)	R(37)	37463.199	0.016	P(37)
P(37)	37447.793	-0.022	P(37)	R(37)	37463.208	0.025	P(37)
P(38)	37447.339	0.017	P(38)	R(38)	37463.020	0.005	P(38)
P(39)	37446.812	0.043	P(39)	R(38)	37463.054	0.039	P(38)
R(29)	37465.317	-0.014	P(31)				
^{63}Cu^{65}Cu: *O1* – X (*v*=0)							
P(14)	38016.167	0.025	P(14)	R(19)	38021.794	0.012	P(19)
P(15)	38015.785	-0.013	P(15)	R(20)	38021.758	0.029	P(20)
P(15)	38015.787	-0.011	P(15)	R(21)	38021.704	0.042	P(21)
P(27)	38009.947	-0.008	P(27)	R(22)	38021.511	-0.071	P(23)
R(14)	38021.713	-0.037	P(14)	R(22)	38021.582	0.000	P(22)
R(15)	38021.821	-0.008	P(15)	R(23)	38021.511	0.022	P(23)
R(15)	38021.824	-0.005	P(15)	R(24)	38021.365	-0.018	P(24)
R(15)	38021.848	0.019	P(18)	R(25)	38021.279	0.014	P(25)
R(17)	38021.845	-0.001	P(17)	R(26)	38021.103	-0.031	P(26)
R(17)	38021.851	0.005	P(20)	R(28)	38020.821	-0.013	P(28)
R(18)	38021.820	-0.002	P(18)	R(29)	38020.698	0.034	P(14)